PPLN-based photon pair sources toward biphoton quantum frequency conversion

by

Aimee K. Gunther

A thesis
presented to the University of Waterloo
in fulfillment of the
thesis requirement for the degree of
Doctor of Philosophy
in
Physics (Quantum Information)

Waterloo, Ontario, Canada, 2018

Examining Committee Membership

The following served on the Examining Committee for this thesis. The decision of the Examining Committee is by majority vote.

External Examiner	Konrad Banaszek Professor
Supervisor	Thomas Jennewein Associate Professor
Internal Member	Kevin Resch Professor
Internal-external Member	Michal Bajcsy Assistant Professor
Other Member	Kostadinka Bizheva Associate Professor

This thesis consists of material all of which I authored or co-authored: see Statement of Contributions included in the thesis. This is a true copy of the thesis, including any required final revisions, as accepted by my examiners.

I understand that my thesis may be made electronically available to the public.

Statement of Contributions

Chapter 2

- Piotr Kolenderski, concept and *Mathematica* modelling support
- Aimee Gunther, experiment design, manuscript, analysis, simulation
- Thomas Jennewein, useful discussion

Chapter 3

- Thomas Jennewein, concept
- Aimee Gunther, experiment design, analysis, simulation
- Katanya Kuntz, Jeongwan Jin, Audrey Dot, useful discussion

Chapter 4

- Piotr Kolenderski, concept
- Piotr Kolenderski & Karolina Sedziak, experimental and analysis design
- Karolina Sedziak, SPDC experiment and data analysis
- Piotr Kolenderski & Aimee Gunther - fiber characterization
- Aimee Gunther, SPDC phasematching simulation
- Thomas Jennewien, useful discussions

Chapter 5

- Thomas Jennewein, concept, experiment design
- Aimee Gunther, experiment design, data collection, analysis, simulation
- Jeongwan Jin & Katanya Kuntz, useful discussion
- Jeongwan Jin, coincidence timetagging LabVIEW code and equipment
- Sascha Agne, coincidence timetagging MATLAB code and LabVIEW spaghetti detangling strategies

Abstract

While quantum properties of light promise much-needed enhancements to metrology, further development of quantum light sources and associated tools are needed to readily harness two-photon interactions via energy-time correlations. This thesis will discuss the experimental development of energy-time correlated photon pairs generated within the nonlinear material of bulk periodically-poled lithium niobate toward photon pair up-conversion. Joint spatial-spectral characterizations of this spontaneous parametric down-conversion source are modelled and measured using a unique single-shot spatial-spectral method. In addition, another telecommunication-wavelength entangled photon pair source is simulated and experimentally characterized through dispersive time-of-flight measurements.

As required by the goal of biphoton frequency conversion, a prism compressor for enacting biphoton dispersion cancellation was built and later characterized using wavelength-scanning interferometry. With the amalgamation of these components and techniques, an experimental study of biphoton frequency conversion is constructed and characterized to elucidate this femtosecond-timescale quantum frequency conversion process.

Acknowledgements

Surviving the crucible of graduate school is not possible without a village-worth of support.

First, I would like to thank God, my husband Thomas, and family and friends from communities far and wide for support during my quest to achieve the impossible.

Graduate school would be far less bearable without past and present members of the Fun Office: Christopher Pugh, Ramy Tannous, and Sebastian Slaman. Also, my quantum optics cohort: John Donohue, Mike Mazurek, Kent Bonsma-Fisher, and Jean-Philippe Maclean made learning about creation and annihilation operators and laser alignment much more fun.

To my supervisor Thomas Jennewein, who allowed me to pursue such interesting research. Your commitment to regularly meeting with me throughout this thesis writing process did not go unnoticed.

I received some great advice from my committee: Kevin Resch, Kostadinka Bizheva, and Michal Bajcsy. Thank you also to my external examiner, Konrad Banaszek, for agreeing to read this work.

Additionally, I would like Kevin Resch and his research group for adopting me over this last year. May your early morning journal club presentations never lack vivacious discussion.

My longtime collaborator, Piotr Kolenderski who helped me become the *Mathematica* wizard I am today.

I would like thank my research group, past and present, for allowing me to borrow all those optical parts – with a special shout out to those who edited this thesis.

To the postdocs who have contributed to my doctoral training and shaped me as a scientist, I thank Audrey Dot, Jeongwan Jin, and Katanya Kuntz.

I would like to thank the inspirational university staff who taught me a thing or two about strategic leadership, communication, and administration which enabled me to achieve so much during my education here. Thank you to Angela Olano, Jodi Szimanski, Tobi Day-Hamilton, Kathryn Fedy, Chris Dietrich, Electra Eleftheriadou, Erica Boland, and Maren Butcher.

During this thesis writing process, I would like to thank Olivia di Matteo for thesis editing and Stefanie Beale for company in writing. Additionally I would like to thank the wonderful ladies of my Slack PhD thesis writing group who made the writing process less lonely. After months and months in a dark lab, I profusely thank the Kitchener Public Library, Smile Tiger Coffee Roasters, Settlement Co, Show and Tell Coffee for bright windows and beautiful caffeinated beverages.

Dedication

I dedicate this work to all women, minorities, and people of colour pursuing the academic dream.

Table of Contents

List of Tables xi

List of Figures xii

1 Introduction 1

1.1 Motivation . . . 1

1.2 Mathematical Description of Electric Fields . . . 2

1.3 Nonlinear Optical Frequency Conversion . . . 3

1.3.1 Three-wave mixing . . . 3

1.3.2 Quantum nonlinear optics - spontaneous parametric down-conversion . . . 8

1.3.3 Biphoton frequency conversion . . . 9

1.4 Chromatic Dispersion . . . 10

1.4.1 On slowing things down... – Group delay . . . 11

1.4.2 ...And stretching things out – Group velocity dispersion . . . 13

1.4.3 Tools for manipulating dispersion . . . 13

1.5 Measuring Dispersion Through Interferometry . . . 16

1.5.1 There and back again: optical phase and interference . . . 17

2 Source of Energy-Time Correlated Photon Pairs 20

2.1 Energy-Time Entangled Photon Pair Source . . . 20

2.2 Type-0 SPDC in Bulk PPLN . . . 21

2.2.1 Theoretical models . . . 22

2.2.2 Spectral and spatial source characterization . . . 23

2.3 X-Spectrum: Spatial-Spectral Properties . . . 27
2.3.1 "X-blobs": A single-shot measurement method for spatial-spectral characterization . . . 27
2.3.2 Discussion . . . 29

3 White Light Interferometry for Dispersion Characterization 30
3.1 Inspiration: Spectral Interferometry By Way of Optical Coherence Tomography . . . 30
3.2 Dispersion Characterization Experiment . . . 31
3.2.1 Swept-source laser . . . 31
3.2.2 Swept-source white light interferometer . . . 31
3.2.3 Data processing: Sweep manipulation . . . 32
3.3 Spectral Phase Extraction . . . 33
3.3.1 Fringe counting . . . 34
3.3.2 Hilbert method . . . 34
3.4 Interferometric Characterization of a Prism Compressor . . . 35
3.4.1 Measurement test design: data sets . . . 36
3.4.2 Prism compressor characterization results . . . 38
3.4.3 Discussion . . . 38

4 Dispersed Time-of-Flight Characterization of a Telecom Photon Pair Source 40
4.1 Characterizing a Telecom Photon Pair Source . . . 41
4.2 Dispersion Characterizations of Optical Fibers . . . 41
4.2.1 OPO measurements . . . 42
4.2.2 Calibrating experimental time delays . . . 43
4.3 Photon Source Characterization Results . . . 44
4.3.1 Modelling a telecom SPDC source in PPLN . . . 45
4.3.2 Discussion . . . 45

5 Biphoton Up-Conversion 47
5.1 Biphoton Up-Conversion: A Test of Ultrafast Coincidence Detection . . . 48
5.1.1 Experimental requirements . . . 50

5.1.2 Experimental success metrics . . . 51
5.2 Selected "Ultrafast Coincidence Detector" Properties . . . 52
5.2.1 Phasematching acceptance bandwidth simulations . . . 52
5.2.2 Time-resolved phasematching: up-conversion crystal temperature characterizations . . . 54
5.2.3 Photon hunting in biphoton "pulse" stretch and space: experimental strategies . . . 56
5.3 Discussion . . . 58
5.3.1 Outlook and recommendations . . . 59

6 Conclusion **61**

References **62**

Appendix A Phase Extraction **76**
A.1 Hilbert Transform . . . 76
A.2 Phase Extraction From Sample Wavepacket . . . 77
A.3 Phase Extraction Dependence on Interferometer Displacements . . . 77
A.4 Uncertainty in Interferometer Measurements . . . 78

Appendix B Code **79**
B.1 White Light Interferometry Data Analysis . . . 79
B.2 Cones: Spatial/Spectral Integration Functions . . . 80
B.2.1 SPDC Integration functions . . . 80
B.2.2 A method for choosing parameters for simulating SPDC . . . 83
B.2.3 Spatial donut Gaussian model . . . 83
B.2.4 Gaussian beam propagation . . . 84

List of Tables

1.1 Prism compressor parameters as defined in Fig. 1.3a. 15

2.1 Simulation parameters for modelling PPLN photon pair source. 25

4.1 Simulation parameters for modelling telecom PPLN photon pair source from fiber spectrometer measurements. 45

5.1 Selective literature for biphoton up-conversion. 48

5.2 Experiment focal lengths for up-conversion of down-conversion. 48

5.3 Estimated group delay dispersion calculated at 1064 nm from optics within biphoton portion of the experimental setup displayed in Fig. 5.1. 51

5.4 Up-conversion acceptance bandwidths, calculated via different methods 54

5.5 Measured quantities from Santec HSL-1000 swept-source laser and time-resolved SHG 55

A.1 Fitting coefficients across all mirror displacements of {Air, -setup} (linearized (hilbert-extracted) phase, p.189, lin avg). Adjusted R-squared goodness of fit > 0.999 77

A.2 Extracted GDD results for all dispersion scenarios 78

A.3 Variable definitions from Eq. (A.2). Prism variables are derived from Section 1.4.3 and the linearization, Δlin, is from extracting variance in GDD from theoretical fringes with perfect displacement. 78

B.1 Parameters needed for SPDC simulation. 83

B.2 ABCD law matrices for modelling optical systems 85

List of Figures

1.1 Three-wave mixing energy/frequency combinations and definitions for frequency conversion in this work. . . . 5

1.2 Refraction in a prism . . . 11

1.3 Prism compressor experimental design and variable definitions. Due to folding with retroreflector, $L = 2q+\delta_{\mathrm{RR}}$ with δ_{RR} being the constant internal retroreflector path length. . . . 15

1.4 Theoretical GDD dependencies on prism compressor parameters for the prism compressor shown in Fig. 1.3b. . . . 16

1.5 Two common interferometer configurations where BS is 50:50 beamsplitter; D is a detector; and d is a mirror translation. . . . 17

2.1 PPLN characterization setups for spatial and spectral down-conversion properties. 24

2.2 Temperature-dependent frequency phasematching . . . 25

2.3 Measured SPDC spatial profiles as seen on the beam profiler camera. Noncollinear emission within the 10 nm bandpass filter is only present for temperatures beneath the degenerate collinear temperature of T=132.4°C. . . . 26

2.4 Spatial data . . . 26

2.5 Simulated X-spectra of Type-0 SPDC in PPLN for temperatures below and above degenerate temperature. . . . 27

2.6 Density plots=theory, contours=experiment for lens f=175 mm . . . 28

3.1 Empty, reference Michelson WLI interferometer . . . 32

3.2 Linearized frequency sweep over time . . . 33

3.3 Fringe counting method demonstrated by an interferometer with 24 cm of NFK51A glass over the relevant spectral bandwidth. . . . 35

3.4 White light interferometer built around prism compressor of test . . . 36

3.5 Prism compressor characterization data sets and notation 36
3.6 Example interference fringes from "+glass" prism compressor dispersion 37
3.7 Measured prism compressor GDD 38
3.8 Prism compressor GDD measurements results with glass sample 39

4.1 Setup used in the experiment. HWP: half-wave plate, T: temperature controller, L: lens (L1- F=125.0 mm, L2- F=75.0 mm), BB: beam blocker, DM: dichroic mirror, LP: longpass filter, PBS: polarization beam splitter, M: mirror, FC: fiber couple (F=8.0 mm, A240TM-C), SMF: single-mode fiber, SNSPD: superconducting nanowire single-photon detector. 41
4.2 OPO relative time delay over a 80 m fiber 42
4.3 Optical element configurations inserted into the dotted boxes of Fig 4.1 to determine zero delay for a given single-photon wavelength. BP: bandpass filter, SMF: single-mode fiber, F: longpass filter. 43
4.4 Simulated PPLN tuning curves (density plot) with fiber spectrometer central wavelength results (points). 45

5.1 Experimental setup for up-conversion of down-conversion 49
5.2 Simulated phasematching tolerances for wavelength and crystal temperature using "Method 1" for a 5 mm sample of bulk 5% MgO:PPLN for frequency conversion 1064 nm + 1064 nm → 532 nm. 53
5.3 Time-resolved SHG with crystal temperature 56
5.4 Wavelength-dependent focal shift in optimal single-photon detector position 57
5.5 Demonstration of 3-dimensional scanning capability: dark counts through depth of focus 58

A.1 Example wavepacket phase extraction 77

Chapter 1

Introduction

1.1 Motivation

Quantum properties of light promise much-needed enhancements to metrology, communication, sensing, and imaging [1]. Such enhancements could provide sensing and imaging at resolutions beyond what is capable with the most advanced classical techniques [1].

Single photons, or unit excitations of the electromagnetic field in a specified mode, can be generated from the process of spontaneous parametric down-conversion (SPDC) [2]. These photon pairs, generated within a nonlinear crystal by the parametric splitting of one pump laser photon into two, have been the backbone of many fundamental single-photon experiments [3]. This frequency conversion process, dictated by momentum and energy conservation, allows for these resulting strong intra-pair photon correlations to be utilized for many foundational and applied applications [2].

These properties have been utilized for spectroscopy by the unique large frequency anti-correlation of SPDC [4–6]. However, using one of these photons, or even a pair of photons each sent to separate subsystems, doesn't inherently provide much spectroscopic benefit [1]. My goal instead is to use such pairs of photons for investigating two-photon interactions, such as two-photon absorption, probing two-photon transitions, or the like to allow for the harnessing of the unique high temporal and frequency resolution dictated by this parametric process. It has been shown such frequency anti-correlated photon pairs require a lower flux of incident light than analogous classical excitations [7]. This opens the door for potential advantageous applications such as sensitive two-photon microscopy.

Already, a wide array of two-photon experiments have demonstrated such properties in SPDC in utilizing femtosecond-timescale temporal control over photon pair up-conversion [8–10]. These two-photon properties have be applied to applications such as: higher-dimensional quantum information [11]; imaging [12]; and demonstrations of dispersion cancellation [13, 14]. Additionally,

entangled two-photon absorption has been demonstrated with SPDC in rubidium vapor by Dayan et al. [15].

This motivation here could have a direct application in practical entangled two-photon absorption for microscopy, imaging, and spectroscopy. The nonlinear process, two-photon absorption, plays a pivotal role in field of fluorescence microscopy [16, 17]. Pulses from ultrafast lasers provide two-photon imaging benefits of increased imaging depth and reduced out-of-focus noise fluorescence over standard microscopy utilizing one-photon absorption. In order to wield the rich, manipulatable properties of SPDC to apply and probe other complex physical systems, photon pair sources and ultrashort pulse shaping coherent control is required. In this work, I seek to elucidate the experimental requirements for achieving biphoton, or photon pair up-conversion in second-order nonlinear media.

The following sections provide the mathematical background toward the underlying principals of the key experimental pieces required for biphoton frequency conversion. Nonlinear frequency conversion, both for photon pair generation and summation, is discussed as well the necessary ultrafast optical tools and concepts. Additionally, background methodology behind relevant characterization techniques is also shown.

1.2 Mathematical Description of Electric Fields

A pulse of light can be described by electromagnetic waves which can be mathematically described as a spatially and temporally-dependent electric field [18, 19]. With such an electromagnetic description, the basis for later interactions with dielectric material can later be described toward our end goal of biphoton frequency conversion and manipulation.

The following electric field definitions, following closely with [18], by no means describe all optical degrees of freedom, but provide a basis for which the frequency (and related energy) and time degrees of freedom can be described and manipulated.

Beginning with a temporal description, independent of the spatial and polarization degrees of freedom, let us first define a function representing the electric field as $E(t)$, which exists initially as a real-valued function. It is mathematically convenient for the frequency-domain description to be defined as the Fourier transform

$$\tilde{E}(\omega) = \int_{-\infty}^{\infty} E(t) e^{-i\omega t} dt \tag{1.1}$$

$$\tilde{E}(t) = \int_{-\infty}^{\infty} E(\omega) e^{i\omega t} d\omega. \tag{1.2}$$

In addition it is practical to consider only positive frequencies:

$$\tilde{E}^{+}(t) = \frac{1}{2\pi} \int_{0}^{\infty} \tilde{E}(\omega) e^{i\omega t} d\omega \tag{1.3}$$

for

$$\tilde{E}^+(\omega) = |\tilde{E}(\omega)|e^{i\phi(\omega)} = \begin{cases} \tilde{E}(\omega) & \text{for} \quad \omega \geq 0 \\ 0 & \text{for} \quad \omega < 0 \end{cases} \tag{1.4}$$

where $\phi(\omega)$ is the spectral phase, conceptually and literally expanded upon later. These physical, positive frequency electric field definitions can be related back to the initial definitions by

$$E(t) = \tilde{E}^+(t) + \tilde{E}^-(t) \tag{1.5}$$

$$\tilde{E}(\omega) = \tilde{E}^+(\omega) + \tilde{E}^-(\omega) \tag{1.6}$$

What will be a useful concept later, additionally $E(t)$ can be related to $\tilde{E}^+(t)$ by

$$\tilde{E}^+(t) = E(t) + iH\{E(t)\} \tag{1.7}$$

where $E'(t)$ is the Hilbert transform of $E(t)$. That is, $\tilde{E}^+(t)$ is a complex analytic signal derived from a real-valued $E(t)$ and generated imaginary component, $\mathrm{H}\{E(t)\}$. The Hilbert function is further discussed in Section A.1.

Furthermore, the electric field can also be described as a real amplitude and phase

$$\tilde{E}^+(t) = \frac{1}{2}\mathcal{E}(t)e^{i[\phi_0+\phi(t)+\omega_l t]} \tag{1.8}$$

where the phase in this representation can be decomposed into: a carrier to the envelope phase, ϕ_0, which can be neglected for the length of pulses here; a time-dependent phase, $\phi(t)$; and a carrier or center frequency ω_l. More practically, these complex field components can be absorbed into a complex field amplitude $\tilde{\mathcal{E}}(t)e^{i\omega_l t} = \mathcal{E}e^{i\phi_0}e^{i\phi(t)}e^{i\omega_l t}$. It is often convenient to work in the frequency domain with shifted frequency, $\Omega = \omega - \omega_l$.

1.3 Nonlinear Optical Frequency Conversion

With the advent of the laser in 1960 [20], suddenly large optical intensities with useful spatial modes were now available. This opened up a vast range of observable nonlinear optical effects. We now delve into what is considered the heart of this work: frequency conversion.

1.3.1 Three-wave mixing

To discuss nonlinear optical frequency conversion, we will need to investigate the electromagnetic interaction in a dielectric media with Maxwell's equations. Electric fields are coupled to the medium through the nonlinear polarization, $\mathbf{P}$ (not to be confused with the other wave "polarization" for the geometric oscillation of light). For the purposes of clarity here, we will first consider homogeneous isotropic media where $\mathbf{P}$ and $\mathbf{E}$ are always initially parallel thus individual

components can be related [19]. The nonlinear crystal of later interest in this work is instead of anisotropic geometry with symmetry about one crystal axis (uniaxial).

In Section 1.2, we introduced and manipulated only the temporal aspect of electric fields. Now, as we venture into three-wave mixing, the other spatial degrees of freedom are necessary. The wave propagation in a second-order nonlinear medium is governed by the wave equation

$$\nabla^2 \tilde{E} - \frac{\epsilon^{(1)}}{c^2}\frac{\partial^2 \tilde{E}}{\partial t^2} = \frac{1}{c^2}\frac{\partial^2 \tilde{P}^{\mathrm{NL}}}{\partial t^2} \tag{1.9}$$

where $\tilde{P}^{\mathrm{NL}} = \chi^{(2)}\tilde{E}^2 + \chi^{(3)}\tilde{E}^3 + \dots$ and $\epsilon^{(1)} = \epsilon_0(1+\chi^{(1)})$. Under these assumptions, $\chi^{(1)}$ is a scalar which is related to the medium's index of refraction by $n_\omega^2 = \epsilon^{(1)}(\omega)$. The $\chi^{(n)}$ within $\tilde{P}^{\mathrm{NL}}$ are tensors containing nonlinearity information for all combinations of frequency mixings along all directions. Since we are only interested in frequencies that are significantly smaller than the crystal's resonant frequencies, frequency dependence is effectively constant in the susceptibility tensor for the lossless medium at hand. This scenario is called the Kleinman symmetry condition [21]. As such, the tensor notation can be simplified to reflect the frequency independence by $d_{ijk} = \frac{1}{2}\chi^{(2)}_{ijk}$ where the indices are then contracted by $jk \to l$. Since we are interested in a fixed propagation and polarization (the wave geometric kind) direction, the nonlinear susceptibility can be reduced (after calculation) to a constant, d_{eff}. Further discussion on d_{eff} and crystal symmetries can be found in [21].

Now we assume propagation in the z-direction (as will be the assumption for the rest of this work). To do this, we include a position-dependent phase to the electric field. The wave equation of Eq. (1.9) can then be reduced according to $\nabla \to \frac{\partial^2}{\partial z^2}$.

Rewriting the single electric field of Eq. (1.6) for the superposition of the three fields ($n = 1, 2, 3$) yields[1]

$$\tilde{E}(z,t) = \frac{1}{2}\sum_n \left(\tilde{\mathcal{E}}_n e^{i\omega_n t}\right) e^{ik_n z}. \tag{1.10}$$

The second-order nonlinear polarization can similarly be written as

$$\tilde{P}^{\mathrm{NL}}(z,t) = \frac{1}{2}\sum_n P_n^{\mathrm{NL}}(z) e^{-i\omega_n t} + \text{c.c.} \tag{1.11}$$

where c.c. is the complex conjugate of the previous expression. To continue, we will look at two specific three-wave mixing combinations: sum-frequency conversion (SFG) and optical parametric oscillation (OPO), as depicted in Fig. 1.1.

[1] Due to the electric field definitions of Section 1.2, the following definitions include factor of 1/2, as explained in the footnote of Boyd [21, p. 7].

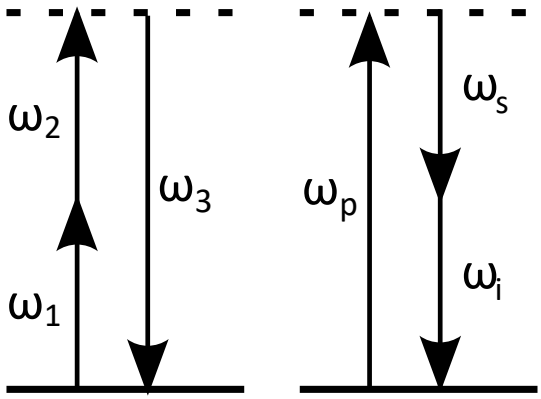

(a) SFG (b) OPO/SPDC

Figure 1.1: Three-wave mixing energy/frequency combinations and definitions for frequency conversion in this work.

Sum-frequency conversion

For the summation of two distinct frequencies $\omega_1+\omega_2=\omega_3$ of Fig. 1.1a, the nonlinear polarization is defined as

$$P_3^{\mathrm{NL}}(z)=P_3(z)e^{-i\omega_3 t} \tag{1.12}$$

for $P_3(z)=4d_{\mathrm{eff}}\tilde{\mathcal{E}}_1(z)\tilde{\mathcal{E}}_2(z)e^{i(k_1+k_2)z}$. Inserting Eq. (1.10) and Eq. (1.12) into the wave equation and gathering terms with the same time-dependence yields a set of three coupled differential equations. By invoking the slowly-varying envelope approximation of $|\frac{\partial^2\tilde{\mathcal{E}}_3}{\partial z^2}|\ll|k_3\frac{\partial\tilde{\mathcal{E}}_3}{\partial z}|$ for amplitude changes over a wavelength yields a simplified, first-order set of coupled differential equations

$$\frac{\partial\tilde{\mathcal{E}}_3}{\partial z}=\frac{2i\omega_3^2 d_{\mathrm{eff}}}{k_3c^2}\tilde{\mathcal{E}}_1\tilde{\mathcal{E}}_2e^{i\Delta kz} \tag{1.13}$$

$$\frac{\partial\tilde{\mathcal{E}}_1}{\partial z}=\frac{2i\omega_1^2 d_{\mathrm{eff}}}{k_1c^2}\tilde{\mathcal{E}}_3\tilde{\mathcal{E}}_2^*e^{-i\Delta kz} \tag{1.14}$$

$$\frac{\partial\tilde{\mathcal{E}}_2}{\partial z}=\frac{2i\omega_2^2 d_{\mathrm{eff}}}{k_2c^2}\tilde{\mathcal{E}}_3\tilde{\mathcal{E}}_1^*e^{-i\Delta kz} \tag{1.15}$$

for wavevector phase mismatch of $\Delta k=k_3-k_1-k_2$ and $\omega_1+\omega_2=\omega_3$. These equations can be solved given the appropriate assumptions [21] to yield an amplitude at the end of the nonlinear medium of

$$\tilde{\mathcal{E}}_3(L)=\frac{2i\omega_3 d_{\mathrm{eff}}}{k_3c^2}\tilde{\mathcal{E}}_1\tilde{\mathcal{E}}_2\left[\frac{e^{i\Delta kL}-1}{i\Delta k}\right] \tag{1.16}$$

for field amplitudes constants of $\tilde{\mathcal{E}}_1$ and $\tilde{\mathcal{E}}_2$. Given that the medium's nonlinearity d_{eff} is present in the amplitude (squared in the intensity), material nonlinearity has a large influence on frequency conversion efficiency.

The irradiance (radiant flux [W/m^2]) of the SFG light is defined as [21] $I_i = \frac{1}{2}\epsilon_0 n_i c|\mathcal{E}_i|^2$, which, after manipulation yields

$$I_3 \propto I_{\max}\text{sinc}^2\left[\frac{1}{2}\Delta kL\right] \tag{1.17}$$

leading for maximal frequency conversion for $\Delta k = 0$. The length over which the three waves can efficiently mix before becoming out of phase is

$$L_{\text{coh}} = \frac{2}{\Delta k}. \tag{1.18}$$

This condition can be met for the three frequencies by strategic crystal parameter choices.

The momentum phasemaching condition, $\frac{\omega_3}{c}n(\omega_3) - \frac{\omega_1}{c}n(\omega_1) - \frac{\omega_2}{c}n(\omega_2) = 0$, rewritten in terms of refractive indices, is not easily met due to frequency-dependence of the nonlinear medium. To reach appreciable phasematching conditions, three techniques are commonly used (most often in combination). First and most common, judicious tuning of birefringence, or the dependence of the refractive index on the direction of polarization of optical radiation [21], can allow for the phase mismatch to go to zero. Typically (though depending on the crystal structure) the highest frequency is polarized in the direction yielding the lowest refractive index. Second, temperature tuning, can, for some nonlinear crystals such as lithium niobate, be an effective method of minimizing the mismatch. Third, angle tuning of the crystal optic axis can sometimes provide enough wavelength-dependent difference to meet the phasematching condition. However, this solution can introduce problems as the three waves will "walk off" from each and lead to decreased efficiency over the interaction length. Used in conjunction with birefringence tuning, strategic cutting of the crystal with respect to its crystallographic optic axis, can allow for a phasematching solution.

Light polarized perpendicular to this optic axis (plane) is, by definition, the ordinary component in which the propagation speed is independent of the angle it makes with the crystal axis. Parallel light polarization to this optic axis is (perpendicular propagation to optic axis plane), by definition, is labelled extraordinary. By solving for the angle θ between the optic axis and $\mathbf{k}$ which yields a $n_e(\theta)$, the phasematching condition of $\Delta k = 0$ can sometimes be achieved.

Quasi-phasematching in periodically-poled media

A quick interlude in phasematching techniques before continuing with different three-wave mixing frequency conversion. The nonlinear medium of interest in this work, lithium niobate ($LiNbO_3$) has a relatively high accessible nonlinearity of 28 pm/V in comparison to other nonlinear crystals for frequency conversion from 532 nm→1064 nm+1064 nm. However, this high coefficient can only be accessed in the d_{33} tensor from all fields polarized the same way, which without birefringence phasematching, as previously mentioned, is inaccessible.

In 1964 it was theorized by Armstrong et al. [22] that by sandwiching together alternating, 180° rotated slices of a nonlinear crystal cut along its optic axis, the relative phase of the three waves could be corrected without requiring matching phase velocities (thus eliminating walk-off from non-parallel Poynting and wavevector propagation). By flipping the domain every time the polarization phase reaches a multiple of π, monotonic frequency conversion growth can be attained over the nonlinear medium interaction length. This was first demonstrated by Yamada et al. [23] in 1992 via a more feasible method of fabrication called periodic poling.

Fabrication is possible in such ferroelectric materials by patterning a periodic electrode on the surface of the crystal with high voltages large enough to reverse the domains in those regions [24].

Mathematically, this periodic modulation of spatial frequency $K_g = 2\pi/\Lambda$ leads a Fourier series $d(z) = \sum_m d_m e^{iK_m z}$ for different spatial harmonics $K_m = mK_g$. The square-wave modulation yields the Fourier coefficient $d_m = d_{\text{eff}} 2\sin(\pi D)/m\pi$ for duty cycle D. It can be seen that lower order harmonics lead to larger effective material nonlinearities. The optimal domain length, Λ, for these is the L_{coh} of Eq. (1.18). This process effectively shifts the phasemismatch $\Delta k = 0 \rightarrow \Delta k = \frac{2\pi}{\Lambda}$ to keep the three fields growing in phase over longer interaction lengths.

Optical parametric amplification

Another useful three-wave mixing configuration is optical parametric oscillation, as seen in Fig. 1.1b. This process is the combination of difference-frequency generation (DFG) between a strong ω_p and a weak ω_s to create the missing ω_i inside an optical cavity. From here, optical parametric amplification (OPA), takes the same strong ω_p and newly generated ω_i to amplify the lower frequency ω_s.

The coupled differential equations are

$$\frac{\partial \tilde{\mathcal{E}}_1}{\partial z} = \frac{2i\omega_1^2 d_{\text{eff}}}{k_1 c^2} \tilde{\mathcal{E}}_3 \tilde{\mathcal{E}}_2^* e^{i\Delta k z} \tag{1.19}$$

$$\frac{\partial \tilde{\mathcal{E}}_2}{\partial z} = \frac{2i\omega_2^2 d_{\text{eff}}}{k_2 c^2} \tilde{\mathcal{E}}_3 \tilde{\mathcal{E}}_1^* e^{i\Delta k z}. \tag{1.20}$$

Note the sign change in the wavevector mismatch phase. The gain of this process, in the presence of cavity feedback, allows for oscillation of the ω_s and ω_i frequencies of Fig. 1.1b.

The final three-wave mixing process of interest is spontaneous parametric down-conversion, also illustrated in Fig. 1.1b. Here, a strong, undepleted pump, ω_p frequency down-converts to similarly named signal and idler frequencies, in a comparable three-wave mixing process to OPA. However, conversely to OPA frequency conversion, there is no, even weak, initial ω_s. Looking at Eq. (1.19) and Eq. (1.20), there exists no initial amplitudes $\tilde{\mathcal{E}}_1$ or $\tilde{\mathcal{E}}_2$ thus this mathematical formalism breaks down. In the following section, we turn to a quantum optical description of this frequency conversion phenomena.

1.3.2 Quantum nonlinear optics - spontaneous parametric down-conversion

One of the key differences between the classical treatment of nonlinear optics and the quantum description arises from the quantized representation of the electric field[2]. Although this quantization procedure will not be reproduced here (many great resources exist [26–29]), the multimode quantized electric field (independent of polarization degrees of freedom) is [30]

$$\hat{E}^{(-)}(\mathbf{r},t) = \int d^2\mathbf{q}_\mu d\omega_\mu \mathcal{E}'_\mu e^{i\mathbf{k}\cdot\mathbf{r}+i\omega_\mu t}\hat{a}(\mathbf{r},t) \qquad \mu = s,i \tag{1.21}$$

where $\hat{a}(\mathbf{r},t)$ and $(\hat{a}^\dagger(\mathbf{r},t))$ are the lowering (and raising) mode operators of the quantum harmonic oscillator [28, 31]. The transverse mode wavevectors, $\mathbf{q}_\mu = (k_{\mu x}, k_{\mu y})$, and all quantization scaling factors are pulled into $\mathcal{E}'_\mu$ for signal and idler photons.

In the interaction picture, time evolution of a quantum system is determined by the Hamiltonian or total energy operator [32]. This electric field excitation of Eq. (1.21) and its hermitian conjugate (h.c.), $\hat{E}^{(+)}(\mathbf{r},t)$, make up the energy-conserving nonlinear interaction Hamiltonian of

$$\hat{H}_I(t) = \frac{\epsilon_0\chi^{(2)}}{2}\int_V d^3\mathbf{r}\hat{E}_p^{(+)}(\mathbf{r},t)\hat{E}_s^{(-)}(\mathbf{r},t)\hat{E}_i^{(-)}(\mathbf{r},t) + \text{h.c.} \tag{1.22}$$

The quantum state describing SPDC can be obtained from first-order perturbation theory of the above Hamiltonian.

$$|\Psi\rangle = e^{i\hat{H}_I t/\hbar}|\text{vac}\rangle \tag{1.23}$$

$$= |\text{vac}\rangle + \frac{i\epsilon_0\chi^{(2)}}{2\hbar}\int_0^t dt'\int_V d^3\mathbf{r}E_p^{(+)}(\mathbf{r},t)E_s^{(-)}(\mathbf{r},t)E_i^{(-)}(\mathbf{r},t)|\text{vac}\rangle + \ldots \tag{1.24}$$

Higher orders of terms represent double-pair, triple-pair etc. of spontaneous down-conversions. The integrals can be solved, as seen in other works [26, 27].

The functional SPDC state can be simplified to the competing effects of the near-monochromatic pump amplitude $\mathbb{A}_p(\mathbf{q}_p,\omega_s,\omega_i) = \exp\left[-\frac{1}{2}\mathbf{q}_p^2 w_p^2\right]\delta(\omega_p-\omega_s-\omega_i)$ and the crystal phasematching $\mathcal{S}(\omega_s,\mathbf{q}_s;\omega_i,\mathbf{q}_i) = Le^{i\Delta kL/2}\text{sinc}\left(\frac{\Delta kL}{2}\right)$.

$$|\Psi^{(2)}\rangle_{DC} = \mathcal{N}\int d^2\mathbf{q}_s d^2\mathbf{q}_i d\omega_s d\omega_i \mathbb{A}_p(\mathbf{q}_s+\mathbf{q}_i,\omega_s+\omega_i)\mathcal{S}(\omega_s,\mathbf{q}_s;\omega_i,\mathbf{q}_i)\hat{a}^\dagger(\mathbf{q}_s,\omega_s)\hat{a}^\dagger(\mathbf{q}_i,\omega_i)|\text{vac}\rangle \tag{1.25}$$

The spectral and spatial properties of such photon pair generation will be discussed in detail in the next chapter.

[2]Recently it has been suggested [25] that quantizing the electromagnetic displacement field $\mathbf{D}$ instead of electric field $\mathbf{E}$ preserves Faraday's law and affects the resulting amplitude weightings. Since the exact weightings for three-wave mixing conversion efficiency is not of concern in this work, I will proceed using the more traditional routes.

1.3.3 Biphoton frequency conversion

It is evident from Eq. (1.25) that SPDC photon pair is dependent on both energy and momentum conservation. In fact, these spectral and temporal properties are inseparable and unfactorable from each. It has been suggested that such an inseparable photon pair state could be considered as a *biphoton* [29].

It has been shown that such highly anti-correlated pair states allow for the two-photon interactions to scale linearly rather than quadratically in intensity [7, 33–35]. Such a nonlinear enhancement has been observed and manipulated at the single-photon level for both two-photon absorption and SFG [15, 36], among others.

The dependencies and experimental sensitivities of such a biphoton up-conversion can be seen through the following quantum frequency conversion.

Starting from Eq. (1.25), the up-converted photon state, $|\Psi^{(2)}\rangle_{\mathrm{UC}}$, can be found through a similar first-order perturbation of another Hamiltonian.

$$\hat{H}_{\mathrm{UC}}(t) = \frac{\epsilon_0 \chi^{(2)}}{2} \int_V d^3\mathbf{r} \hat{E}_u^{(-)}(\mathbf{r},t)\hat{E}_s^{(+)}(\mathbf{r},t)\hat{E}_i^{(+)}(\mathbf{r},t) + \mathrm{h.c.} \tag{1.26}$$

where $\mu = u$ represents the up-converted mode.

$$|\Psi^{(2)}\rangle_{\mathrm{UC}} = e^{i\hat{H}_{\mathrm{UC}}t/\hbar}|\Psi^{(2)}\rangle_{\mathrm{DC}} \tag{1.27}$$

$$= |\Psi^{(2)}\rangle_{\mathrm{DC}} + \frac{i\epsilon_0\chi^{(2)}}{2\hbar} \int_0^t dt' \int_V d^3\mathbf{r} E_u^{(-)}(\mathbf{r},t)E_s^{(+)}(\mathbf{r},t)E_i^{(+)}(\mathbf{r},t)|\Psi^{(2)}\rangle_{\mathrm{DC}} \tag{1.28}$$

Through further integration containing many intermediate variables and delta functions later, the final state, limited to first order, can be written as [9]

$$|\Psi^{(2)}\rangle_{\mathrm{UC}} = \left[\int d\omega_s \int d^2\mathbf{q}_s \mathcal{S}^*(\omega_s,\mathbf{q}_s;\omega_i,\mathbf{q}_i)\right] \hat{a}_u^\dagger(0,\omega_p)|\mathrm{vac}\rangle. \tag{1.29}$$

Here, the assumption has been made that phasematching properties between the two crystals are identical.

If biphotons propagated through some dispersive medium on the way to the second crystal, Eq. (1.29) would then contain an additional signal and idler dependent phase

$$|\Psi^{(2)}\rangle_{\mathrm{UC}} = \left[\int d\omega_s \int d^2\mathbf{q}_s \mathcal{S}^*(\omega_s,\mathbf{q}_s;\omega_i,\mathbf{q}_i) e^{i[\phi_s(\omega_s)+\phi_i(\omega_i))]}\right] \hat{a}_u^\dagger(0,\omega_p)|\mathrm{vac}\rangle \tag{1.30}$$

It is through this type of behaviour that biphotons have the ability to interfere with itself [37] and share a joint phase which is dependent on $\Delta kL/2$ [7, 38]. Because of energy conservation between signal and idler photons in the non-separable amplitude, the biphoton wavepacket behaves similarly to that of an ultrafast pulse when propagating through dispersive media.

Additionally, it is for this reason that coherent control can be imparted onto these biphotons via standard ultrafast optics pulse shaping tools which affects the temporal width of the intensity coherence properties[39]. Coherent control with biphotons has been demonstrated in pulse shaping tools such as spatial light modulators [8], prisms [13], commercial pulse shapers [40]. For this reason, the remaining sections of this chapter are dedicated to the study and manipulation of chromatic dispersion. Experimentally, it has been shown that unmatched dispersion from biphoton propagation prior to up-conversion through just over 1 mm of a PPLN crystal would reduced the biphoton up-conversion coincidence peak by 55% [9]. The typical biphoton up-conversion rates, despite optimal configurations, are still quite low at only 800-1000 counts/s. In addition to these low rates, the wavelength for the up-converted biphoton is by definition, the same as the powerful SPDC pump. This, as will be seen in a later chapter, leads to challenges in filtering out stray background light.

It is worth pointing out that for this biphoton frequency conversion to occur, the signal and idler photons from the same pair must both meet within the second nonlinear crystal. If one of the photons from the pair is lost, it can only incoherently up-convert (at much lower probabilities) [7]. For this reason, dispersion compensation should allow the highest transmission of the biphotons as possible. Choices for this will be discussed in further sections.

1.4 Chromatic Dispersion

A majority of this work relates to what happens when an electromagnetic wavepacket propagates through a frequency-dependent material. In some contexts, this effect on the wavepacket is nefarious and a problem to be solved, so tools will then be described as to solve it. In one particular circumstance, its effect can be turned into a useful characterization tool of its own. The remaining sections of this chapter mathematically draw clear the role of chromatic dispersion as a key player in this work.

Imagine a pulse of light localized in time, composed of multiple frequencies, such as the "white" light refracting through the prism in Fig. 1.2. As a whole, the pulse is slowed down to the speed known as the group velocity, v_g, when passing through a normally dispersive medium – that is, "bluer" frequencies travel slower than "redder" frequencies. In this medium, light is slowed down from its fastest unhindered speed in vacuum to a speed related to the dispersive properties of the medium. When such a light pulse passes through some frequency-dependent medium of refractive index $n(\omega)$, different frequencies will be delayed resulting in a longer, stretched pulse. This is due to the frequency-dependence of the group velocity, and known as the group velocity dispersion (GVD).

In the following sections we will mathematically expand upon these concepts, manifesting both in freespace and optical fiber, and point to ramifications and work-a-rounds for these effects

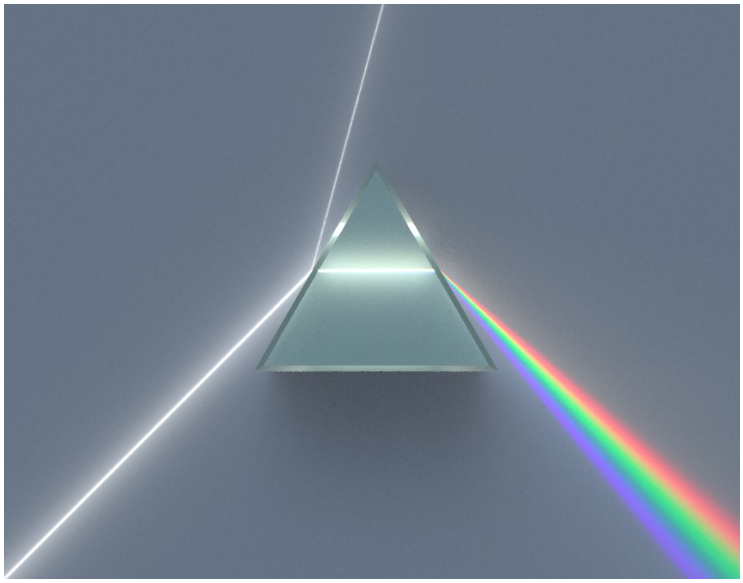

Figure 1.2: White light refracted through and reflected off of a prism.[3]

toward the main experimental goal of this work.

1.4.1 On slowing things down... – Group delay

The electromagnetic field passing through a dispersive medium acquires an optical phase related to

$$\phi(\Omega) = k(\Omega)L \tag{1.31}$$

where k is the momentum wavevector and L is the length of medium. It is this wavevector, $k = \frac{(\Omega-\omega_l)n(\Omega-\omega_l)}{c} = \frac{2\pi n(\lambda)}{\lambda}$, which when Taylor expanded, yields the source of a few dispersive medium effects.

$$k(\Omega) = k(\omega_l) + \left.\frac{dk}{d\Omega}\right|_{\omega_l}(\Omega-\omega_l) + \left.\frac{d^2k}{d\Omega^2}\right|_{\omega_l}(\Omega-\omega_l)^2 + \dots \tag{1.32}$$

The first-order coefficient is defined as the inverse group velocity, which varies with the central frequency.

$$v_g = \left(\left.\frac{dk}{d\Omega}\right|_{\omega_l}\right)^{-1} = \left(\frac{n_0}{c} - \frac{\lambda}{c}\left.\frac{dn}{d\lambda}\right|_{\lambda_l}\right)^{-1} \tag{1.33}$$

This decreased velocity in the medium (with respect to c, the speed of light in vacuum) can also be represented as a group delay

$$\tau_g = \frac{L}{v_g} = \left(\left.\frac{dk}{d\Omega}\right|_{\omega_l}\right)L. \tag{1.34}$$

[3] Dispersive_Prism_Illustration_by_Spigget.jpg: Spigget derivative work: Cepheiden (talk) (https://commons.wikimedia.org/wiki/File:Dispersive_Prism_Illustration.jpg), "Dispersive Prism Illustration", https://creativecommons.org/licenses/by-sa/3.0/legalcode

It is due to these frequency-dependent time-delay reasons that free-space propagation through air will be mainly considered. However for some strategic reasons, as we will see later, these concepts of group delay and group velocity dispersion will also be considered in optical fiber. We will only consider single-mode, step-index optical fibers, where the wavelength- (or frequency-) dependent delay of the envelope is not only dependent on the medium (germanium-doped silica glass), but the confinement effects of the step-index waveguide.

A step-index optical fiber is a cylindrically symmetrical waveguide where a "core" of refractive index n_1 is surrounded by a "cladding" of index n_2 for $n_1 > n_2$. Waveguide propagation is maintained by total internal reflection if the angle of incidence at the core-cladding boundary is greater than the critical angle $\theta_c = \sin^{-1}(n_2/n_1)$. Alternatively written, this condition is maintained for ray propagation angle θ with respect to the fiber axis meets $\theta < \pi - \theta_c$ [19].

The electromagnetic solutions for propagation in a cylindrical waveguide are known as modes. Mathematically, they are solutions to the Helmholtz equation solved for cylindrical symmetry of dielectric media of refractive index $n(r)$. This refractive index profile for a step-index fiber is $n(r) = n_1$ within the core ($r < a$) and $n(r) = n_2$ in the cladding ($r > a$). Given these boundary conditions, the solutions to the Helmholtz equation are Bessel functions of the first- ($J_l(x)$) and second- ($K_l(x)$) kind for the core and cladding, respectively [41]. Under the assumptions that the solutions are continuous and have continuous derivatives at $r = a$, single-mode propagation can be found from solving the characteristic equation

$$\kappa \frac{J_1(\kappa a)}{J_0(\kappa a)} = \gamma \frac{K_1(\kappa a)}{K_0(\kappa a)} \tag{1.35}$$

for transverse core propagation constant $\kappa = (n_1^2 k_0^2 - \beta^2)^{1/2}$ and cladding decay parameter $\gamma = (\beta^2 - n_2^2 k_0^2)^{1/2}$ for $k_0 = 2\pi/\lambda$ [41]. This equation can be solved graphically by plotting left and right sides and finding the intersections. Given these results, κ and thereby all other constants can be determined.

Material dispersion arises out of the wavelength-dependent core and cladding refractive indices. The group delay (per unit length) can be computed from [41]

$$\hat{\tau_g} = \frac{d\beta}{d\omega} = -\frac{\lambda^2}{2\pi c}\frac{d\beta}{d\lambda}. \tag{1.36}$$

This result contains group delay influences from both material and waveguide. Group delay can be related to group velocity by $L/\hat{\tau}_g$.

1.4.2 ...And stretching things out – Group velocity dispersion

The second-order coefficient of Eq. (1.32) represents the group velocity dispersion[4].

$$k'' = \left(\frac{d^2k}{d\omega^2}\right)_{\omega_l} = \frac{\lambda_l^3}{2\pi c^2}\left(\frac{d^2n}{d\lambda^2}\right)_{\lambda_l} \tag{1.37}$$

This parameter represents the medium's ability to impart a frequency-dependent group delay which leads to the pulse or wavepacket spreading in time. When this parameter is multiplied by the length of medium L, the quantity then represents the group delay dispersion (GDD), $k''L$. This stretching in the time domain has no effect on the spectral domain in this work.

For $k'' > 0$, the medium is said to have normal dispersion. For $k'' < 0$, the medium has anomalous dispersive properties. In terms of pulse stretching, both normal and anomalous dispersion will temporally broaden a transform limited wavepacket after propagation through the medium. However, in a normally dispersive medium, the "bluer" frequency components will lag behind the "redder". With anomalous dispersion, the opposite is true: "redder" frequency components will lag behind the "bluer".

Depending on which context GVD is used in, the units used to represent this quantity differ. In optical fiber, due to the convenient low material loss window in silica bounded by Rayleigh scattering and infrared absorption [19], telecommunication systems often operate in the bands from approximately 1260 nm to 1660 nm which are consequently known as the "telecom bands". Since this loss is so low in telecom optical fiber, GVD is specified in units of [ps/km-nm]. A majority of this work will use units of $[\mathrm{fs}^2/\mu m]$ common to ultrafast optics.

Group velocity dispersion in optical fibers, similar to the discussion on group velocity, has both material and waveguide dependencies. When core a is small, the index of refraction difference between cladding n_2 and core n_1 has great effect [41]. Similar to the group delay arising from single-mode propagation, the group velocity dispersion parameter can be obtained via derivative with respect to wavelength

$$D = \frac{d\hat{\tau_g}}{d\lambda}. \tag{1.38}$$

Between the material and waveguide contributions, the material GVD sets the behaviour whereas varying waveguide confinement shifts this curve in wavelength [19].

1.4.3 Tools for manipulating dispersion

Having the ability to manipulate dispersion can allow for properties of coherent ultrafast pulses to be tuned and extracted. First, dispersion manipulation via a prism compressor, an essential tool in ultrafast optics, will be discussed to tune and compensate the GDD that is acquired through

[4]One should always be clear on which definition they are using for group velocity dispersion. The group-velocity dispersion parameter is also known as $k'' = d/d\omega(1/v_g)$ and $dv_g/d\omega$ [42]

optical elements in the setup. Then finally, the use of dispersion as a tool to deduce single-photon spectral properties will also be discussed.

Prism compressor

To attain the largest temporal intensity or peak power, the optical pulse or wavepacket should be transform-limited in time. Since almost every optical component induces material dispersion, maintaining femtosecond-timescale pulses at the point of interest requires compensation for these acquired spectral phases. The most common method of inducing negative GDD is through continuous, frequency-dependent angular dispersion [18]. This idea was first implemented using diffraction gratings [43] then later extended to pairs of prisms [44].

Since high throughput is of highest priority, angular dispersion implemented through prism refraction is the better, low loss choice. There are many good resources for ray tracing the generate geometric and material dispersion through a prism compressor [45, 46], though [18] will be followed here.

Building off of the previous ideas of chromatic dispersion, we now model the spectral modification of a wavepacket transmission through a linear optical element with the transfer function, $\tilde{H} = R(\Omega)e^{i(\Phi(\Omega))}$. An electric field passing through such an optical element, represented in polar form, is

$$\tilde{E}(\Omega) = R(\Omega)e^{-i\Phi(\Omega)}\tilde{E}_{\text{in}}(\Omega) \tag{1.39}$$

where for our interests, the optical element (optimized for the frequency range of interest) has minimal effect on the amplitude, where $R(\Omega) \approx 1$.

A prism compressor can similarly be described by a linear transfer function which imparts a tunable second-order phase "chirp" to the wavepacket in frequency. The phase of this transfer function can be modelled as $\Phi_{\text{PC}}(\Omega) = \frac{\Omega}{c}OPL(\Omega)$ where, due to angular dispersion, the optical path length, $OPL(\Omega)$, is frequency-dependent. Since we require maximal transmission, the prisms are set up at Brewster's angle of $\theta_B = \tan^{-1}\left(\frac{n_2}{n_1}\right)$. If the electric field incident from one medium to the other is transverse magnetic ("horizontally polarized" in the lab reference frame), the reflection goes to zero[5]. Using this simplification of equal incident and outgoing beam angles for all four prisms of a standard prism compressor (Fig. 1.3a), the resulting GDD imparted by a prism compressor is [18]

$$\left.\frac{d^2\Phi_{\text{PC}}}{d\Omega^2}\right|_{\omega_l} = \frac{\lambda_l^3}{2\pi c^2}\left[L_g \left.\frac{d^2n}{d\lambda^2}\right|_{\lambda_l} - \left(4L + \frac{L_g}{n^3}\right)\left(\left.\frac{dn}{d\lambda}\right|_{\lambda_l}\right)^2\right]. \tag{1.40}$$

[5]This condition is experimentally obtained by observing the reflection and rotating the prism until the reflect spot is at the angle of minimum deviation with respect to the incident beam [47].

L	Apex-to-apex prism distance
L_g	Optical path length through prism glass
h	Prism insertion measured from prism apex
θ_B	Brewster's angle $=\arctan[n(\lambda)]$
α	Prism apex angle

Table 1.1: Prism compressor parameters as defined in Fig. 1.3a.

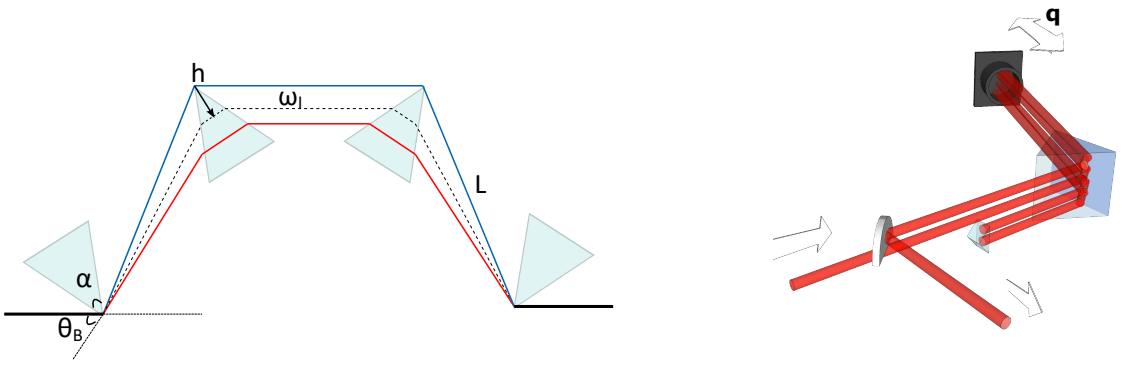

(a) Unfolded prism compressor

(b) Folded prism compressor

Figure 1.3: Prism compressor experimental design and variable definitions. Due to folding with retroreflector, $L = 2q + \delta_{\mathrm{RR}}$ with δ_{RR} being the constant internal retroreflector path length.

One of the downsides of prism compressors, in comparison to diffraction grating-based pulse compressors, is the unwieldly large inter-prism distances L needed to achieve relatively small amounts of chromatic dispersion. As such, it is common to reduce the optical table footprint of the prism compressor by using a mirror at the half-way point and folding it back over the same two prisms. It has been shown by Akturk et al. [48] that there are additional benefits to halving yet again the two-prism prism compressor to that of a single prism, as seen in Fig. 1.3b. With a quadruple-pass prism compressor, it is possible to reduce the potential pulse distortions (pulse tilt/sheering/magnification [49]) of prism misalignment by having symmetry between incident and exit angles.

The simulated dispersion sensitivities of a quadruple-pass prism compressor (Eq. (1.40)) for different parameters are shown in Fig. 1.4. It is useful to note that prism insertion, h, can tune large amounts of GDD with millimeters of translation (100 fs^2/mm). As a comparison, the practical inter-prism distance, q, (as defined $q = 1/2(L + \delta_{\mathrm{RR}})$ for variables defined in Fig. 1.3a) tunes GDD at about a fifth of h (-21 fs^2/mm).

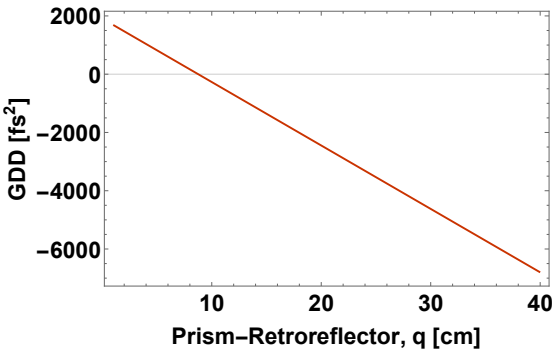

(a) Angular dispersion path length dependence

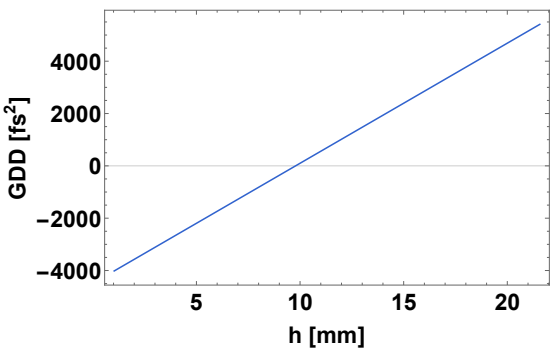

(b) Prism insertion dependence

Figure 1.4: Theoretical GDD dependencies on prism compressor parameters for the prism compressor shown in Fig. 1.3b.

Fiber Spectrometer

Due to the frequency-dependent refractive index of fused silica-based optical fibers, pulses with different central frequencies will travel at different group velocities. This results in a measurable, frequency-dependent time-delay. Due to the high dispersion of very long optical fibers, different monochromatic frequencies comprising the optical pulse will each experience a frequency-dependent time delay resulting in a "stretched pulse". This, in addition to frequency-dependent waveguide confinement contributes to what is called the group velocity dispersion [19, 41].

If the fibers are long enough (such that it's in the dispersion "far-field zone" [50]), with detectors of high enough temporal resolution and detection efficiency, time-domain measurements can yield frequency information about the pulses (or SPDC photons). This is made possible by the propagation of pulses through chromatic dispersion to yield a Fourier transform from time to frequency [19, 50]. Additionally, this fiber spectrometer method is particularly advantageous for the single-photon telecom regime since optical fibers exhibit low loss. Furthermore, most other InGaAs-based spectral characterization tools suffer quite low efficiencies resulting in time-consuming tuning curve characterizations.

1.5 Measuring Dispersion Through Interferometry

Ultrafast optical tools are of limited use unless their performance is verified. We turn now to white light interferometry to evaluate the affected spectral phase of an electric field. Interferometry has to do with the addition of an electric field amplitudes with respect to a displaced portion (in one form or another) of the same field. If, at the output of an interferometer, intensity fringes are observed, then the light source is said to be coherent. In the present interferometry application, we are interested in first-order coherence of electric field amplitudes rather than of intensities. A

further discussion of first- and second-order coherence in relation to this work's ultimate goal of biphoton up-conversion can be found in [51].

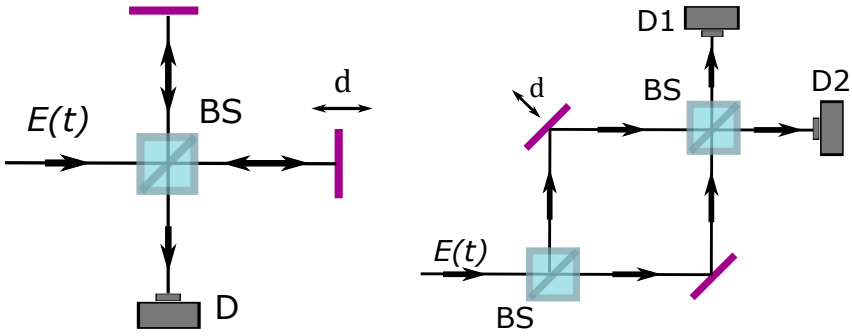

(a) Michelson interferometer (b) Mach-Zehnder interferometer

Figure 1.5: Two common interferometer configurations where BS is 50:50 beamsplitter; D is a detector; and d is a mirror translation.

Coherence can be observed in multiple forms. In Young's double-slit experiment, spatial coherence of the electric field amplitude is observed in the form of fringes on a viewing screen. Temporal coherence of a temporally delayed, though otherwise similar, electric field can be measured on a Michelson interferometer [42], as seen in Fig. 1.5a. A combination of spatial and temporal displacements can be implemented in what is called a Mach-Zehnder interferometer, displayed in Fig. 1.5b. Although only classical optics will be considered in this present application of spectral phase extraction, interferometry can be a useful tool for measuring temporal coherence single-photon wavepackets (using a Michelson interferometer) and photon pair wavepackets (using a Mach-Zehnder interferometer) [52]. In this thesis, both these types of interferometers are used, depending on different experimental constraints. An important experimental metric in interferometry is visibility. This fringe sharpness metric is calculated by $V = \frac{I_{\max} - I_{\min}}{I_{\max} + I_{\min}}$.

1.5.1 There and back again: optical phase and interference

To see how the GDD parameter from previous sections can be measured with interferometry, we now mathematically describe such a white light interferometer [42]. For simplicity, let us consider a Michelson interferometer, as seen in Fig. 1.5a, with the following three electric fields before and after the beamsplitter: initial $\tilde{E}(t)$; delayed $\tilde{E}_1(t-\tau)$; and undelayed $\tilde{E}_2(t)$. For simplicity, we will work with the shifted frequency variable $\Omega = \omega - \omega_l$ with the electric fields

$$2\tilde{E}(\Omega + \omega_l) = \tilde{\mathcal{E}}(\Omega) = \int_{-\infty}^{\infty} \tilde{\mathcal{E}}(t) e^{-i\Omega t} dt \tag{1.41}$$

$$\tilde{\mathcal{E}}(t) = \frac{1}{2\pi} \int_{-\infty}^{\infty} \tilde{\mathcal{E}}(\Omega) e^{i\Omega t} d\Omega. \tag{1.42}$$

Upon recombination at the beamsplitter, the intensity output of the Michelson interferometer is

$$I(\tau) \propto \langle \tilde{\mathcal{E}}_1^2(t-\tau)\rangle + \langle \tilde{\mathcal{E}}_2^2(t)\rangle + \langle \tilde{\mathcal{E}}_1(t-\tau)\tilde{\mathcal{E}}_2^*(t)\rangle e^{-i\omega_l\tau} + \langle \tilde{\mathcal{E}}_1^*(t-\tau)\tilde{\mathcal{E}}_2(t)\rangle e^{i\omega_l\tau} \tag{1.43}$$

where the angled brackets denote time averaging. Of particular interest are the third and fourth terms of Eq. (1.43) which contain electric field envelopes from both interferometer arms. These we will define as the first-order cross correlations[6]

$$\begin{aligned}\tilde{A}_1(\tau) &= \langle \tilde{\mathcal{E}}_1^*(t-\tau)\tilde{\mathcal{E}}_2(t)\rangle e^{i\omega_l t} \\ &= \mathcal{A}_1^+(\tau)e^{i\omega_l\tau}\end{aligned} \tag{1.44}$$

with $\tilde{A}_2(\tau)$ being similarly defined. The correlation terms from each interferometer output provide complementary information. For that reason, we'll pursue only positive spectral components ($e^{i\omega_l\tau}$) as the negative spectral components ($e^{-i\omega_l\tau}$) contain no new information.

Utilizing cross correlation properties of the Fourier transform and other embedded definitions, the field correlation can be reduced to

$$\begin{aligned}\tilde{A}_1^+(\Omega) &= \int_{-\infty}^{\infty} \tilde{A}_1^+(\tau)e^{-i\omega\tau}d\tau \\ &= \tilde{E}_1^*(\omega)\tilde{E}_2(\omega)\end{aligned} \tag{1.45}$$

or, more conveniently in shifted frequency,

$$\begin{aligned}\mathcal{A}_1^+(\Omega) &= \tilde{\mathcal{E}}_1^*(\Omega)\tilde{\mathcal{E}}_2(\Omega) \\ &= |\tilde{\mathcal{E}}(\Omega)|^2\end{aligned} \tag{1.46}$$

That pleasant jaunt through electric field and embedded Fourier transform definitions is not without cause. If each interferometer arm is perfectly balanced with $\tilde{\mathcal{E}}_1(\Omega) = \tilde{\mathcal{E}}_2(\Omega)$, and with $\tau = 0$ time difference between the two arms, then the resulting cross correlation is the spectral intensity, $|\tilde{\mathcal{E}}(\Omega)|^2$. This result is known as a Fourier spectrometer, and it is both an interesting and a useful tool.

Now, let some sample of glass be placed in one of the interferometer arms. This piece of glass affects the electric fields by some amplitude and phase modification, mathematically described by an optical transfer function $T(\Omega)e^{ik(\Omega)}$. The amplitude modification for optically transparent glass samples is assumed to be $T(\Omega) \approx 1$. The spectral phase, which will be of interest later, arising from the sample of thickness $d/2$ is defined as $k_l = \frac{2\pi n(\lambda_l)}{\lambda_l} = \frac{\omega_l n(\omega_l)}{c}$. If this sample was placed in arm 2, then the resulting electric field envelope would be

$$\tilde{\mathcal{E}}_2(\Omega) = T(\Omega)\tilde{\mathcal{E}}_1(\Omega)\exp\left[-id\left(k(\Omega) - \frac{\Omega+\omega_l}{c}\right)\right] \tag{1.47}$$

[6]The modulus of this "mutual coherence" term is an alternative definition to the fringe visibility.

where the term $-\frac{(\Omega+\omega_l)n_{\text{air}}}{c}$, for $n_{\text{air}} \approx 1$, is the term that enforces the phase due to traversing there and back through air is not double-counted over the sample's thickness $d/2$.

We turn now to the first-order cross-correlations from the interferometer outputs. In total, with the sample and realistic amplitude losses, the other cross-correlation term, $\tilde{\mathcal{A}}_2^+(\Omega)$ is

$$\mathcal{A}_2^+(\Omega) = \tilde{r}_{12}(\Omega)|\tilde{\mathcal{E}}(\Omega)|^2 T(\Omega) \exp\left[-id\left(k(\Omega) - \frac{\Omega+\omega_l}{c}\right)\right]. \tag{1.48}$$

Now by conveniently dividing Eq. (1.48) by Eq. (1.46), additionally multiplied by a complex, frequency-dependent function $\tilde{r}_{12}(\Omega)$ representing amplitude losses and any unbalanced phase shifts in the two arms of the interferometer, yields an isolated spectral phase in the interference fringes. Taylor expansion of $k(\Omega)$, as we will utilize later, allows for GDD=$k''L$ of Eq. (1.37) to be extracted from a polynomial fitting of this unwrapped spectral phase.

Chapter 2

Source of Energy-Time Correlated Photon Pairs

2.1 Energy-Time Entangled Photon Pair Source

Sources of energy-time correlated photon pairs need to be developed and characterized in order to utilize quantum correlations in advanced metrology and spectroscopy techniques. These photon pairs, generated from spontaneous parametric down-conversion (SPDC), maintain strict, non-separable conservation of energy and conservation of momentum, which has been demonstrated to be advantageous for applications in quantum metrology and spectroscopy [7]. Additionally, these SPDC photon pair sources inherently show some sort of correlation in frequency. This correlation can be adjusted by strategic engineering of the phasematching function, $\mathcal{S}(\omega_s, \omega_i)$, for applications such as quantum computing [53] and quantum communication [54]. For example, by clever poling period design [55, 56] or material dispersion matching [57], the signal and idler frequency correlation can be tuned to near frequency uncorrelation which is highly sought after when working with other high-purity photonic degrees of freedom. Since we are interested in two-photon quantum frequency conversion, most attention will be to this particular energy-time degree of freedom.

Strong biphoton frequency anti-correlations arise from a spectrally narrowband pump amplitude, $\mathcal{E}(\omega_p)$. This effectively bounds the up-converted spectral bandwidth or resolution of which the signal and idler photons could combine into [7]. As long as the pump spectral bandwidth is within that of the acceptance bandwidth of the up-conversion crystal phasematching or absorption band, the pump laser choice is adequate. Additionally, the pump laser choice has temporal consequences. Narrowband continuous wave (cw) lasers pumping SPDC create biphotons which coherently behave as ultrashort pulses [7, 38] which is beneficial for nonlinear two-photon processes. The pulse-like behaviours from these cw-pumped biphotons will later require the utilization of ultrafast optical dispersion compensation tools to remain transform-limited for two-photon

quantum frequency conversion goal, as discussed in later chapters.

In addition to these physical photon pair source requirements, I chose the SPDC wavelength conversion of 532 nm→1064 nm+1064 nm, from the availability of a <5 MHz linewidth cw Nd:YAG laser [Coherent Verdi V-18] and for the potential application of the photon pair source with commonly used two-photon fluorophores in the NIR. Additionally, this laser offered the availability of very high optical powers and excellent beam quality due to the original laboratory purpose of pumping (up to two) Ti:Sapphire laser oscillators. This was a very important feature as even with the more nonlinear crystal of PPLN, frequency conversion rates are still low, let alone back-to-back frequency conversions. To combat the low frequency conversion rates, high pump laser power (1 W) was employed which resulted in ≈ 100 nW of down-conversion photon pairs. This macroscopically measurable flux is still considered "single-photon-level" as the frequency modes contained within the 60 nm spectral bandwidth exceeds that of the generated photon flux, or less than one photon per frequency mode. This condition bounds the maximal photon flux at $\Phi_{\max} = \Delta\omega = 10^{14}$ photons/s (18 μW) [8]. Additionally, as previously discussed, the temporal coherence of these biphotons are on the 10s of fs – inversely proportional to the spectral bandwidth [8] – which requires the rate of photon pair emission to exceed this to eliminate chance of overlap (corresponding to > 6 μW of photon flux). This crystal and laser choice has been demonstrated for biphoton frequency conversion by [9, 13].

However, there are some physical consequences to such high pump powers. Lithium niobate is known for its lower damage threshold (compared to PPKTP) against photorefractive damage [24, 58], although with the 5% doping of MgO this has been shown to be reduced [59]. In particular, this wavelength combination of 532 nm and 1064 nm is especially detrimental due to green-induced infrared absorption (GRIIRA) [24, 60] however this can be somewhat reduced by high (> 100°C) crystal operating temperatures [59, 61]. Additionally, increasing the pump waist size in the crystal can lower the power density (at the cost of conversion efficiency), though, as discussed later, this may result in some beneficial spatial down-conversion properties.

2.2 Type-0 SPDC in Bulk PPLN

We turn now to spatially and spectrally characterizing Type-0[1] SPDC. First, a theoretical model is outlined with a practical thought of simulating experimental data. Next, experimental characterizations are compared with the simulated theory. Finally, a simple, novel method for joint spectral and spatial SPDC characterization is proposed, demonstrated, and compared with simulated theory.

[1] Type-0 refers to the polarization orientation of the three waves in the frequency conversion process where the pump, signal, and idler waves are extraordinarily polarized with respect to the crystal's optical axis (*eee*), as defined in Section 1.3.1.

2.2.1 Theoretical models

Following from the discussion SPDC in Section 1.3.1, the spatial and spectral emission properties can be simulated by appropriate integration of the restricting functions representing the crystal's phasematching function, $\mathcal{S}(\omega_s, \mathbf{q}_s; \omega_i, \mathbf{q}_i)$, and the pump amplitude, $\mathbb{A}_p(\mathbf{q}_p, \omega_p)$. In this work, the vector $\mathbf{q} = (k_x, k_y)$ is taken to distinguish the biphoton wavevector components which are in the plane perpendicular to propagation, as seen in Fig. 2.1b.

As stated previously, the crystal phasematching function is dependent on the wavevector mismatch, Δk, between the three electric fields and the crystal's periodic poling, Λ.

$$\mathcal{S}(\omega_s, \mathbf{q}_s; \omega_i, \mathbf{q}_i) = \mathcal{N}\sqrt{\omega_s \omega_i}\text{sinc}\left(\frac{\Delta k L}{2}\right) \tag{2.1}$$

$$\Delta k = \mathbf{k}_p - \mathbf{k}_s - \mathbf{k}_i - \frac{2\pi}{\Lambda} \tag{2.2}$$

where $\mathbf{k}_p = (\mathbf{q}_p, k_{pz})$ and $\mathcal{N}$ is a normalization coefficient containing the nonlinear electric susceptibility of the three-wave mixing interaction [62]. Due to the spectrally broadband nature of the down-conversion photon pair emission, the dispersive nature of the lithium niobate crystal for the noncollinear wavevectors, $\mathbf{q} = (k_x, k_y)$, must be taken into account [63]:

$$k_z(\mathbf{q}, \omega) = n_o(\omega)\sqrt{\frac{\omega_0^2}{c^2} - \frac{\mathbf{q}^2}{n_e(\omega)^2}}. \tag{2.3}$$

For simulating these quantities, a temperature- and wavelength-dependent refractive index is required. In this work, the Sellmeier equation representing the refractive index of MgO:PPLN was that provided by Gayer et al. [64] though recent studies have produced this new, high temperature Sellmeier equation [65]. Other important temperature dependent quantities useful for simulation include the poling period, $\Lambda(T)$, and crystal length, $L(T)$ [66].

The final factor shaping the down-conversion emission is from the pump amplitude, $\mathbb{A}_p(\mathbf{q}_p, \omega_p)$, which, due to the near-monochromatic nature of the SPDC investigated here, enacts the condition of energy conservation through that of a delta function in frequency,

$$\mathbb{A}_p(\mathbf{q}_p, \omega_s, \omega_i) = \exp\left[-\frac{1}{2}\mathbf{q}_p^2 w_p^2\right]\delta(\omega_p - \omega_s - \omega_i) \tag{2.4}$$

and a Gaussian in the pump field's spatial distribution, dependent on pump waist w_p. This can be combined into the spectral density as

$$\Psi(\omega_s, \mathbf{q}_s; \omega_i, \mathbf{q}_i) = \mathbb{A}_p(\mathbf{q}_s + \mathbf{q}_i, \omega_s + \omega_i)\mathcal{S}(\omega_s, \mathbf{q}_s; \omega_i, \mathbf{q}_i). \tag{2.5}$$

Using these definitions, the measured intensity can be calculated through integration over the relevant spatial and spectral ranges. The spectral emission, as measured by an optical spectrum analyzer, can be obtained via

$$I(\omega_s) \propto \int d\omega_i \int_{-|\mathbf{q}_{\text{lens}}|}^{|\mathbf{q}_{\text{lens}}|} d\mathbf{q}_s d\mathbf{q}_i |\mathcal{F}_{\text{eff}}(\omega_i)\Psi(\omega_s, \mathbf{q}_s; \omega_i, \mathbf{q}_i)|^2, \tag{2.6}$$

where the spatial integration is bounded by the perpendicular wavevector obtained by the limiting numerical aperture of the collection optics. Further discussion on choosing parameters to simulate experimental data can be found in Appendix B.2.2.

The spatial intensity distribution, as measured by a spatially-resolved detector or camera, can be computed by the following integral:

$$I(\mathbf{q}_s) \propto \int_{-|\mathbf{q}_\mathrm{w}|}^{+|\mathbf{q}_\mathrm{w}|} d\mathbf{q} \int d\omega_s d\omega_i |\mathcal{F}_\mathrm{eff}(\omega_s,\omega_i)\mathcal{F}_\mathrm{bp}(\omega_s,\omega_i)\Psi(\omega_s,\mathbf{q}_s;\omega_i,\mathbf{q}_i)|^2. \tag{2.7}$$

where the bounds of the integration in momentum-space is up to $|\mathbf{q}_\mathrm{w}|$ of the pump waist divergence angle in the nonlinear crystal and the frequency bounds over silicon's absorption efficiency range, represented by the function, $\mathcal{F}_\mathrm{eff}(\omega)$. Because, in the case of implementation here, the wavelength-dependent detection efficiency dropped so significantly over the spectral region of interest, spectral discrimination was limited by a spectral bandpass filter, $\mathcal{F}_\mathrm{bp}(\omega)$.

2.2.2 Spectral and spatial source characterization

Moving from theory to practice, I now present the spatial and spectral characterization results of a 5 mm crystal of MgO:PPLN for 532 nm→1064 nm+1064 nm SPDC.

Given the pre-existing knowledge of the noncollinear emission behaviour of the collinearly phasematched SPDC source, I chose a short, 11 mm focal length aspheric lens to capture photon pair emission up to a large opening angle and to facilitate uniformity between spatial and spectral characterizations, as seen in Fig. 2.1a.

Spectral

The photon pairs to be measured were created from pumping a 5 mm PPLN crystal with 1 W of continuous wave light, as seen in Fig. 2.1a. Spectral filtering removed the strong pump and allowed the remaining photon pairs to be fiber coupled into a multimode optical fiber and measured on an optical spectrum analyzer [Anritsu MS9710B].

These experimental results are used to determine more exact parameter choices for the simulated phasematching curves. A method for parameter choice in matching theory to experiment is found in Appendix B.2.2. Given the resulting phasematching parameters, shown in Table 2.1, integration of Eq. (2.6) over each experimental crystal temperature resulted in well-agreeing simulated spectra. Fig. 2.2 shows the simulated spectral FWHM bandwidths (as light-colored bars) and central daughter photon frequencies overlaid the experimental phasematching (density plot).

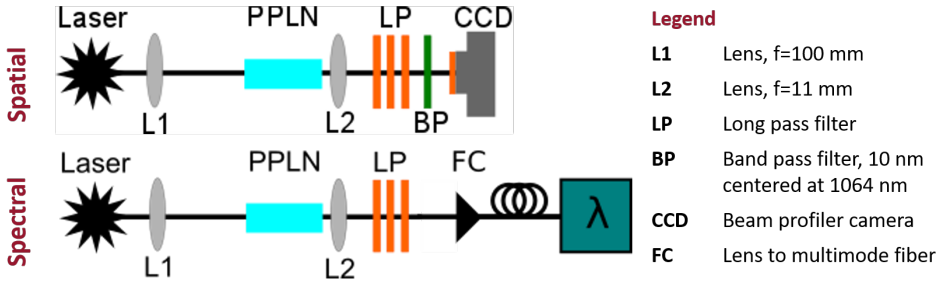

(a) Spatial and spectral characterization setups

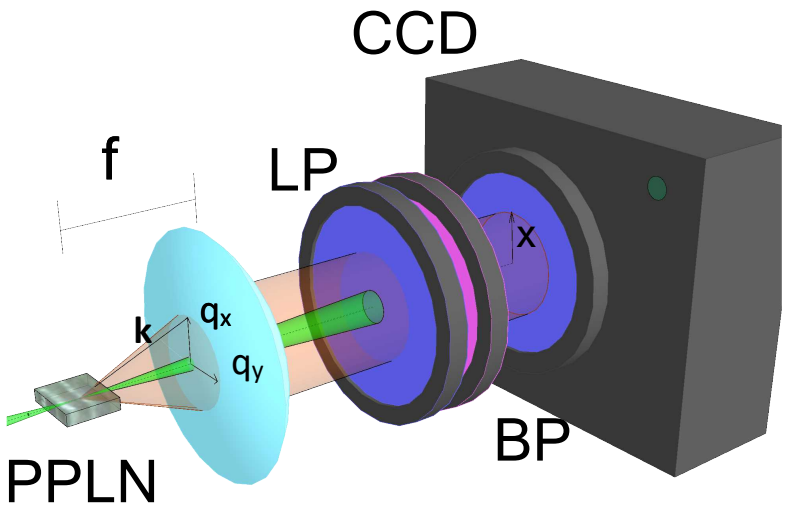

(b) Spatial wavevector definitions

Figure 2.1: PPLN characterization setups for spatial and spectral down-conversion properties.

Spatial

The spatial characterization, conceptualized in Fig. 2.1b, was performed for temperatures *beneath* the degenerate temperature of Fig. 2.2. This reasoning becomes evident when compared with the raw beam profiler images of Fig. 2.3. Here, since the CCD beam profiling provides no spectral discrimination beyond the it's nonuniform detection efficiency, I imparted spectral information onto the spatial measurement with a 10 nm FWHM bandpass filter. This allowed me to investigate the temperature-dependent spatial behaviour of the central down-conversion wavelength.

To reiterate, the noncollinear photon pair spatial properties beneath degenerate, collinear frequency conversion configuration are investigated. This took the form of spatial "donuts" or "cones" comprised of a specific Gaussian spectral distribution of radius $\mathbf{r}$, or, as converted to

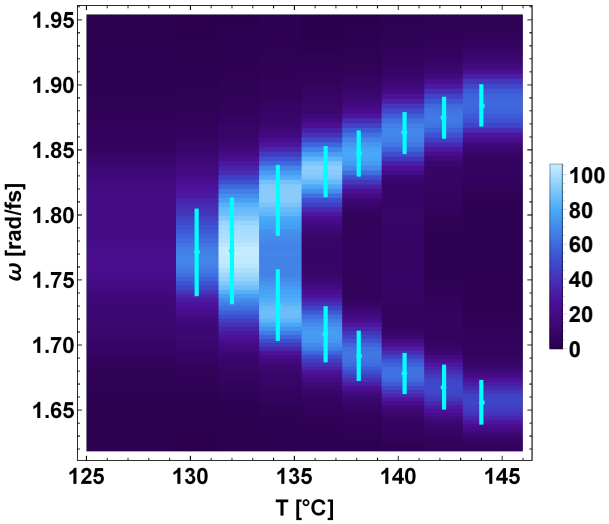

Figure 2.2: Measured phasematching spectrum of experiment (density plot) and simulation (light-colored bars, full-width half-maximum)

Λ	6.764 μm
w_{PPLN}	38.7 μm
q	0.0760 rad/μm
T_{degen}	132.4°C
L	5 mm
f_{eff}	11.190 mm

Table 2.1: Simulation parameters for modelling PPLN photon pair source.

momentum-space, a perpendicular wavevector $\mathbf{q}$. This was fitted to a two-dimensional Gaussian offset by some radius $\mathbf{r}$, presented in Appendix B.2.3. Spatial variances from the x- and y-directions were extracted and averaged to display FWHM in error-bar form, as presented in Fig. 2.4. Additionally, the effect of refraction from the large refractive index lithium niobate to air was calculated for radii via paraxial Gaussian ABCD matrix propagation (described in Appendix B.2.4) before these Cartesian spatial results were converted to momentum-space.

The temperature-dependent radii results showed the transition of a single wavelength (1064 nm) from a noncollinear component wavevector ($\mathbf{q}$) to the collinear, single-Gaussian spatial distribution of macroscopic spectral intensity shown in Fig. 2.2. Additionally, these perpendicular wavevectors $\mathbf{q}$ can be converted to opening half-angles via $\frac{q}{|\mathbf{k}|} = \sin\theta$.

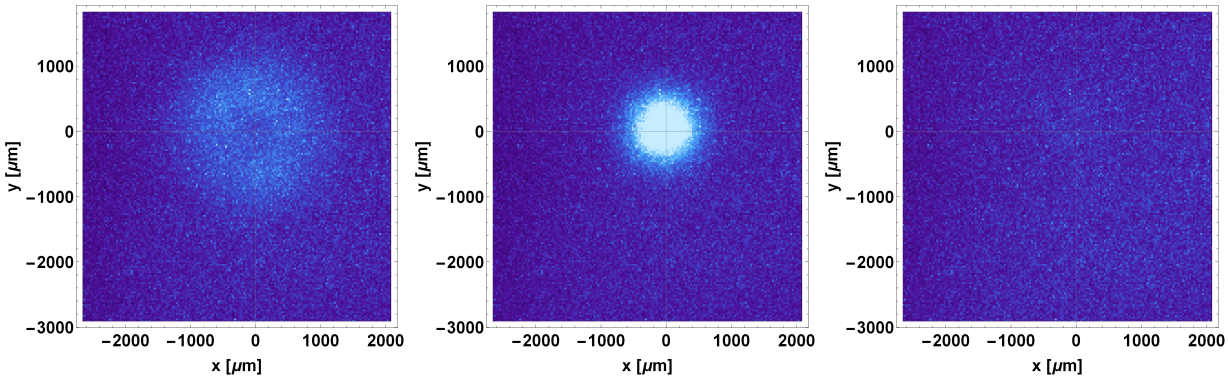

(a) $T = 120.3°\text{C}$ (b) $T = 131.9°\text{C}$ (c) $T = 137.7°\text{C}$

Figure 2.3: Measured SPDC spatial profiles as seen on the beam profiler camera. Noncollinear emission within the 10 nm bandpass filter is only present for temperatures beneath the degenerate collinear temperature of T=132.4°C.

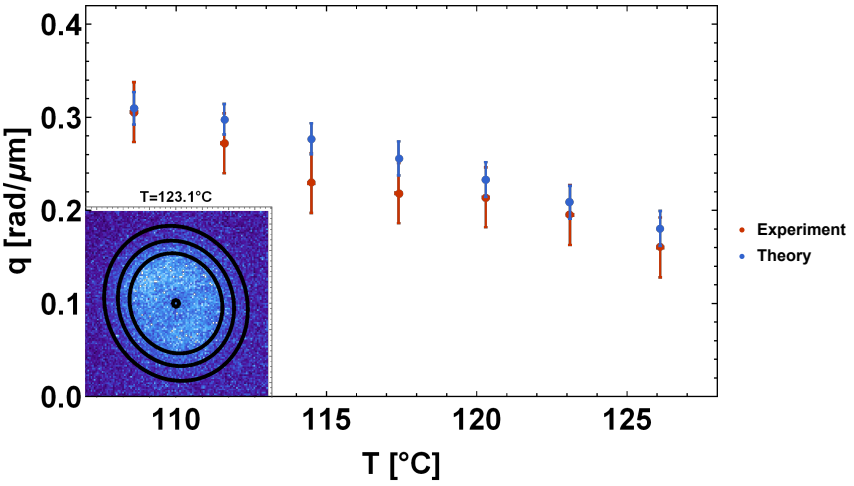

Figure 2.4: Beam profiler spatial data and fit for $T = 123.1°\text{C}$ "cone"

2.3 X-Spectrum: Spatial-Spectral Properties

Combining both the spectral and spatial information of SPDC emission yields a position-dependent spectrum of an unusual structure. This arises out of a joint coherence between space and time [67] due to symmetry enacted under the momentum and conservation laws in phasematching. This has been demonstrated to exist in quadratic $\chi^{(2)}$ nonlinear frequency conversion such as SHG [68] and SPDC [69].

Spatial-spectral representations of this result in a hyperbolic structure commonly described in the literature as "X-spectrum" or "X-wave", as simulated in Fig. 2.5. For reference, the degenerate, collinear SPDC configuration of interest is close to that of Fig. 2.5b. For temperatures greater than $T = 132.4°\text{C}$, the frequencies separate and become non-degenerate with continued collinearity, as depicted in Fig. 2.5c.

The ramification of this property is an unfactorability between space and time [69] which can result in extreme (femtosecond/micrometer) spatiotemporal localization [70]. It is this property we are interested in utilizing and confirming for frequency conversion later on.

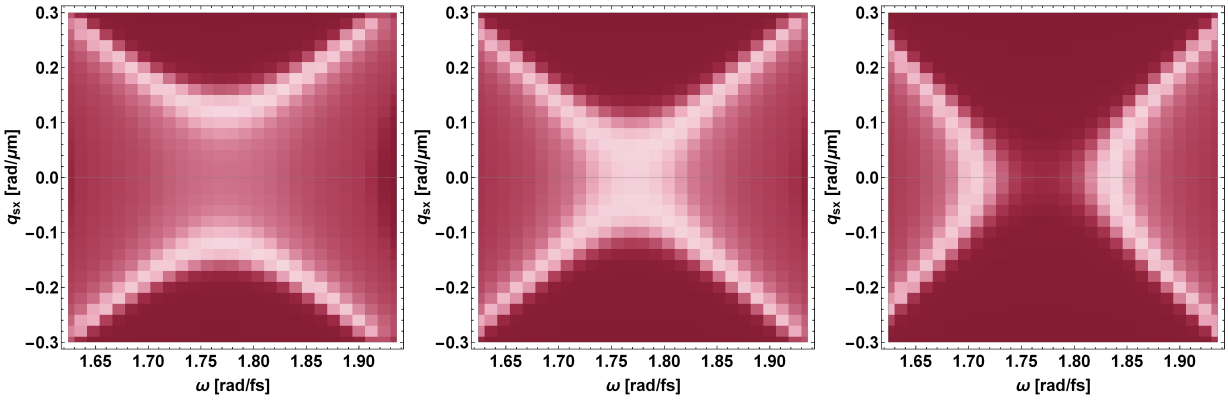

(a) $T = 129.1°\text{C}$ (b) $T = 132.4°\text{C}$ (c) $T = 136.5°\text{C}$

Figure 2.5: Simulated X-spectra of Type-0 SPDC in PPLN for temperatures below and above degenerate temperature.

These X-spectra are dependent on various crystal and pump parameters, as characterized by Lerch et al. [71]. Poling period, Λ, tuning behaves similar to temperature tuning of Fig. 2.5 by shifting around temperatures for degenerate collinear (near $q = 0$) configuration.

2.3.1 "X-blobs": A single-shot measurement method for spatial-spectral characterization

X-spectra is typically acquired by micrometer-level raster-scanning (x,y meandering) of an optical fiber over some down-conversion imaging plane and measuring the spectrum with a fibercoupled

optical spectrum analyzer. This is a time-consuming measurement, especially with low-rate photon pair sources or inefficient detection.

Given the measurements described in Section 2.2.2, I formulated the following simple method for extracting spatial-spectral X-spectrum information. From these SPDC "cone" images of Fig. 2.4, perpendicular wavevector parameters can be extracted and combined with spectral filter parameters to yield spatial-spectral "X-blobs". These Gaussian approximations of X-spectra for a given wavelength band are made possible by using a spatially discriminating detector (CCD camera) and spectral filters. This advantageously allows for spatial-spectral information to be extracted at each crystal temperature from single-shot measurements.

The mean radius values (converted to perpendicular wavevector, q_0) and extracted variance (σ_q) results of the spatial "cone" Gaussian of Appendix B.2.3 (as displayed in Fig. 2.4) can be combined with the spectral bandpass filter information (ω_0, σ_ω) into a two-dimensional Gaussian. These "X-blobs" are defined in Eq. (2.8).

$$F_{\text{xblob}}(\omega, q) = \text{bkg} + \mathcal{N} \exp\left[-\frac{1}{2(1-\rho^2)}\left(\frac{(\omega-\omega_0)^2}{2\sigma_\omega} + \frac{(|q|-q_0)^2}{2\sigma_q} - \frac{2\rho(\omega-\omega_0)(|q|-q_0)}{2\sigma_\omega\sigma_q}\right)\right] \tag{2.8}$$

Accurate conversion from Cartesian coordinates to wavevector is achieved via ABCD matrix Gaussian beam propagation, as discussed in Appendix B.2.4.

This, of course, is not a full X-spectrum measurement as its spectral information is artificially bound by transmission of the bandpass filter. However, since most down-conversion sources are designed for use at a single, particular wavelength, the use of an appropriate bandpass filter in this method will provide all the useful spatial information.

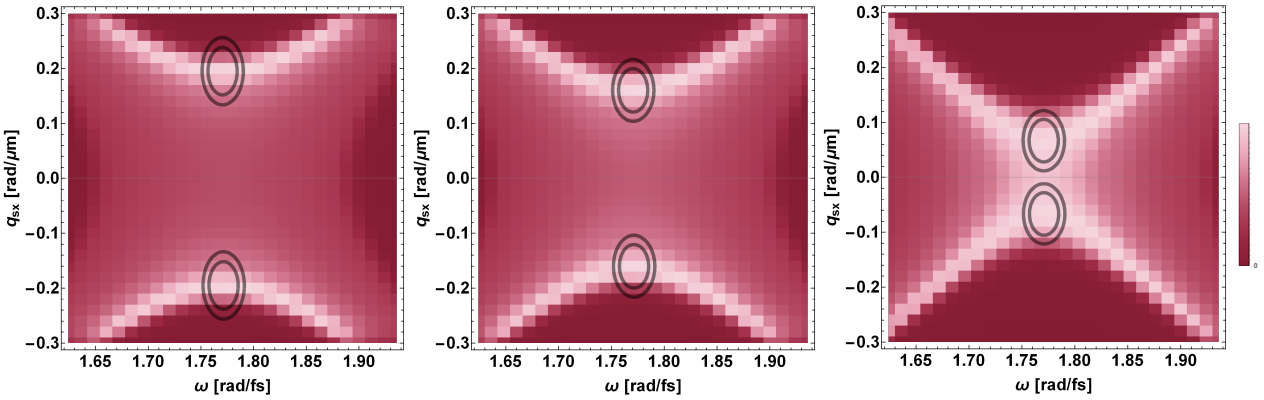

(a) $T = 123.1°\text{C}$ (b) $T = 126.1°\text{C}$ (c) $T = 131.9°\text{C}$

Figure 2.6: Density plots=theory, contours=experiment for lens f=175 mm

The extracted X-blobs and simulated X-spectra for various temperatures beneath degenerate configuration show good agreement, as seen in Fig. 2.6.

2.3.2 Discussion

When any new entangled photon source is built, its spectral properties, among others, are characterized. Most often with SPDC sources, the multimode spatial properties are disregarded when projected onto a single-mode optical fiber for more convenient quantum optical manipulation [30]. This is all well and good until mixed spectral components reduce necessary photon state purity or Hong-Ou-Mandel interference visibilities [72]. In the literature this has been addressed by Guerreiro et al. [73] among others for strategic optical design to limit the collection of unwanted frequencies without resorting to spectral filtering which lowers count rates. What this X-blob method offers is simple, quick technique for measuring the spatial distribution for the wavelength of interest.

The limitations of this method stem from the competing factors of the precision or variances of these X-blobs. First, in the frequency dimension, the bandpass filter widths dictate σ_ω regardless of spatial distribution. Similarly, the bandpass filter affects the amount of counts incident on the camera which, dependent of camera noise properties, affects the signal-to-noise ratios of the measurement. Additionally, this method can only measure noncollinear phasematching of the wavelength(s) of interest. For this particular example, this resulted in X-blobs beneath degenerate collinear phasematching temperature where frequency conversion is weak (see Fig. 2.2 for relative temperature-dependent intensities). Thus, due to noise, no accurate pump waist-dependent variance could be extracted. However, depending on the camera detection efficiency or SPDC photon pair flux, this may be possible [74], thus providing estimates of spatial-spectral entanglement [75].

To conclude, in this chapter I characterized and simulated the spatial and spectral properties of Type-0 SPDC generated from bulk PPLN. This showed good agreement and appropriate suitability for a biphoton up-conversion experiment in comparison to the literature. Additionally, I proposed and demonstrated a new, simple method for characterizing the coupled spatial-spectral properties of SPDC through an relevant estimate of the X-spectrum.

Chapter 3

White Light Interferometry for Dispersion Characterization

Biphoton quantum frequency conversion requires dispersion cancellation for the femtosecond-resolution photons to efficiently meet and convert in a nonlinear medium. Here, I present a characterization of a necessary building block for quantum frequency conversion, namely dispersion manipulation via a low loss prism compressor. This tool is characterized using white light interferometry from a wavelength-scanning laser. The methodology is based closely off of the well-established field of optical coherence tomography (OCT) and the concepts of interferometry introduced in Section 1.5.

3.1 Inspiration: Spectral Interferometry By Way of Optical Coherence Tomography

There is a large established body of research on optical coherence tomography who study the internal structure of samples such as living eyes or other objects [42, 76, 77], with many different types of interferometers. Reflections off of different structures in the sample can be extracted from the interference fringes then Fourier-transformed to relevant spatial units. The interferometer stability and quality of fringe data to accurately extract the spectral phase is similar in this present application to that for OCT prior to the extraction of the desired point spread function [78]. In order for spatial structures of samples to be most precisely extracted from interference fringes, group delay dispersion and other orders of phase must be compensated [79]. This can either be achieved via data post-processing [80] or by precisely compensating dispersion with glass in the reference arm of the interferometer (babinet prism) [81].

There are several methods in the OCT literature to extract the spectral phase. Due to the availability of a high speed swept-source laser at the central wavelength and bandwidth of

interest, I chose to design a white-light interferometer similar to those used in swept-source OCT [77, 80, 81].

The experimental technique demonstrated here may be useful for interferometry with high-speed swept lasers, but the data analysis can be extended to any sort of spectral domain interferometry. In addition, the technical data manipulation for phase retrieval from a real signal is useful for a large variety of applications which require data transformations such as a Fourier transform.

3.2 Dispersion Characterization Experiment

3.2.1 Swept-source laser

High-speed swept-source lasers are typically made from broadband semiconductor optical amplifiers illuminating a quickly rotating hexagonal grating, allowing for a rapid sweeping of narrow spectral line from short to long wavelength to be coupled into optical fiber [82, 83]. This frequency sweep is inherently fairly linear in time(up to 99%) [84], however calibration of this frequency sweep is often needed for precise phase or reflectometry extraction, as will be discussed in Section 3.2.3.

The swept-source laser used in this work is the Santec HSL-1000 which is centered at 1064 nm and continuously swept 74 nm over 21 μs at 28 kHz sweep rate. Similar to other OCT experiments using this laser [81], the sweep signal is triggered off of a portion of a bandpass-filtered beam.

3.2.2 Swept-source white light interferometer

Since this is a frequency-sweeping interferometer, the displacements of the reference and the sample arms remain constant over the recording of the interference fringe. Because of this, no parallel calibration of path difference was required [81, 85]. Interference fringes were taken at five different reference arm displacements demonstrating reliability in the spectral phase extraction method.

High interference stability is needed for accurate extraction of the spectral phase. As such, the visibility of the fringe is maximized by optimizing the polarization with a half-wave plate prior to entering the interferometer. This is also important in OCT applications as polarization and chromatic aberrations from dispersion affect the longitudinal resolution within the sample [81].

Similar to other OCT and white light interferometry experiments, a balanced detection scheme was employed to increase the photodiode sensitivity and to reduce power fluctuations [81, 86]. Additionally, subtraction between each interferometer output allows for the constant intensity background terms $\langle \tilde{\mathcal{E}}_1^2(t-\tau)\rangle$ and $\langle \tilde{\mathcal{E}}_2^2(t)\rangle$ from Eq. (1.43) to be removed.

To allow for live manipulation and control of interferometer fringe data, I designed a LabVIEW program. This controlled and saved each photodiode electrical signal from the oscilloscope to apply background subtraction and normalization by $\frac{D1-D2}{D1+D2}$ in addition to individual detector DC voltage offset adjustments. In addition, the LabVIEW program displayed the real-time magnitude of Fourier-transformed normalized fringe signal for more accurate path length displacements.

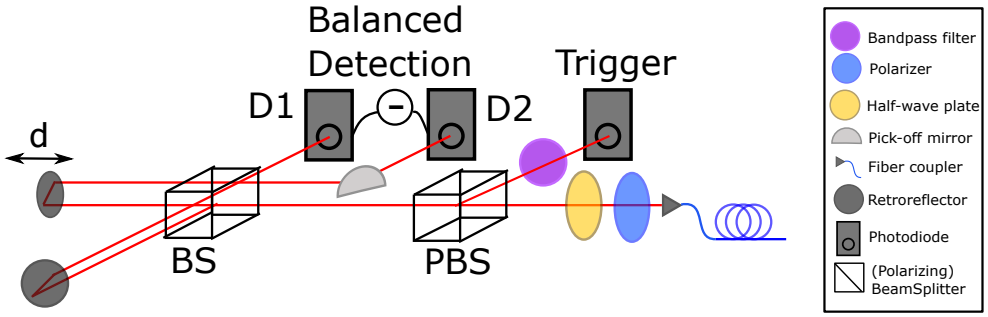

Figure 3.1: Reference swept-source white light interferometer for sweep linearization in an offset Michelson configuration.

3.2.3 Data processing: Sweep manipulation

As is the case with other Fourier domain interferometry experiments, special care needs to be taken to make sure that the wavelength sweep is linear in time, or that it is being sampled equally in time [87].

Many experimental and computational techniques have been developed to linearize the frequency sampling, for either swept-source or spectral domain interferometry. For example, Ahn and Kim [88] built an empty auxiliary interferometer and determined the swept-laser's instantaneous frequency from its extracted spectral phase and used this to resample the signal. Other techniques include implementation of an auxiliary Fabry-Perot cavity to give a tight frequency-time reference [89]. In addition, fringe counting of the signal from an additional unbalanced interferometer can be used [90].

Contrary to other spectral-domain OCT (SD-OCT) implementations, my application of white light interferometry for a single device characterization has no need for fast calibration and computation rates, which is a serious motivator of different calibration and rescaling methods in the literature. Here, a variant of linearizing with an instantaneous frequency was employed. From an empty, unbalanced interferometer signal, the phase, $\phi(t)$ was obtained via the argument of a Hilbert-transformed complex analytic interference fringe signal (see Section 3.3.2). Since $\phi(t) = k(\omega(t))(d) = \omega(t)\tau = \omega(t)\frac{c}{d}$, the abscissa, or x-axis, can be replaced with an extracted time-dependent angular frequency

$$\omega(t) = \phi(t)\frac{c}{d}. \tag{3.1}$$

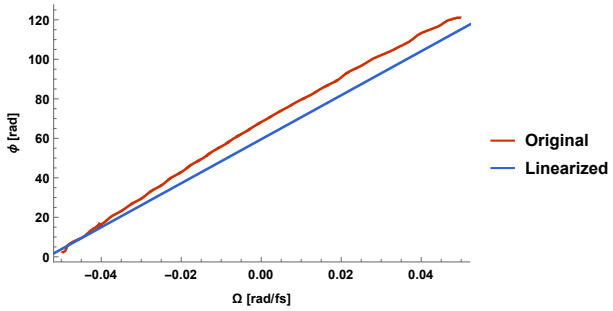

Figure 3.2: Comparison of measured phase extracted from linearized vs unlinearized $\omega(t)$ as taken in the experimental setup of Fig. 3.1.

A downside to this technique is that the frequency instabilities of individual wavelength sweeps are not observed. However, the results of this linearization are within experimental error. Moreover, this application of swept-wavelength interferometry does not require the same level of phase stability as no Fourier transform nor multidimensional scans (image generation from B-scan[1]) are needed.

In addition to linearization, other sweep manipulations in post-processing are needed, such as transforming wavelength ($\lambda(t)$) to angular frequency ($\omega(t)$) to shifted frequency ($\Omega(t)$). The rescaled interference fringe then is processed in *Mathematica* with a Wiener filter [91, 92] to reduce the Gaussian noise on the signal prior applying mathematical transforms. It has also been shown [82] that this additional data smoothing processing step can increase the resolution of OCT and phase reconstruction accuracy [85].

Since this linearization method is based on physical mirror displacements, the uncertainty resulting from different mirror displacements between the characterization sweep and the sample sweep were investigated. It was hypothesized that this uncertainty should be small, as this is a first-order, non-frequency-dependent shift. To test this, I generated theoretical dispersed fringes of {Air,+glass} with the frequency abscissa generated from imperfect theoretical interference fringes offset by the maximum positional time-delay micrometer offset. This yielded a 4 fs^2 uncertainty, discussed in Appendix A.4.

3.3 Spectral Phase Extraction

Using white light interferometers, extraction of the spectral phase can be useful for measuring the group velocity dispersion of samples, such as water [93] or the sample's index of refraction [94].

[1] *A-scan* is defined in OCT as a one-dimensional depth scan. A common benchmark often cited in the literature is a *B-scan* rate, or a two-dimensional image rate for OCT systems [83]

To validate the characterization results, two methods were taken to extract the spectral phase from the resulting interferometer fringes. First method is derived from [80] and is a variant of extracting the phase via $\phi = \arctan\left(\frac{\text{Re[signal]}}{\text{Im[signal]}}\right)$. The second method is based on another conceptually simple idea of fringe counting. If every time a fringe goes through zero, a π phase shift occurs, then spectral fringes should yield a spectrally-dependent zero spacing or chirp over the spectral fringe. Thus, by recording the frequency of a phase zero crossing, the spectral phase, $\phi = n\pi$ where n is an integer, can be extracted.

These two methods were used to verify the group delay dispersion imparted by an experimental implementation of a prism compressor.

3.3.1 Fringe counting

Following from the interferometry background of Section 1.5.1, the spectral phase imparted onto the electric field from the sample is of the form:

$$\tilde{E}_2(\Omega) \approx T(\Omega)\tilde{E}_1(\Omega)\exp\left[-id\left(k_l + k_l'\Omega + \frac{k_l''}{2}\Omega^2 + \frac{k_l'''}{6}\Omega^3 + \dots\right) + id\left(\frac{\Omega+\omega_l}{c}\right)\right]. \tag{3.2}$$

The GVD coefficient, k_l'', can be determined from a polynomial fit of this frequency-dependent phase, extracted via fringe zero-crossings. Then, from multiplication of known sample thickness, d, the GDD can be calculated.

This fringe counting method can be visually demonstrated in Fig. 3.3 from interference fringes modified by 24 cm of NFK51A glass (GDD=8100 fs^2). The phase is extracted from counting zero-crossings of the spectral fringes by a *Mathematica* function[2] and multiplying by a factor of π.

3.3.2 Hilbert method

Hilbert transform is seen as a more useful tool in OCT for determining dispersion in a sample over that of the Fourier transform as the multiple reflections resulting in a complicated phase dependence in addition to chromatic dispersion [80].

As previously alluded to, the Hilbert transform (discussed in more detail in Appendix A.1) takes a real-valued signal and generates the imaginary part of a complex analytic signal. With this now complex analytic signal, the phase can be extracted from a general time-dependent signal via

$$\phi(t) = \arctan\left(y(t)/\mathrm{H}\{y(t)\}\right), \tag{3.3}$$

[2]Zero-crossing *Mathematica* function modified from http://mathematica.stackexchange.com/questions/10640/find-zero-crossing-in-a-list modified and reproduced in Appendix B.1

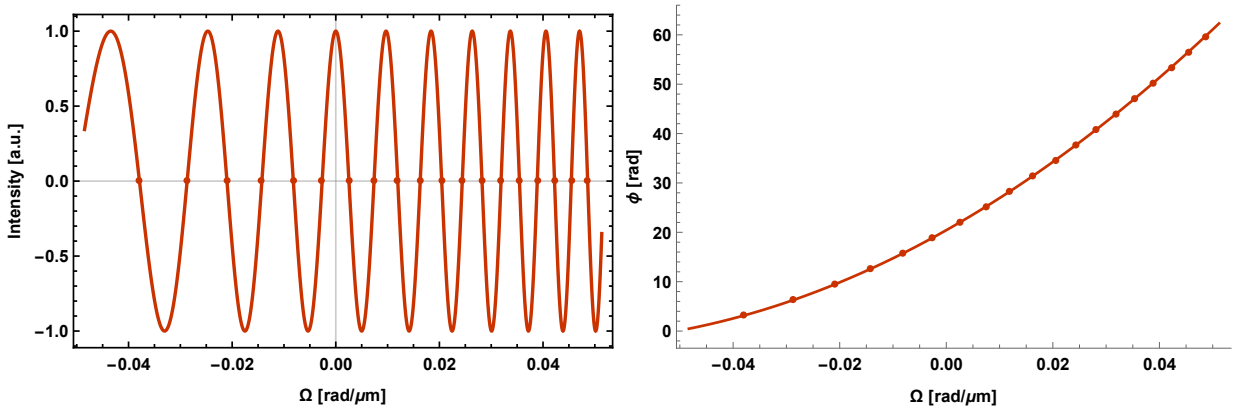

(a) Theoretical fringes

(b) Phase from zero-crossings

Figure 3.3: Fringe counting method demonstrated by an interferometer with 24 cm of NFK51A glass over the relevant spectral bandwidth.

As is the case here, the time-series data obtained from the oscilloscope is mapped to shifted frequency to obtain $\phi(\Omega)$. Similar to the previous method, a third-order polynomial can be fit to the unwrapped spectral phase and the GDD can be related directly from fitting coefficient, b.

$$\phi(\Omega) = \phi_0 + a\Omega + \frac{1}{2}b\Omega^2 + \frac{1}{6}c\Omega^3 \tag{3.4}$$

3.4 Interferometric Characterization of a Prism Compressor

The prism compressor, as discussed in Section 1.4.3, is an integral tool in ultrafast optics for tuning the chirp, or related GDD, of ultrashort pulses. Characterization of such a prism compressor in the experimental setup was a priority for the ultimate goal of photon pair quantum frequency conversion where low-loss dispersion compensation is necessary. Beyond verifying the accuracy of theoretical prism compressor equations [18], practically measuring both zero and calculated dispersion of up-conversion of down-conversion setup were of interest.

Characterizing prism compressors within white light interferometers is not unheard of. Naganuma et al. [85] demonstrated white light interferometry characterization of a prism pair within a laser cavity. Here, using an interesting combination of swept-source white light interferometry and two spectral phase extraction techniques, I present the results of a series of interferometer measurements. Such results verify the dispersion imparted by a doubly-folded prism compressor set for three different positions with two additional known sample comparisons, inspired by [81]. Additionally, two phase extraction methods – the Hilbert transform method and the fringe counting method – are implemented on experimental and theoretical data, as previous discussed with extracted spectral phase results within experimental error

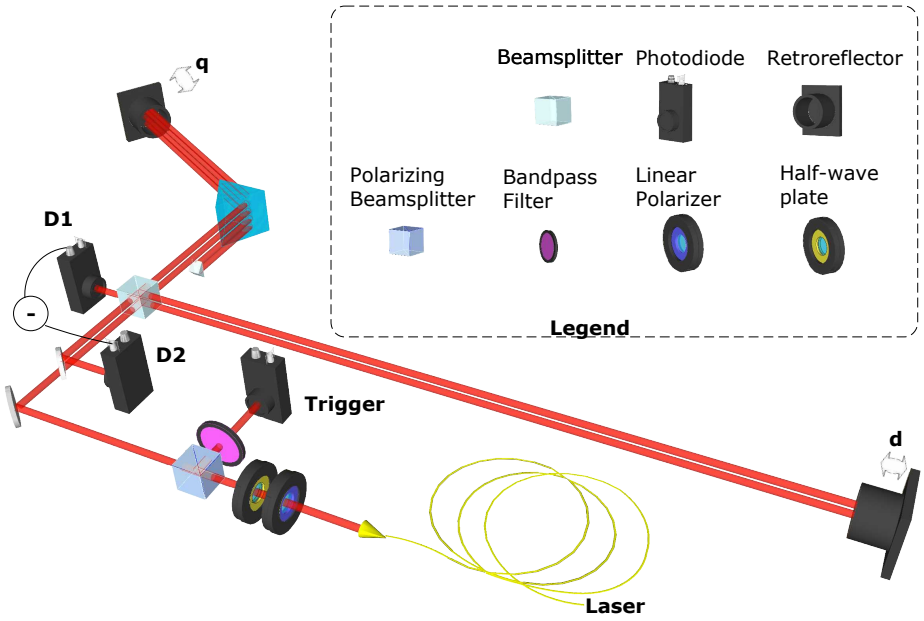

Figure 3.4: Michelson interferometer built around existing prism compressor for phase extraction. Glass sample placed in either interferometer arm according data set of interest. Balanced detection is obtained from subtraction between detectors D1 and D2. Depending on the data set at hand, the glass block was placed in either the prism compressor or empty interferometer arm.

3.4.1 Measurement test design: data sets

Verifying prism compressor's accuracy when set to the calculated biphoton up-conversion setup dispersion was of prime interest. Since it was not possible to include the entire biphoton portion of the setup in the interferometer due to focusing difficulty of crystal to crystal, the net Mach-Zehnder interferometer phase measured was that of one arm: prism compressor, set to the calculated negative "setup" dispersion (designated {Air,-setup} in contracted experiment notation defined in Fig. 3.5).

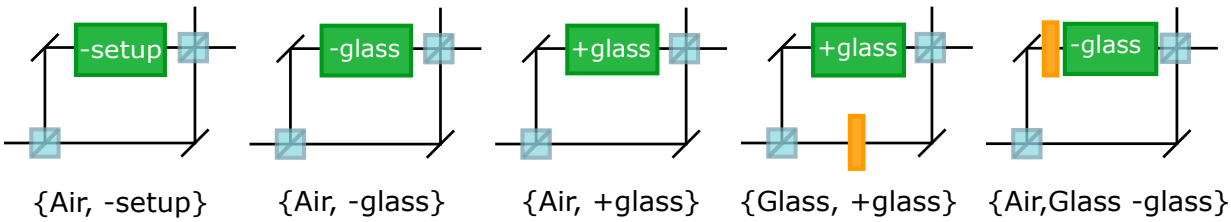

Figure 3.5: Prism compressor characterization dispersion scenarios and data set notation. Here the green blocks refer to the prism compressor and it's dispersion setting whereas the orange block is the BK7 block of glass.

Since prism compressors can produce positive GDD in addition to negative GDD, it was desirable to find that zero dispersion point. Given the availability of a 0.961 cm BK7 glass block[3], two other prism compressor positions were chosen to equal positive and negative GDD values of this glass. The dispersion from these prism compressor positions were also measured alone, as seen in Fig. 3.5.

Under the premise that equal phase in both arms of an interferometer will cancel, two interferometer configurations of "zero dispersion" were measured for prism compressor settings of "+glass" and "-glass". For each of these five interferometer dispersion configurations (Fig. 3.5),

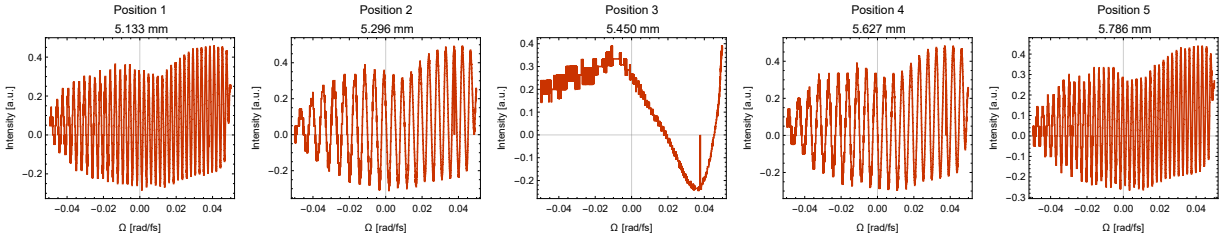

Figure 3.6: Example interference fringes from "{Air,+glass}" prism compressor dispersion and interferometer setting with five different displacements.

five interferometer displacements were chosen, qualitatively described as "lots of fringes" and "some fringes", on both sides of zero path difference (single fringe). The shorthand for dispersion in each interferometer arm making up these characterization scenarios are depicted in Fig. 3.5. For consistency's sake, the relative interferometer arm displacement was set relative to the same Fourier transform frequency displayed live on the LabVIEW program. Using this method, it was found that position uncertainty of all measurements was within 9 μm. An example data set, normalized to total power from both interferometer outputs, is seen in Fig. 3.6.

Using the two phase extraction procedures described in Section 3.3, the quadratic fitting coefficients of Eq. (3.4) were extracted for each interferometer displacement position at each dispersion scenario. Example fitting results are located in Appendix. A.3.

For the sweep linearization, interference fringes from an empty, "dispersion sample-free" interferometer are needed. Since the quadruple-pass prism compressor of test displaces beam height, it was not possible to simply "remove" the prism compressor to measure the empty interferometer. Because of this, a second empty interferometer was built for fringe measurement at the five relative displacements, as seen in Fig. 3.1. The phase extracted from these empty fringes were used to generate a linearized abscissae for subsequent measurements, as per the method described in Section 3.2.3.

[3]I would like to thank Dr. Kevin Resch for allowing me to near-indefinitely borrow this optical component.

3.4.2 Prism compressor characterization results

For each interferometer net dispersion scenario, the phase of mirror Positions 1, 2, 4, and 5 were extracted. For the Hilbert transform method, this reduced the phase variations/uncertainty from the zero-path delay single fringe of Position 3, as noted in the literature. This also allowed for more direct comparison with the fringe counting method, which required multiple fringes or zero-crossings to extract the spectral phase. Fitting results for {Air, -setup} are shown in Table A.1. It is interesting to note that the sign change is conserved moving across zero-path delay. Recall that the quadratic fitting coefficient, b, is related to GDD by $b = -\frac{k_i'' d}{2} = -\frac{\text{GDD}}{2}$.

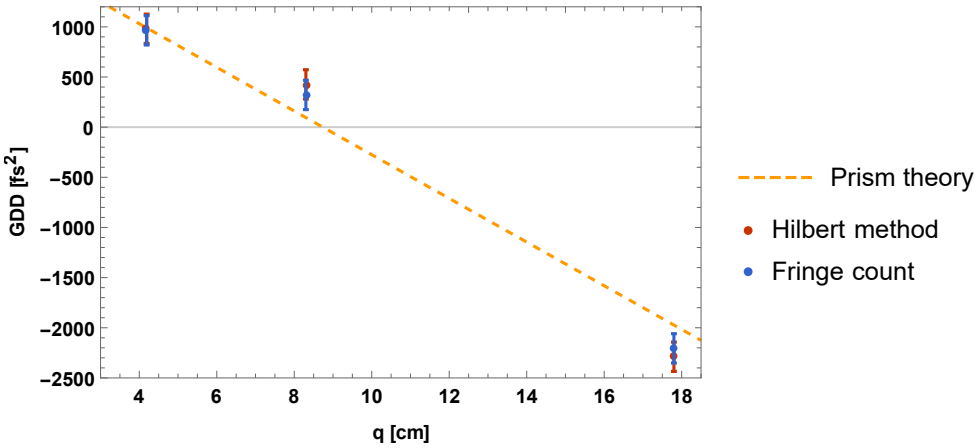

Figure 3.7: GDD measurements from prism compressor via WLI.

The dispersion of the prism compressor for different dispersion scenarios were adjusted via the prism-retroflector distance, q, which is related to the interprism length, L. Upon further inspection, the prism insertion, h, was not in the position assumed in calculating appropriate q values for test within the interferometer. This resulted in a constant GDD offset of -526 fs^2.

The extracted interferometric GDD results from the prism compressor, shown in Table A.2, can be viewed in two ways. First, by the stand-alone, q-dependent prism compressor-imparted dispersion results, as seen in Fig. 3.7. Second, to validate measurements with a known glass sample, the prism compressor is set to compensate by the same amount, as seen in Fig. 3.8.

3.4.3 Discussion

In this chapter, I presented the characterization of a doubly-folded prism compressor using white light interferometry. The techniques utilized here were inspired by the field of optical coherence tomography, and specifically, swept-source optical coherence tomography. Based on this, I developed a white light interferometer using a frequency-swept laser and extracted the spectral phase of three different prism compressor GDD positions via two methods: Hilbert transform and fringe counting. By characterizing and correcting systematic errors such as the laser sweep

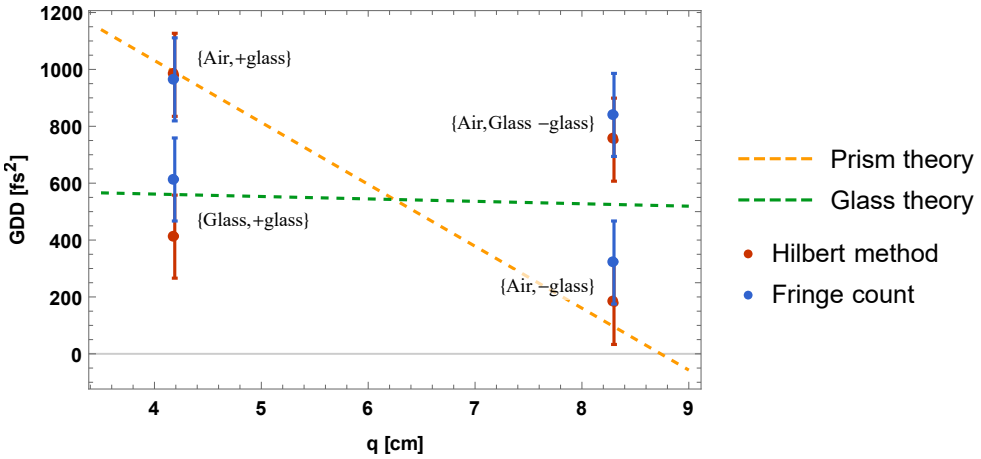

Figure 3.8: Mach-Zehnder interferometer dispersion measurements with "cancellation" from a 0.961 cm BK7 block as a function of prism-retroreflector distance, q.

linearity and the prism insertion, final results yield GDD tunability from simulated values of +560 fs^2 to -1973 fs^2 with separate experimental phase extraction method results nearly within experimental uncertainty of these results. From just the values measured here, the dispersion cancellation requirements for the proposed biphoton up-conversion experiment can be fulfilled by this ultrafast optical device. Additionally, the data processing and experimental techniques were validated by successful interferometer "cancellation" of prism compressor dispersion by a known sample of BK7 glass.

An advantage for this technique over others from the availability of a light source with the correct central wavelength and bandwidth for the intended quantum light source use. Many other characterization techniques exist for characterizing prism compressors, such as autocorrelators or, as in the case of the identically designed doubly folded prism compressor of [48], an implementation of frequency-resolved optical gating. It is additionally possible for spectral fringe and phase extraction from such a light source on a spectrometer, similar to spectral-domain OCT. This option was somewhat limited by availability of an appropriate spectrometer. The 1060 nm range is often problematic for detector sensitivity as it falls near the detection efficiency edges of both Si-based and InGaAs-based spectrometers. This spectral domain-based method would have also required a critical pixel-to-frequency calibration for accuracy.

Finally, white light interferometry and the techniques discussed here offer tantalizing experiment opportunities for translation from classical to quantum. Crossover works such as [4–6, 95] among many others have demonstrated interesting quantum optical white light interferometry. Given the mostly non-interacting nature of the quantum optics subdiscipline with the optical coherence tomography subdiscipline, this work presents some of the key concepts and important data extraction techniques of OCT for the quantum optics reader.

Chapter 4

Dispersed Time-of-Flight Characterization of a Telecom Photon Pair Source

Chromatic dispersion has been the main antagonist against the quest for quantum frequency conversion of SPDC photon pairs presented thus far in this thesis. However, for applications outside of this goal, dispersion can be a useful tool for the study and characterization of SPDC photon pairs. This chapter discusses collaborative work I participated in toward the theoretical and experimental characterization of a similar PPLN-based photon pair source at the telecom wavelength band where dispersion played a pivotal role in the method.

Entangled photon pairs suited for telecommunications [50, 71, 96, 97] infrastructure around 1550 nm provide an interesting test bed for quantum communication and quantum information protocols [54]. While telecom single-photon level detection tools have had poor sensitivity until recently, the development of spectrally broadband, high detection efficiency superconducting nanowire single-photon detectors (SSPDs or SNSPDs) [98] has made new methods of entangled photon sources characterization possible.

By utilizing chromatic dispersion from long, low loss Corning SMF28e+ single-mode optical fibers, introduced in Section 1.4.3, the SPDC phasematching tuning curves of Type-0 PPLN can be extracted from time-of-flight measurements between each photon of the pair.

Fiber spectrometers have previously been used to measure various spectral properties of photons pairs [50, 99–101]. Here I present a method for extracting the spectral phasematching tuning curves of entangled photon pairs generated from the process of Type-0 SPDC based on time-resolved measurements in a telecom fiber spectrometer.

4.1 Characterizing a Telecom Photon Pair Source

The photon pair source of interest is a 10 mm bulk PPLN crystal phasematched for Type-0 down-conversion at a given crystal temperature T, as seen in Fig. 4.1. The 780.2 nm cw pump laser is removed from the photon pairs by means of a dichroic mirror and two longpass filters and the photon pairs are split into two paths for spectral analysis. Since these photon pairs are both of

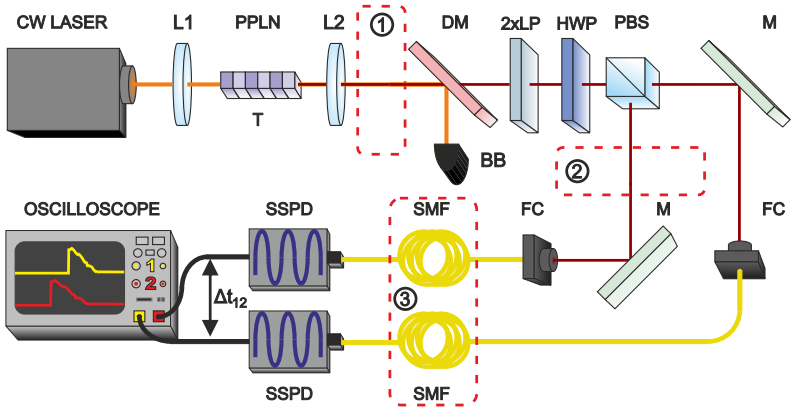

Figure 4.1: Setup used in the experiment. HWP: half-wave plate, T: temperature controller, L: lens (L1- F=125.0 mm, L2- F=75.0 mm), BB: beam blocker, DM: dichroic mirror, LP: longpass filter, PBS: polarization beam splitter, M: mirror, FC: fiber couple (F=8.0 mm, A240TM-C), SMF: single-mode fiber, SNSPD: superconducting nanowire single-photon detector.

the same polarization, a half-wave plate set to 22.5° rotates the polarization as to split the signal and idler photons equally on a polarizing beamsplitter. Photons from each of the separate paths are coupled to single-mode optical fiber and, after propagating through varying lengths of fiber, are each detected by SSPDs. The resulting electrical signals are analyzed on a fast oscilloscope to extract time delays between the two paths which are dependent on the signal and idler photon group delays through the fibers.

4.2 Dispersion Characterizations of Optical Fibers

As discussed in Section 1.4.3, long optical fibers can be used as a fiber spectrometer. This is an especially advantageous measurement technique in the telecom spectral range as absorption losses are quite low allowing for still appreciable photon transmission and detection in long optical fibers.

The chromatic dispersion in a single-mode optical fiber, as discussed in Section 1.4.2, is a temperature-dependent combination of frequency-dependent material dispersion and frequency- and waveguide-dependent waveguide dispersion [41]. This can be simulated given the appropriate silica Sellmeier equation and fiber parameters. However, due to the long lengths of optical

fiber needed to perform the time → frequency Fourier transform, the existence of temperature fluctuations, material inhomogeneities, and other systematic experimental uncertainties can affect the accuracy of such spectral measurements.

4.2.1 OPO measurements

Previous works [100, 101] from our group have calibrated the fiber spectrometer with a known light source at one or two frequencies. In this work, due to availability of a tuneable OPO pulsed light source, group delays were measured over the range of 1310 nm to 1660 nm, the entire spectral range of the idler photon.

In order to accurately calibrate the long optical fiber of the fiber spectrometer, 16 wavelengths from an OPO were used to obtain wavelength-dependent group delay information. These pulses, ranging between 1310 nm and 1660 nm in approximate 20 nm increments, were coupled into optical fiber and split using a polarizing fiber beamsplitter with one portion going to a triggering fast photodiode, and the other pulse portion to a long fiber sample with a second fast photodiode. Care was taken to equalize OPO pulse optical power to keep nonlinear Raman broadening to a minimum and also to maintain uniform, precise electrical signal measurements.

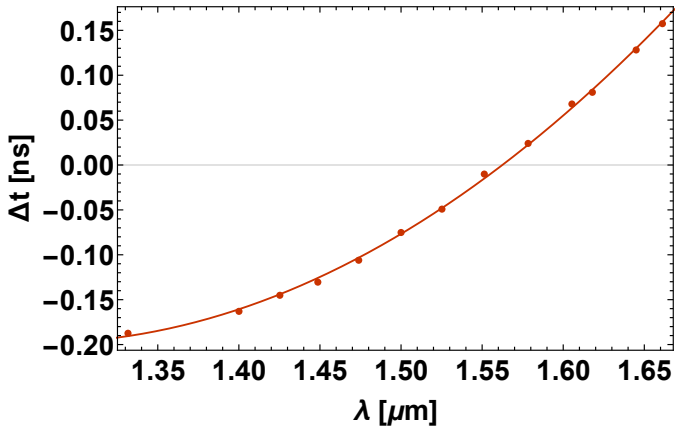

Figure 4.2: Measured and interpolated OPO relative time delay over a 80 m single-mode optical fiber.

Using a fast oscilloscope[1], histograms were constructed from the time delay information between the long fiber sample and the triggering arm for each wavelength. By analyzing the mean value of the timing delay histogram for different OPO wavelengths, the relative group delay could be extracted, as seen in Fig. 4.2. These measurements resulted in a list of OPO wavelengths and associated time delays (measured modulo the subsequent OPO pulse delay). This relative time delay exhibits a near quadratic behaviour in the telecom wavelength band resulting

[1]I would like to thank Dr. Vadim Makarov for lending me this beautiful, 20 GHz bandwidth, 80 GS/s oscilloscope and fast photodiodes.

from the interplay of material resonances in the UV and IR [41]. The fiber spectrometer calibration was completed by fifth-order interpolation over these results. These fiber properties, used in conjunction to the experiment calibration of the next section, allow for the unknown SPDC phasematching tuning curves could then be accurately determined from single-photon time-delay information.

4.2.2 Calibrating experimental time delays

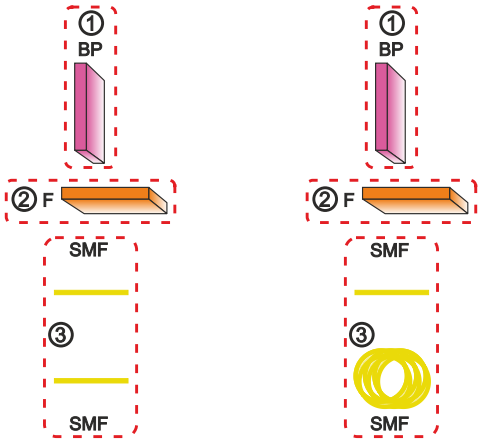

(a) Configuration # 1 (b) Configuration #2

Figure 4.3: Optical element configurations inserted into the dotted boxes of Fig 4.1 to determine zero delay for a given single-photon wavelength. BP: bandpass filter, SMF: single-mode fiber, F: longpass filter.

With frequency-dependent time delays obtained for both 80 m spectrometer fibers, we then sought to reconcile the fiber characterization results with that of the photon pair experiment. If the 80 m spectrometer fiber was the only length used in the experiment, the wavelengths from frequency-dependent delays would be easy to extract. However optical fiber is used in multiple areas of the experimental setup for light transportation, including down into the cryogenic superconducting nanowire single-photon detectors (SSPDs). These additional lengths need to be taken into account for their role in stretching the pulses.

The following scheme was devised by my collaborators to determine the true "zero delay" of the photon pair experiment so only the dispersion from only the spectrometer fibers could contribute to the resulting spectral measurements. This method was based on the effective simultaneity of SPDC photon pair generation time to determine the systematic time delay between signal and idler. The SPDC generated from 66.9°C crystal phasematching is limited by a 1560 nm bandpass filter (10.75 nm FWHM) then equally split via a halfwave plate-polarizing beamsplitter combination, as described in the previous section. One of the paths is additionally filtered by

a 1500 nm longpass spectral filter. This filter configuration remains constant throughout the time delay calibration tests. This scheme is depicted in Fig. 4.3. First, time delays are recorded on a fast oscilloscope for two short single-mode optical fiber patch cables. This configuration should provide the least (though still noticeable) pulse spreading between the degenerate photons. Finally, a combination of the long 80 m spectrometer and short fiber is performed: time delays between a short and long fiber are measured.

These time delay results are subtracted from the variable phasematching temperature photon pair results to obtain a full system "short" time delay Δt_{short} (Eq. (4.1)) and "long" time delay Δt_{long} (Eq. (4.2))

$$\Delta t_{\text{short}} = t_{sh,T} - t_{cal,sh} \tag{4.1}$$

$$\Delta t_{\text{long}} = t_{l,T} - t_{cal,l}. \tag{4.2}$$

These are then combined to form the final time delay, Δt of Eq. (4.3) which is comparable to the interpolated OPO fiber measurements.

$$\Delta t = \Delta t_{sh,T} - \Delta t_{l,T} \tag{4.3}$$

Using this new Δt, derived from the 1560 nm calibration reference, the wavelength of the photons from a different crystal temperatures can attainted from the OPO time-delay interpolation of Fig. 4.2.

4.3 Photon Source Characterization Results

After each photon is detected on cryogenic SSPDs, the electrical signals are analyzed into histograms on a fast oscilloscope. This yielding traces visibly similar to those taken on an optical spectrum analyzer. However, the time-delay-to-wavelength conversion requires careful fiber dispersion analysis.

The central wavelengths can be extracted directly for time delays within the OPO fiber calibration. This corresponds to the lower wavelength photon of the pair. Utilizing the energy conservation condition, the central wavelength of other photon from the pair can determined. The resulting central wavelengths are plotted (dots) in Fig. 4.4a.

The photon spectral bandwidths can additionally be extracted from the central wavelength measurement interpolation by use of Eq. (4.5)

$$\Delta t = \frac{d}{d\lambda} t(\lambda) \Delta\lambda \tag{4.4}$$

which, when rearranged, yields

$$\Delta\lambda = \frac{\Delta t}{\frac{d}{d\lambda} t(\lambda)} \tag{4.5}$$

The experimentally extracted photon bandwidths are shown (red) in Fig. 4.4b.

4.3.1 Modelling a telecom SPDC source in PPLN

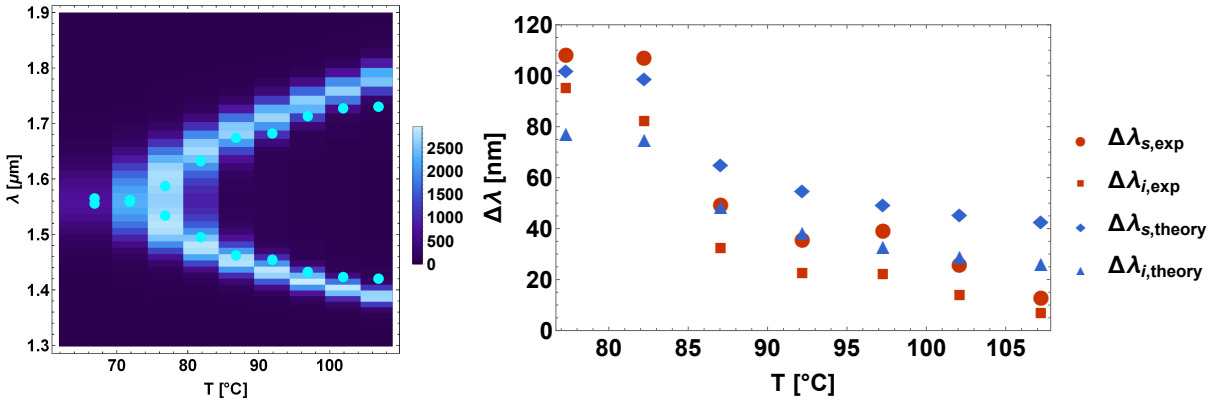

(a) Central wavelengths

(b) Spectral bandwidths

Figure 4.4: Simulated PPLN tuning curves (density plot) with fiber spectrometer central wavelength results (points).

Using the experiment-to-simulation matching procedure mentioned in Appendix B.2.2, I chose a poling period, Λ, based on the solution to $\Delta k = 0$ of Eq. (2.2). Given the perpendicular wavevector ($\mathbf{q}$) determined from the beam waist in the PPLN crystal and the degeneracy temperature of the tuning curve, the simulation parameters of Table 4.1. Simulation results of this SPDC

Λ	19.473 μm
w_{PPLN}	39 μm
q	0.0720 rad/μm
T_{degen}	71.9°C
L	10 mm

Table 4.1: Simulation parameters for modelling telecom PPLN photon pair source from fiber spectrometer measurements.

source were obtained spectrally and spatially integrating the functions defined in Section 2.2.1 (and *Mathematica* code modelled in Appendix B.1) to good experimental agreement, as seen in Fig. 4.4. Bandwidths of these computed spectral intensities were fitted with Gaussians to determine FWHM results.

4.3.2 Discussion

When paired with high detection efficiency SSPDs, long single-mode optical fibers provide a powerful tool in the arsenal of telecommunication-band quantum optical physicist. Such broadband single-photon sensitive spectral characterization tools in this wavelength regime are requisite for

SPDC source development for quantum communication. This method, however, due to material absorption losses, is limiting in its application for the NIR as absorption for 800 nm is 5 dB/km [102] compared with the pleasantly low 0.20 dB/km of 1550 nm [103] although single-photon detection efficiencies at 800 nm are not near as demanding (necessary cryostat for SSPDs) nor low.

Overall, this experimental characterization method shows good agreement theoretical simulations. It is evident that at the largely non-degenerate wavelengths of Fig. 4.4a, the uncertainty of the fiber spectrometer begins to increase. This is due to the GVD from the material properties of the fiber in the wavelength range of interest. In this experiment, the system calibration was completed at 1560 nm, which has an anomalous GVD parameter of $D_\lambda \approx +17$ ps/km-nm. Given a system maximum of $\delta t = 25$ ps, this results in a FWHM measurement uncertainty of $\Delta\lambda = \frac{\delta t}{|D_\lambda| L} \times (2\sqrt{2\ln 2}) = 43$ nm. The resolution of the fiber spectrometer can be calculated from $\delta\lambda = \frac{c\delta t}{dnL}$, which with the current system jitter is estimated to be 8 nm.

From my own exploration of the phasematching parameter space, I've observed that there exists no method to "squeeze" or "compress" the tuning curves of Type-0 cw SPDC, only shift in temperature. At the far, most non-degenerate wavelengths of Fig. 4.4a, the maximal central wavelength discrepancy is 42 nm (though still within uncertainty), although this should be noted that this is up to 215 nm away from SPDC degeneracy at 1560 nm – quite a large characterization range.

This particular implementation of the OPO fiber characterization was disadvantageous in that it didn't allow for an absolute time delay reference with known wavelength to compare the OPO characterization directly to photon pair measurements. This made extraction of the group velocity and GVD parameter from measurements much more difficult, especially to analyze over such a short 80 m length of optical fiber. Given the large spectral bandwidths of the photon pairs (Fig. 4.4b), any longer of a spectrometer fiber and the temporal spreading would have been too much to handle. However, the experimental setup calibration explained and implemented here could extend application of this technique to other time-delay measurement scenarios.

In the fiber calibration, since the OPO pulsed at a rate of 76 MHz, this resulted in a pulse period of 13.6 ns. However, due to the long length of the spectrometer fiber, multiple pulses existed in the fiber at a given time. This meant that the wavelength-dependent time delays were measured with respect to different pulses rather than the same pulse split two ways. Additionally, the repetition rate of the pulsed Ti:Sapphire laser which pumped the OPO was not perfectly stable, causing additional delay uncertainty. In the photon pair source characterization, the temporal resolution of the photon pair measurements are limited by the SSPDs with at an estimated 25 ps timing jitter. However, such long, 80 m fiber lengths did not exhibit a noticeable temperature-dependent phase or stress drift, even as the wavelength calibration was performed over two days, pointing to more practical use of such fiber lengths.

Chapter 5

Biphoton Up-Conversion

We now arrive at the natural culmination of the preceding chapters: up-conversion of down-conversion, the ultimate test of energy-time entanglement. We saw the development of the energy-time entangled photon pair source in Chapter 2 and the subsequent characterization of a chromatic dispersion-tuning prism compressor in Chapter 3. Here I bring it all together, an experiment to combine transform-limited biphoton wavepackets within a second nonlinear crystal to perform ultrafast coincidence as a first step toward entangled two-photon absorption. Additionally, from the process of "photon hunting" for such weak up-conversion signals, I also present a set of tools and measurement techniques for manipulating light in the ray-optic limit and probing properties of crystal phasematching.

Motivation for such an experiment has been discussed throughout this work. From the literature, others who have exerted such ultrashort temporal control over biphoton up-conversion have applied such properties to spatiotemporal study of SPDC [8–10]; higher-dimensional quantum information [11]; demonstrations of dispersion cancellation [13, 14]; and entanglement-enhanced two-photon absorption [15], as outlined in Table 5.1. With this level of biphoton spatiotemporal control, it is possible to apply such a quantum light source toward two-photon fluorescence detection with applications to microscopy and spectroscopy.

The following chapter presents a negative result. Here are characterizations of an experimental setup designed to efficiently measure femtosecond timescale, entanglement-assisted photon coincidences. Properties of major setup components will be presented followed by a discussion on the experimental design decisions, compared to the literature, on displaying the physical effect of interest.

Reference	Method		Purpose
	Crystal	Coherent control	
O'Donnell and U'Ren [9]	PPLN	Prism compressor	Time-resolved up-conversion
Pe'er et al. [8]	PPKTP	Spatial light modulator	Biphoton phase coherent control
Dayan et al. [36]	PPKTP	Prism compressor	Nonclassical power dependence
Jedrkiewicz et al. [10]	BBO	None, achromatic optics	Few fs time-resolved up-conversion
Schwarz et al. [11]	PPKTP	Spatial light modulator	d-dimensional qudit Bell state violation
O'Donnell [13]	PPLN	Separate prism compressors	Dispersion cancellation
Lerch et al. [14]	PPKTP	Spatial light modulator	Biphoton entanglement measurement
Dayan et al. [15]	PPTKP	Spatial light modulator	Entangled two-photon absorption in Rb vapour

Table 5.1: Selective literature for biphoton up-conversion.

5.1 Biphoton Up-Conversion: A Test of Ultrafast Coincidence Detection

Quantum frequency conversion (defined more precisely as frequency conversion retaining the quantum optical properties of the input [104]) has been demonstrated many times over in the last twenty years. Typically, the process is desirable for transforming photons to more convenient wavelengths for either detection [105]; quantum memory accessibility [106]; coherence tomography and sensing; [95, 107]; and telecommunication [108].

Most of the previously mentioned applications arise from a single-photon (typically detection heralded from its SPDC pair) combined in a nonlinear medium with a strong escort pulse, as seen in [109, 110] (among others). However what is of interest here is whole biphoton up-conversion where both the signal and idler photons from the same pair, sum together in frequency [9].

The experiment, a demonstration of extreme spatiotemporal localization from broadband SPDC, consists of three main sections:

1. a highly spatiotemporally (10s of fs, 100s of μm) localized SPDC source;
2. a low loss dispersion compensator (prism compressor) capable of correcting 1797 fs^2 to allow all biphoton frequency components to arrive within the ultrashort coherence time;
3. and an ultrafast nonlinear coincidence detector consisting of the second nonlinear crystal and low dark count, visible light single-photon detector,

as was implemented in Fig. 5.1.

Lens:	L1	L2	L3	L4	L5	OAP mirrors
Units [mm]	175	200	175	40	25.4	15

Table 5.2: Experiment focal lengths for up-conversion of down-conversion.

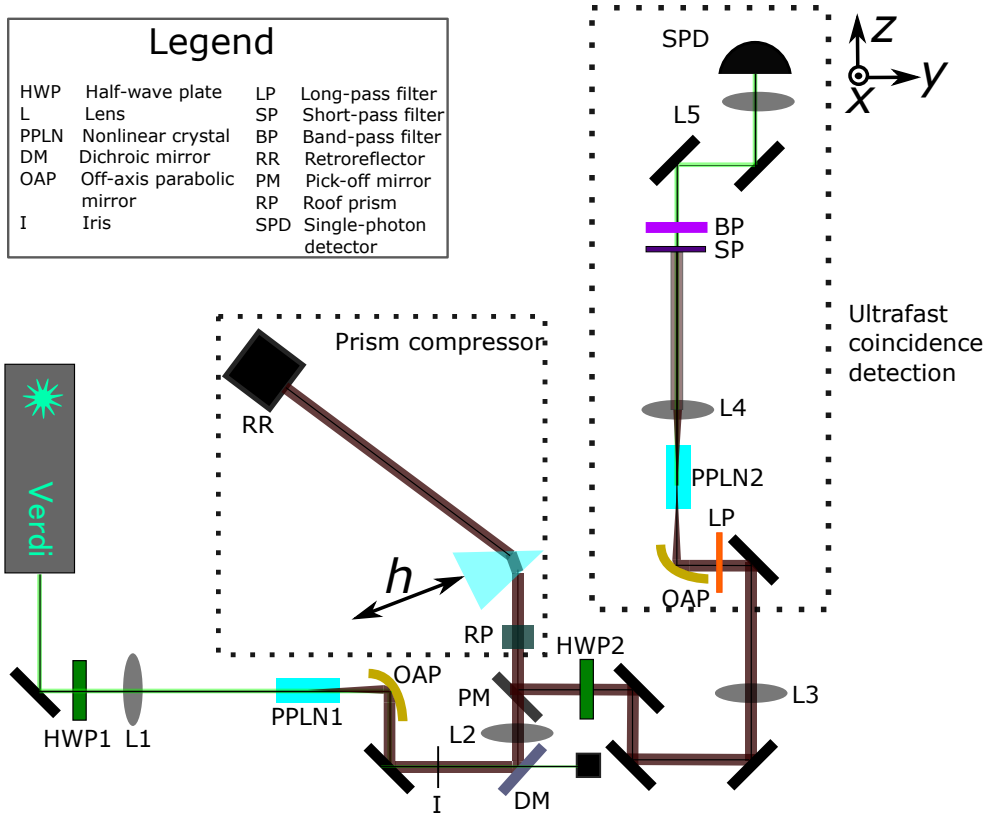

Figure 5.1: Designed and implemented experimental setup for up-conversion of down-conversion. Data collection was automated linear actuators in translation stages for h, x, y with manual translation, z. Lens focal lengths displayed in Table 5.2.

5.1.1 Experimental requirements

There are a number of inherent challenges to overcome when designing such an ultrafast coincidence detection experiment in a nonlinear crystal. First, both crystals must be phasematched to allow optimal frequency conversion of a single wavelength, $\lambda_p = \lambda_{\mathrm{SFG}}$. Second, chromatic dispersion accumulates through biphoton propagation through dispersive material, most substantially, the PPLN crystals. The calculated setup dispersion from Fig. 5.1 is 1797 fs^2, as calculated from Table ??. According to [9], a 3790 fs^2 GDD brings biphoton quantum frequency conversion probability to zero. A mere 198 fs^2 dispersion (12 mm of fused silica glass) in that experiment reduced the biphoton up-conversion coincidence peak by 55%. Third, the spatial mode of the SPDC must be controlled to enable a tight beam waist in the second crystal in addition to the spatial-spectral SPDC distribution controlled to allow propagation for both correlated signal and idler photons of a pair. What follows are strategies and solutions for mitigating these physical challenges and requirements.

As characterized in Chapter 2, the cw-pumped, spectrally broadband SPDC photon pair source is highly correlated in frequency and momentum with photon pairs being generated at angles beyond the collinear configuration. Since these up-conversion of down-conversion experiments result in very low, unheralded single-photon count rates (800-1000 counts/s), I chose high numerical aperture, gold off-axis parabolic (OAP) mirrors with a short effective focal length (15 mm) to collect the most photon pairs possible and thus, aim to increase the total frequency conversion efficiency. Jedrkiewicz et al. [10] demonstrated in 2012 that parabolic mirrors without dispersion compensation can be used to directly UCDC. In addition, due to the inherent symmetry of the overall process (532 nm $\rightarrow$ 1064 nm+1064 nm $\rightarrow$ 532 nm), I chose the focusing lens of the second crystal be the same as the output "collimation lens" (OAP mirror) of the first crystal.

Alignment of such OAP mirrors requires utmost care as photon pair momentum distributions should be preserved for later pair SFG. After consulting the literature, I settled upon the "dual beam" method [111] for OAP mirror alignment[1].

Given the combinations of Rayleigh length, collimating lens focal length, and total optical path length from crystal to crystal, the SPDC beam propagation exists in the ray-optics limit $(z - f) \gg z_0$ [19], we see

$$\frac{1}{f} \approx \frac{1}{z} + \frac{1}{z'}, \tag{5.1}$$

where z is the distance from the beam waist to lens of focal length f and z' is the distance from this lens to the new beam waist. This important as in this limit, "collimation" is not possible thus beam expansion will occur with propagation. This is detrimental as both photons of the photon pair must arrive at the second crystal, unshifted in time or space, for quantum frequency conversion to occur – they must not be clipped by the effective aperture of the optical setup.

[1] Other OAP mirror alignment methods I considered are [112] and [113]

A way to mitigate the constant biphoton beam expansion through the 250 cm optical path length to the second crystal is by implementing a beam relay. Due to space constraints from the vertically stacked, doubly-folded prism compressor (Section 1.4.3), the beam relay was asymmetrically imaged to an intermediate beam waist, as seen in Fig. 5.1. The lens relay was characterized for both down-conversion and an infrared laser by examining beam profiles (via CCD beam profile camera and knife edge measurements [114] and predictive modelling. The resulting lens system, optimized for down-conversion transmission, allowed a maximal setup throughput (66.5%) and minimal beam waist/spot size at the second crystal location (65 μm).

Optical component	GDD [fs^2]
PPLN crystals	1364
Roof prism	201
Half waveplates	84
Spectral filter (assumed 1 mm NBK7)	22
Relay lenses	125
Total	1797

Table 5.3: Estimated group delay dispersion calculated at 1064 nm from optics within biphoton portion of the experimental setup displayed in Fig. 5.1.

5.1.2 Experimental success metrics

Now that we've introduced the main experimental components of this biphoton up-conversion setup, let us now discuss physical tests for success. First, as mentioned previously, the frequency conversion in nonlinear crystals exhibits temperature dependence on its phasematching conditions. O'Donnell and U'Ren [9] demonstrated a complete loss of phasematching for +20°C change in PPLN2 temperature.

Second, the SHG is polarization-dependent. The frequency-conversion process can be "turned off" by linear polarization rotation[2].

Third, the biphoton up-conversion is sensitive to dispersion. This parameter can be continuously tuned via prism compressor adjustment.

Fourth and most practically, signal blocking by spectral filtering and beam blocking provides a useful sanity check. Installed prior to the detection portion of the setup, additional longpass ("green killing") and shortpass/bandpass ("IR killing") filter combinations are flipped in and out

[2] An important thing to consider when using polarization as an up-conversion test compared to unaffected down-conversion is to first verify if optical coatings and elements in the setup optimized for the visible up-conversion are not polarization-dependent for the infrared down-conversion.

of the optical path to infer the approximate wavelength of the single-photon detection counts. Counts that appear to be visible, not infrared, are then confirmed by fully blocking the down-conversion signal before the second crystal to verify if the signal appropriately disappears or is stray pump laser light.

Fifth, as predicted in [7] and demonstrated in [36], entangled photon pairs exhibit a linear power dependence on two-photon interactions such as two-photon absorption and SFG. However, since both photons of the same pair are required in frequency conversion, losses affect fluorescence or SFG quadratically. This can be used as test of success as stray pump single-photons should not follow both of these behaviours.

Finally, although it was not possible to manipulate in this experimental implementation, the inter-beam $g^{(2)}(\tau)$, or coincidence rate (as opposed to the intrabeam $g^{(2)}_{s,s}(\tau)$ or $g^{(2)}_{i,i}(\tau)$, commonly used as a metric for single-photon sources illuminating its multi-photon emission rate in a given mode [3]) between the signal and idler photon leads to a dramatic peak when $\tau = 0$.

The up-conversion portion of the experimental setup continued the beam relay, imaging the second PPLN crystal waist to that of the free-space single-photon detector [MPD PDM50CTC]. More detailed exploration and characterizations of this frequency conversion and detection are explored in the following section.

5.2 Selected "Ultrafast Coincidence Detector" Properties

As previously described, the second nonlinear crystal in the photon pair up-conversion experiment acts here as an "ultrafast coincidence detector". This nonlinear process of SFG has been described classically in Section 1.3.1.

In this experiment, the labelled "pump" frequency is fixed: whatever frequency pumps the SPDC is the frequency which the broadband down-conversion will precisely add up to. Thus, the second PPLN crystal must be optimal for this specific frequency. In this case, $\lambda_p = 532$ nm so the SFG wavelengths are 1064 nm + 1064 nm $\rightarrow$ 532 nm.

The following sections describe in more detail specific tuning properties and tolerances of SFG conversion as well as single-photon up-conversion collection and detection.

5.2.1 Phasematching acceptance bandwidth simulations

In order for frequency conversion to occur, the phase mismatch between the three electric fields must be zero. However, as discussed in Section 1.3.1, the function dictating the phasematching is a sinc function. How fast does that sinc function fall off? With what precision must the crystal parameters be set to still fall within this acceptance bandwidth? To answer these questions I simulate the phasematching acceptance bandwidth for the frequency conversion process of 1064 nm + 1064 nm $\rightarrow$ 532 nm using three models.

Method 1: Phasematching function

The first simulation approach is based on the previously discussed phasematching model of the reverse frequency conversion process, SPDC, of Section 2.2.1. Since the three waves of SPDC contain the same momentum and energy conservation for the reverse process of SFG, this existing model of a squared Eq. (2.1) is a reasonable choice for this purpose, as reproduced below.

$$\mathcal{S}^2(\omega_s, \mathbf{q}_s; \omega_i, \mathbf{q}_i) \approx \text{sinc}^2\left(\frac{\Delta k L}{2}\right) \tag{5.2}$$

$$\Delta k = \mathbf{k}_p - \mathbf{k}_s - \mathbf{k}_i - \frac{2\pi}{\Lambda} \tag{5.3}$$

For all other parameters remaining equal, each of the high-energy wavelength and crystal temperature are individually varied, as seen by the sinc functions of Fig. 5.2. By fitting a Gaussian to each of Fig. 5.2a and 5.2b, the estimated FWHM acceptance bandwidths, $\Delta\lambda_1$ and ΔT_1, are shown in Table 5.4.

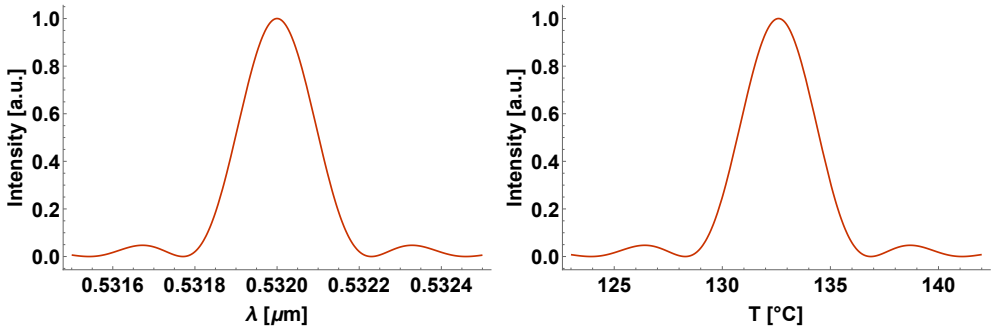

(a) Wavelength dependence

(b) Temperature dependence

Figure 5.2: Simulated phasematching tolerances for wavelength and crystal temperature using "Method 1" for a 5 mm sample of bulk 5% MgO:PPLN for frequency conversion 1064 nm + 1064 nm → 532 nm.

Method 2: Taylor series of phase mismatch

The spectral acceptance bandwidth can be also calculated by taking the first-order terms of a Taylor series of the phase mismatch Eq. (2.2) for $\Delta k|_{2\lambda_p}(\lambda - 2\lambda_p)$. Then, solving under the assumption $\Delta k = \frac{2\pi}{L}$. This results in the isolated spectral width, in terms of the down-conversion pump wavelength, λ_p,

$$\Delta\lambda_2 = \frac{2\pi}{|\frac{\partial}{\partial\lambda}\Delta k(2\lambda_p)|L}. \tag{5.4}$$

Second-order Taylor series provides no noticeable difference in acceptance bandwidth, $\Delta\lambda$.

Method 3: SHG bandwidth from periodically-poled material [115]

This result of Ref. [115] is similarly derived from the approach of the previous method. The authors note that spectral bandwidth, as defined by FWHM, is not affected the medium's periodic poling.

$$\Delta\lambda_3 = \frac{0.4429\lambda}{L}\left|\frac{n_2 - n_1}{\lambda} + \frac{\partial n_1}{\partial\lambda} - \frac{1}{2}\frac{\partial n_2}{\partial\lambda}\right|^{-1} \tag{5.5}$$

Translating the terminology from that of publication to this work, $\lambda_1 = \lambda_p = 532$ nm and $\lambda_2 = 1064$ nm for $L = 5$ mm.

Results and implications

The viable parameter ranges for a given summation wavelength, λ_p for the three methods are shown in Table 5.4.

Method:	1	2	3
T[°C]	3.58	–	–
$\Delta\lambda$ [nm]	0.19	0.68	0.46

Table 5.4: Up-conversion acceptance bandwidths, calculated via different methods

As previously mentioned, the down-conversion pump wavelength, λ_p, must be within the acceptance bandwidth of the second crystal. Given that the broadband down-conversion should sum to a bandwidth of the 5 MHz pump laser (5 fm at 532 nm), there shall be no problem fitting the down-conversion pump spectrum within the up-conversion acceptance bandwidth of the narrowest of the three, $\Delta\lambda_1$=0.19 nm[3].

Of greater relevance is the crystal oven temperature sensitivity. The phasematching sinc function of Fig. 5.2b shifts at 0.0545 nm/°C with a FWHM appreciable signal range of 3.58°C. Alternatively written, the optimal phasematching temperature induces a pump wavelength change of 18.3°C/nm.

5.2.2 Time-resolved phasematching: up-conversion crystal temperature characterizations

Now that the bounds of up-conversion crystal phasematching precision has been theoretically determined, experimental temperature characterization of the second PPLN crystal can now be undertaken.

[3] An interesting application of up-conversion phasematching functions can be found by deconvolution of the associated spectral effects to act as an up-conversion spectrometer at more convenient wavelengths [105].

One practical challenge when characterizing disparate frequency conversion harmonics is adequate sensitivity and spectral range for spectral analysis tools. As discussed in the previous section, the acceptance bandwidth must be temperature-tuned for maximal up-conversion of biphotons summing to the exact 532 nm pump frequency. Since available spectrum analysis tools were not sensitive for measuring both 532 nm pump frequency as well as the weak and broadband SPDC centered at 1064 nm, I present, in this section, a characterization method for pinpointing temperature dependence on SHG based off of a single spectrometer, a swept-source infrared laser, and time-resolved coincidence detection.

Extending the phasematching characterization of Section 5.2.1, a 10 nm FWHM, Gaussian intensity profiled spectral bandpass filter limited the time-dependent, broadband swept source laser of $\omega(t)$ to produce SHG in the PPLN crystal under test. However, here, detection timing information from the single-photon detector was compared within a narrow timing window to the trigger of the laser. This resulted in a time-delay histogram which was dependent on nonlinear crystal's temperature.

By analyzing the coincidence timing information and individual electronic signals for a given crystal temperature, a relation between laser frequency and sweep time can be made. Using this, the infrared wavelength of the laser sweep can be assigned as the optimal fundamental wavelength of the SHG phasematching at a given temperature. Assuming the $\omega(t)$ laser sweep begins and ends at spectral intensity half-max start- and stop- times, the time-to-frequency conversion can be calculated, as seen in Table 5.5.

Sweep time	21.475 μs
Conversion factor	74.2 nm/(21.475 μs)
$T = 160°$C delay	3.394 μs

Table 5.5: Measured quantities from Santec HSL-1000 swept-source laser and time-resolved SHG

An interesting result of such a study is the measurement of a calibration offset between different spectrometers. In this characterization, the frequency reference is based only on a spectrum taken on a single optical spectrum analyzer [Anritsu MS9710B] for the infrared swept-source laser. Using a different, silicon-based single-photon spectrometer [Acton SpectraPro 2750i], the temperature-dependent up-conversion measured under the same experimental conditions shows a relative spectrometer wavelength offset of 1.61 nm, as seen in Fig. 5.3. The validity of this approach is demonstrated by the near parallel nature of the two fitted slopes, as seen in Eq. (5.6) and Eq. (5.7), thus explaining differences from the calibration alone.

$$T_{\text{spectral}}(\lambda) = -11261.9 + 10.6962\lambda \tag{5.6}$$

$$T_{\text{time}}(\lambda) = -11180.2 + 10.6356\lambda \tag{5.7}$$

This method, although a technically and physically interesting technique, could similarly be determined on a single spectrometer by overlapping the temperature-dependent SHG of the

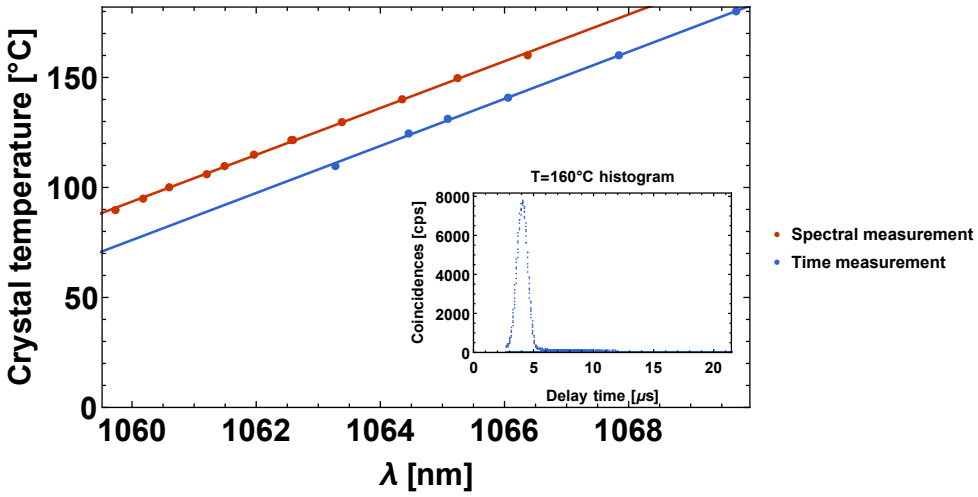

Figure 5.3: SHG Phasematching as measured by time-resolved measurements compared to independent spectrometer. Inset: coincidence histogram for $T = 160°\text{C}$ relative to laser sweep.

swept-source laser with that of the 532 nm down-conversion pump, which provided the final second crystal temperature used in the experiment.

5.2.3 Photon hunting in biphoton "pulse" stretch and space: experimental strategies

Due to the very low biphoton up-conversion counts expected from the literature, special care is needed to make sure misalignment and beam steering is not at fault for lack of detection. Here I present "photon hunting" strategies to explore the parameter space of the remaining experimental parameter uncertainties and tolerances. Additionally, I experimentally characterize and verify many of the physical behaviours of frequency conversion and beam propagation, theoretically discussed elsewhere.

Beyond the second PPLN crystal in the detection portion of the experiment, as seen in Fig. 5.1, an additional beam relay is required to focus on the 50 μm active area of the silicon-based single-photon detector [MPD PDM50CTC], optimized for detection of green light. As characterization remains uncertain after single frequency alignment due to chromatic focal shifts, he single-photon detector is mounted on a x, y, z translation stage set. With a beam profiling camera mounted on a translation stage, I studied the chromatic focal shifts and beam waist propagation through the focus of the final single-photon detector lens, as seen in Fig. 5.4. This plot shows some important information. First, the imaging system leading up does image the beam waist (radius) small enough to be within half of the single-photon detector active area, as hoped for. Second, it shows that the Gaussian beam of the laser does indeed behave differently than the multimode down-conversion. Collinearity through the 250 cm setup (including both crystals) still results in different focusing behaviours between the two light sources so one must take care not solely trust the alignment laser. Third, the focal shift of L5 is in the negative direction for shorter

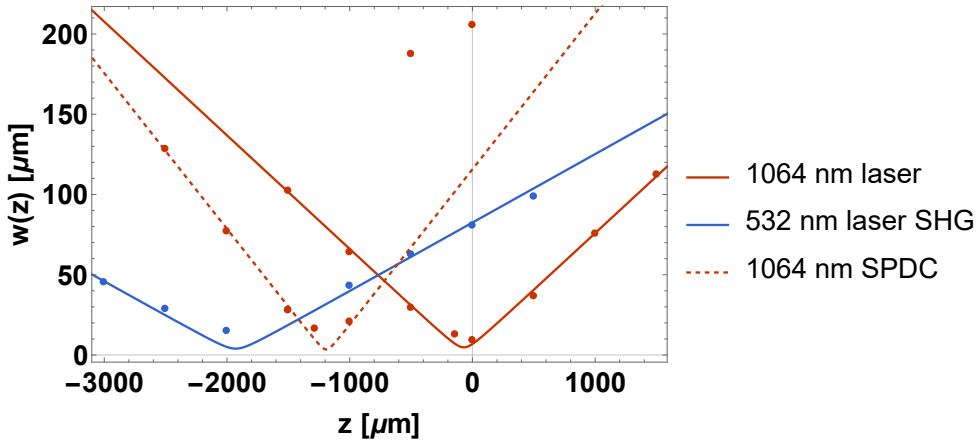

Figure 5.4: Wavelength-dependent focal shift in optimal single-photon detector position as measured by a beam profiling camera.

wavelengths for the laser and its up-conversion, about 2 mm closer to the lens, which is quite a lot. This is important as this focal shift trend points to a good starting detector z-position for biphoton quantum frequency conversion hunting.

Since tight focusing from a short focal length lens is required for the detector active area, misplacement of the detector could result in large photon flux variances outside of the beam waist. To combat this alignment uncertainty, I designed a LabVIEW-automated program to record single-photon detector counts while varying the x, y position in the detector plane and the prism compressor dispersion tuning with prism insertion, h. These automated scans of different detector planes and GDD compensation were associated with a manual z detector position. In total, a four-dimensional parameter space was investigated. An example of this system's capabilities and uses can be seen in Fig. 5.5a of an up-conversion of down-conversion scan prior to more aggressive background count reduction (scattered down-conversion pump light cannot be spectrally filtered out). Given that peak expected counts are so low at the best of times, and that photon flux through the detector beam waist varies so rapidly, I fit a 2D Gaussian to the resulting x, y raster scans to look for numerical trends across z and h slices in signal variance and amplitude beyond what was visible by inspection, as seen in Fig. 5.5b.

It is worth discussing the optical propagation effects induced by varying parameters such as prism insertion h and half-waveplate (HWP2) rotation on waist position in a single-photon detector plane. Conveniently, the detector plane raster scanning data acquisition and Gaussian-fit data analysis techniques were perfect for such investigations. Though varying prism glass insertion into the SPDC path does increase the effective optical path length (+1.22 cm of total optical path length per mm of h prism insertion), minimal beam wander and beam relay deterioration are detected in the imaging plane. Additionally, detection plane beam wander from angular displacements was characterized. Using HWP2 and rotating around the x-axis up to 470 μm of lateral displacement yielded no noticeable beam shift in the detection plane. Given the minimal

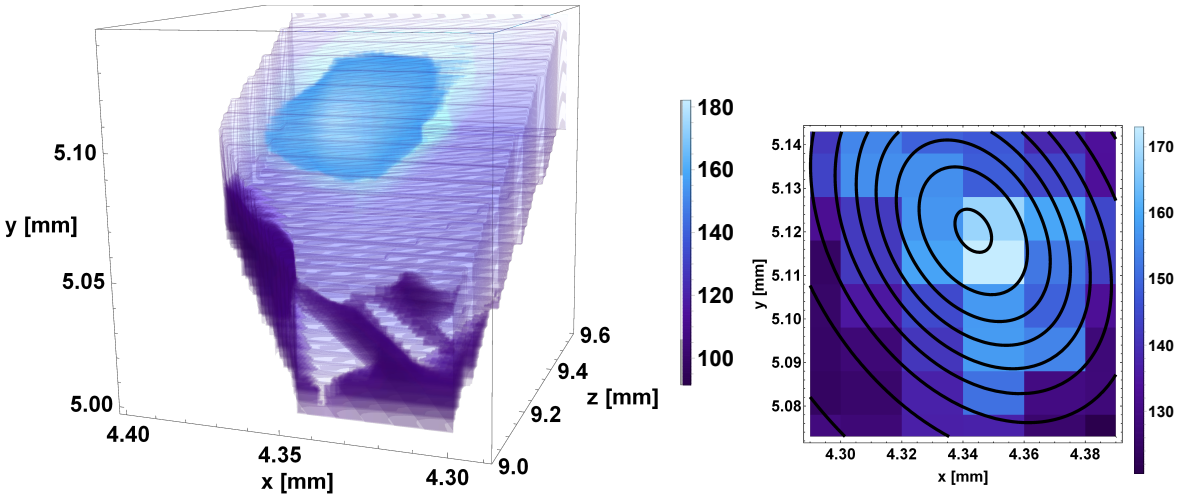

(a) 3D density plot of detected photon counts

(b) 2D slice for z=9.558 mm with fitted contours

Figure 5.5: Demonstration of 3-dimensional scanning capability: background counts [units: counts/second] through propagation z-slices at a single prism h position out of prism parameter space. Dark purple represents edge counts of 3D density plot volume.

detected displacements of any purposeful beam deviations, and the flexibility of the detection plane raster scanning fitting trend technology, I was confident that exploring the parameter space would not result in lack of detection due to misalignment.

5.3 Discussion

Although this experiment is heavily inspired by experimental quantum frequency conversion work by O'Donnell and U'Ren [9] and Jedrkiewicz et al. [10], it is important to point out a few potentially important experimental differences.

Extracted from lens choices in previously cited biphoton up-conversion experiments, it is noted that the beam waist of this experiment is half of that from others. This has a few effects: increased down-conversion efficiency as well as less well-defined spatial correlations [51]. If anything, this increase in frequency conversion efficiency is advantageous, allowing for a potential rate increase for up-converted biphotons above background noise. However, larger perpendicular wavevector ($\mathbf{q}$, in Chapter 2 notation) in the phase mismatch via momentum conservation yields larger spatial width or variance down-conversion momenta. Decreasing this spatial variance is related to an increased degree of (spatial) entanglement by reducing the two-photon wavefunction to a narrower distribution [75]. Careful reading of the literature and some personal correspondence revealed that all nonlinear crystal biphoton up-conversion experiments cited here included some form of spatial aperture to limit largely non-collinear down-conversion emission. Reasons why are hinted

at in [116] and are potentially related to two-photon wavefunction coherence [52].

The use of parabolic mirrors for lenses in biphoton frequency conversion is not, by definition, a problematic experimental difference. However in contrast, the OAP mirror implementation of Jedrkiewicz et al. [10] took place with much longer effective focal lengths ($f = 17.8$ cm) and without dispersive elements (except for the crystals) thus requiring no dispersion compensator. This choice resulted in the ability for direct, $4f$ imaging from crystal to crystal with a substantially shorter optical path length (≈ 71 cm) [117]. As discussed earlier, the choices of short OAP mirrors and dispersion compensation via prism compensation resulted in two additional lenses to beam relay between crystals, as seen in Fig. 5.1. These lenses, however, were not achromatic and result in a wavelength-dependent focal shift over the down-conversion spectral bandwidth. A later analysis by the same research group [70] theoretically determined the effect of imperfect imaging on up-conversion $g^{(2)}$ rates (referring to crystal being located a Δz displacement away from optimal). For their setup, a $\Delta z = 500$ μm focusing error (displacement in z-direction) reduced the biphoton coincidence rates by a factor of 1/12 and for $\Delta z = 2000$ μm, the peak was reduced close to that of the incoherent background.

Also, it was shown in Section 1.4.3 that prism compressors could tune GDD by means of both geometric and material dispersion (parameters q and h, respectively). However, these two parameters are not interchangeable as each affects different higher-order (third-order and above) spectral phase dependence. Shaked et al. [118] and Lukens et al. [40] demonstrated the need for dispersion cancellation of even orders of dispersion to allow for preserved biphoton phase summation in subsequent SFG[4]. Additionally, O'Donnell and U'Ren [9] mentioned the optimal prism compressor position for that biphoton frequency conversion experiment was to optimized into a position which compensated for fourth-order dispersion leaving a small, non-zero second-order dispersion. For the experiment discussed in this thesis, only second-order dispersion was considered.

5.3.1 Outlook and recommendations

Drawing upon all this knowledge, I propose the following recommendations. First, to remove the touchy short focal length OAP mirrors (and subsequent beam relay) and replace them with longer focal length lenses (similar to that of [9]). Perhaps with a longer Rayleigh length, beam expansion won't be as fierce and not require it. Secondly, for practical ease of automated photon hunting, I recommend the re-mounting of various spectral filters prior to the single-photon detector onto a motorized, remotely-controlled filter flip mount. This would save significant time as the process of reducing stray background counts from scattering of the 1 W pump laser from the free-space single-photon detector. This was time consuming as replacement of black shielding

[4]Higher-order phase effects for prism compressors (including most relevantly, 4th order) can be calculated from [119].

would need to occur whenever a sanity-check of a green-killing long-pass filter was flipped in to evaluate potential up-conversion signals. Third, theoretical investigations into prism compressor fourth-order dispersion dependencies could allow for a better initial prism compressor position for subsequent parameter space hunting.

It is unfortunate that, given the time restraints, it was not possible to experimentally follow through with all the suggested recommendations. From an experimental optics perspective, the characterizations presented here suggest that biphoton frequency conversion could have been possible with the optical component qualities of this setup. However given what has been shown in the literature it is probable that the current experimental design would not have yielded results.

I hope this chapter has been insightful and a good literature resource for those newly venturing into the fascinating and plentiful field of biphoton frequency conversion. There does exists a rich trove of experimental and theoretical literature investigating the fascinating ultrashort spatiotemporal capabilities of SPDC and I hope the presentation here allows them to be more accessible. Additionally, this could be a useful resource for future modelling, designing, manipulating, and characterizing frequency conversion phasematching in bulk PPLN.

Chapter 6

Conclusion

The energy-time degree of freedom for SPDC provides a rich trove of physics to be explored. The candidate SPDC source of this work, cw-pumped Type-0 interaction in bulk PPLN, have been shown to exhibit promising spatial-spectral correlations. In order to take advantage of the inherent spatiotemporal localization these spectrally broadband SPDC photon pairs provide, one must confront the continual villain of such temporally ultrafast biphoton wavepackets, chromatic dispersion. To correct for this, I built a compact dispersion manipulation tool in the form of a doubly folded prism compressor, which I've shown can be precisely measured through a white light interferometry technique inspired by spectral domain optical coherence tomography.

However chromatic dispersion doesn't always have to be the nemesis of spectrally broadband SPDC. Additionally, I have demonstrated that dispersive optical fibers can also be used to efficiently give spectral characterizations of SPDC tuning curves at the telecommunication wavelengths.

The demonstration of these properties through ultrafast coincidence detection in biphoton upconversion was ultimately unsuccessful due to constraints in time (and space), however hopefully with the knowledge and recommendations discussed here, implementation of this demanding quantum optical experiment can be made more accessible to novel applications in the fields of imaging and metrology.

References

[1] A. Stefanov. On the role of entanglement in two-photon metrology. *Quantum Science and Technology*, 2(2):025004, June 2017. ISSN 2058-9565. doi: 10.1088/2058-9565/aa6ae1. URL http://stacks.iop.org/2058-9565/2/i=2/a=025004?key=crossref.57c92b9044ea47ef149bdb6c85777b94.

[2] K. Edamatsu. Entangled Photons: Generation, Observation, and Characterization. *Japanese Journal of Applied Physics*, 46(11):7175–7187, November 2007. ISSN 0021-4922, 1347-4065. doi: 10.1143/JJAP.46.7175. URL http://stacks.iop.org/1347-4065/46/7175.

[3] M. D. Eisaman, J. Fan, A. Migdall, and S. V. Polyakov. Invited Review Article: Single-photon sources and detectors. *Review of Scientific Instruments*, 82(7):071101, July 2011. ISSN 0034-6748. doi: 10.1063/1.3610677. URL https://aip.scitation.org/doi/full/10.1063/1.3610677.

[4] M. Okano, H. H. Lim, R. Okamoto, N. Nishizawa, S. Kurimura, and S. Takeuchi. 0.54 m resolution two-photon interference with dispersion cancellation for quantum optical coherence tomography. *Scientific Reports*, 5(1), November 2016. ISSN 2045-2322. doi: 10.1038/srep18042. URL http://www.nature.com/articles/srep18042.

[5] D. A. Kalashnikov, E. V. Melik-Gaykazyan, A. A. Kalachev, Y. F. Yu, A. I. Kuznetsov, and L. A. Krivitsky. Quantum interference in the presence of a resonant medium. *Scientific Reports*, 7(1):11444, September 2017. ISSN 2045-2322. doi: 10.1038/s41598-017-11694-z. URL https://www.nature.com/articles/s41598-017-11694-z.

[6] F. Kaiser, P. Vergyris, D. Aktas, C. Babin, L. Labonté, and S. Tanzilli. Quantum enhancement of accuracy and precision in optical interferometry. *Light: Science & Applications*, 7(3):17163, March 2018. ISSN 2047-7538. doi: 10.1038/lsa.2017.163. URL https://www.nature.com/articles/lsa2017163.

[7] B. Dayan. Theory of two-photon interactions with broadband down-converted light and entangled photons. *Physical Review A*, 76(4), October 2007. ISSN 1050-2947, 1094-1622. doi:

10.1103/PhysRevA.76.043813. URL https://link.aps.org/doi/10.1103/PhysRevA.76.043813.

[8] A. Pe'er, B. Dayan, A. A. Friesem, and Y. Silberberg. Temporal Shaping of Entangled Photons. *Physical Review Letters*, 94(7), February 2005. ISSN 0031-9007, 1079-7114. doi: 10.1103/PhysRevLett.94.073601. URL https://link.aps.org/doi/10.1103/PhysRevLett.94.073601.

[9] K. A. O'Donnell and A. B. U'Ren. Time-Resolved Up-Conversion of Entangled Photon Pairs. *Physical Review Letters*, 103(12), September 2009. ISSN 0031-9007, 1079-7114. doi: 10.1103/PhysRevLett.103.123602. URL https://link.aps.org/doi/10.1103/PhysRevLett.103.123602.

[10] O. Jedrkiewicz, J.-L. Blanchet, E. Brambilla, P. Di Trapani, and A. Gatti. Detection of the Ultranarrow Temporal Correlation of Twin Beams via Sum-Frequency Generation. *Physical Review Letters*, 108(25), June 2012. ISSN 0031-9007, 1079-7114. doi: 10.1103/PhysRevLett.108.253904. URL https://link.aps.org/doi/10.1103/PhysRevLett.108.253904.

[11] S. Schwarz, B. Bessire, and A. Stefanov. Experimental violation of a d-dimensional Bell inequality using energy-time entangled photons. *International Journal of Quantum Information*, 12(07n08):1560026, 2014. URL https://worldscientific.com/doi/abs/10.1142/S0219749915600266.

[12] C. Bernhard, B. Bessire, T. Feurer, and A. Stefanov. Broadband energy-entangled photon for high resolution temporal sensing. page 97210L, April 2016. doi: 10.1117/12.2212450. URL http://proceedings.spiedigitallibrary.org/proceeding.aspx?doi=10.1117/12.2212450.

[13] K. A. O'Donnell. Observations of Dispersion Cancellation of Entangled Photon Pairs. *Physical Review Letters*, 106(6), February 2011. ISSN 0031-9007, 1079-7114. doi: 10.1103/PhysRevLett.106.063601. URL https://link.aps.org/doi/10.1103/PhysRevLett.106.063601.

[14] S. Lerch, T. Guerreiro, B. Sanguinetti, P. Sekatski, N. Gisin, and A. Stefanov. Entanglement, uncertainty and dispersion: a simple experimental demonstration of non-classical correlations. *Journal of Physics B: Atomic, Molecular and Optical Physics*, 50(5):055505, March 2017. ISSN 0953-4075, 1361-6455. doi: 10.1088/1361-6455/aa5b19. URL http://stacks.iop.org/0953-4075/50/i=5/a=055505?key=crossref.696480f130d0db536dbef3f67911c92f.

[15] B. Dayan, A. Pe'er, A. A. Friesem, and Y. Silberberg. Two Photon Absorption and Coherent Control with Broadband Down-Converted Light. *Physical Review Letters*, 93(2), July 2004.

ISSN 0031-9007, 1079-7114. doi: 10.1103/PhysRevLett.93.023005. URL https://link.aps.org/doi/10.1103/PhysRevLett.93.023005.

[16] E. E. Hoover and J. A. Squier. Advances in multiphoton microscopy technology. *Nature Photonics*, 7:93–101, 2013. doi: 10.1038/NPHOTON.2013.361. URL http://www.nature.com/nphoton/journal/v7/n2/abs/nphoton.2012.361.html.

[17] W. Denk, D. W. Piston, and W. W. Webb. Multi-photon molecular excitation in laser-scanning microscopy. In J. B. Pawley, editor, *Handbook of Biological Confocal Microscopy*, chapter 28, pages 535–549. Springer, New York, 3 edition, 2006. URL https://link.springer.com/chapter/10.1007/978-0-387-45524-2_28.

[18] J.-C. Diels and W. Rudolph. *Ultrashort laser pulse phenomena: fundamentals, techniques, and applications on a femtosecond time scale*. Optics and photonics. Elsevier / Academic Press, Amsterdam ; Boston, 2nd edition, 2006. ISBN 978-0-12-215493-5. URL https://www.elsevier.com/books/ultrashort-laser-pulse-phenomena/diels/978-0-12-215493-5.

[19] B. E. A. Saleh and M. C. Teich. *Fundamentals of photonics*. Wiley series in pure and applied optics. Wiley-Interscience, Hoboken, 2nd edition, 2007. ISBN 9780471358329.

[20] T. H. Maiman. Stimulated optical radiation in ruby. *Nature*, 187(4736):493–494, 1960. URL https://nature.com/articles/187493a0.

[21] R. W. Boyd. *Nonlinear optics*. Academic Press, Amsterdam, third edition, 2008. URL https://elsevier.com/books/nonlinear-optics/boyd/978-0-12-369470-6.

[22] J. A. Armstrong, N. Bloembergen, J. Ducuing, and P. S. Pershan. Interactions between Light Waves in a Nonlinear Dielectric. *Physical Review*, 127(6):1918–1939, 1962. URL https://journals.aps.org/pr/abstract/10.1103/PhysRev.127.1918.

[23] M. Yamada, N. Nada, M. Saitoh, and K. Watanabe. First-order quasi-phase matched $LiNbO_3$ waveguide periodically poled by applying an external field for efficient blue second-harmonic generation. *Applied Physics Letters*, 62(5):435–436, 1993. doi: http://dx.doi.org/10.1063/1.108925. URL http://scitation.aip.org/content/aip/journal/apl/62/5/10.1063/1.108925.

[24] D. S. Hum and Martin M. Fejer. Quasi-phasematching. *Comptes Rendus Physique*, 8 (2):180–198, March 2007. ISSN 16310705. doi: 10.1016/j.crhy.2006.10.022. URL http://linkinghub.elsevier.com/retrieve/pii/S1631070506002349.

[25] N. Quesada and J. E. Sipe. Why you should not use the electric field to quantize in nonlinear optics. *Optics Letters*, 42(17):3443–3446, September 2017. ISSN 1539-4794. doi: 10.1364/OL.42.003443. URL http://www.osapublishing.org/ol/abstract.cfm?uri=ol-42-17-3443.

[26] C. K. Hong and L. Mandel. Theory of parametric frequency down conversion of light. *Physical Review A*, 31(4):2409–2418, April 1985. ISSN 0556-2791. doi: 10.1103/PhysRevA.31.2409. URL https://link.aps.org/doi/10.1103/PhysRevA.31.2409.

[27] Z. Y. Ou, L. J. Wang, and L. Mandel. Vacuum effects on interference in two-photon down conversion. *Physical Review A*, 40(3):1428–1435, August 1989. ISSN 0556-2791. doi: 10.1103/PhysRevA.40.1428. URL https://link.aps.org/doi/10.1103/PhysRevA.40.1428.

[28] C. Gerry and P. Knight. *Introduction to Quantum Optics*. Cambridge University Press, New York, 2004. ISBN 9780521527354. doi: 10.1017/CBO9780511791239. URL https://cambridge.org/core/books/introductory-quantum-optics/B9866F1F40C45936A81D03AF7617CF44#.

[29] D. N. Klyshko. *Photons and Nonlinear Optics*. Gordon and Breach, New York, rev. and enl. ed. edition, 1988. ISBN 2881246699. URL https://books.google.ca/books?id=yJdYDwAAQBAJ.

[30] P. Kolenderski, W. Wasilewski, and K. Banaszek. Modeling and optimization of photon pair sources based on spontaneous parametric down-conversion. *Physical Review A*, 80 (1), July 2009. ISSN 1050-2947, 1094-1622. doi: 10.1103/PhysRevA.80.013811. URL https://link.aps.org/doi/10.1103/PhysRevA.80.013811.

[31] R. Loudon. *The quantum theory of light*. Oxford science publications. Oxford University Press, Oxford, 3rd edition, 2000. ISBN 0198501773. URL https://global.oup.com/academic/product/the-quantum-theory-of-light-9780198501763?cc=ca&lang=en&.

[32] D. H McIntyre. *Quantum mechanics: a paradigms approach*. Pearson, Boston, 2012. ISBN 9780321765796. URL http://catalogue.pearsoned.ca/educator/product/Quantum-Mechanics/9780321765796.page.

[33] J. Gea-Banacloche. Two-photon absorption of nonclassical light. *Physical Review Letters*, 62:1603–1606, Apr 1989. doi: 10.1103/PhysRevLett.62.1603. URL http://link.aps.org/doi/10.1103/PhysRevLett.62.1603.

[34] J. Javanainen and P. L. Gould. Linear intensity dependence of a two-photon transition rate. *Physical Review A*, 41:5088–5091, May 1990. doi: 10.1103/PhysRevA.41.5088. URL http://link.aps.org/doi/10.1103/PhysRevA.41.5088.

[35] N. Ph. Georgiades, E. S. Polzik, K. Edamatsu, H. J. Kimble, and A. S. Parkins. Nonclassical excitation for atoms in a squeezed vacuum. *Physical Review Letters*, 75:3426–3429, Nov 1995. doi: 10.1103/PhysRevLett.75.3426. URL http://link.aps.org/doi/10.1103/PhysRevLett.75.3426.

[36] B. Dayan, A. Pe'er, A. A. Friesem, and Y. Silberberg. Nonlinear Interactions with an Ultrahigh Flux of Broadband Entangled Photons. *Physical Review Letters*, 94(4), February 2005. ISSN 0031-9007, 1079-7114. doi: 10.1103/PhysRevLett.94.043602. URL https://link.aps.org/doi/10.1103/PhysRevLett.94.043602.

[37] Y. Shih. Entangled biphoton source - property and preparation. *Reports on Progress in Physics*, 66(6):1009–1044, June 2003. ISSN 0034-4885, 1361-6633. doi: 10.1088/0034-4885/66/6/203. URL http://stacks.iop.org/0034-4885/66/i=6/a=203?key=crossref.541892603a40e3d102d5107e268434b0.

[38] M. V. Chekhova. Two-photon spectron. *Journal of Experimental and Theoretical Physics Letters*, 75(5):225–226, March 2002. ISSN 0021-3640, 1090-6487. doi: 10.1134/1.1478518. URL https://link.springer.com/article/10.1134/1.1478518.

[39] J. M. Lukens and A. M. Weiner. Biphoton Pulse Shaping. In S. Wabnitz and B. J. Eggleton, editors, *All-Optical Signal Processing*, volume 194, pages 423–448. Springer International Publishing, Cham, 2015. ISBN 978-3-319-14991-2 978-3-319-14992-9. doi: 10.1007/978-3-319-14992-9_13. URL http://link.springer.com/10.1007/978-3-319-14992-9_13.

[40] J. M. Lukens, A. Dezfooliyan, C. Langrock, M. M. Fejer, D. E. Leaird, and A. M. Weiner. Demonstration of High-Order Dispersion Cancellation with an Ultrahigh-Efficiency Sum-Frequency Correlator. *Physical Review Letters*, 111(19), November 2013. ISSN 0031-9007, 1079-7114. doi: 10.1103/PhysRevLett.111.193603. URL https://link.aps.org/doi/10.1103/PhysRevLett.111.193603.

[41] D. Marcuse. *Light Transmission Optics*. Van Nostrand Reinhold, 2 edition, 1982.

[42] S. Diddams and J.-C. Diels. Dispersion measurements with white-light interferometry. *Journal of the Optical Society of America B*, 13(6):1120–1129, 1996. URL https://osapublishing.org/josab/abstract.cfm?uri=josab-13-6-1120.

[43] E. Treacy. Optical pulse compression with diffraction gratings. *IEEE Journal of Quantum Electronics*, 5(9):454–458, September 1969. ISSN 0018-9197. doi: 10.1109/JQE.1969.1076303. URL https://ieeexplore.ieee.org/document/1076303/.

[44] R. L. Fork, O. E. Martinez, and J. P. Gordon. Negative dispersion using pairs of prisms. *Optics Letters*, 9(5):150, May 1984. ISSN 0146-9592, 1539-4794. doi: 10.1364/OL.9.000150. URL https://www.osapublishing.org/abstract.cfm?URI=ol-9-5-150.

[45] Y. Shaked, S. Yefet, and A. Pe'er. The Prism-Pair: Simple Dispersion Compensation and Spectral Shaping of Ultrashort Pulses. *International Journal of Experimental Spectroscopic Techniques*, 1:4, 2016.

[46] U. Keller. Ultrafast solid-state lasers. volume 46 of *Progress in Optics*, pages 1 – 115. Elsevier, 2004. doi: http://dx.doi.org/10.1016/S0079-6638(03)46001-0. URL http://www.sciencedirect.com/science/article/pii/S0079663803460010.

[47] Eugene Hecht. *Optics*. Pearson Education, Inc., Boston, fifth edition. edition, 2016. ISBN 9780133977226. URL https://pearson.com/us/higher-education/program/Hecht-Optics-5th-Edition/PGM45350.html.

[48] S. Akturk, X. Gu, M. Kimmel, and R. Trebino. Extremely simple single-prism ultrashort-pulse compressor. *Optics Express*, 14(21):10101–10108, 2006. URL https://osapublishing.org/oe/abstract.cfm?uri=oe-14-21-10101.

[49] S. Akturk, X. Gu, P. Gabolde, and R. Trebino. The general theory of first-order spatio-temporal distortions of Gaussian pulses and beams. *Optics Express*, 13(21):8642–8661, October 2005. ISSN 1094-4087. doi: 10.1364/OPEX.13.008642. URL https://www.osapublishing.org/oe/abstract.cfm?uri=oe-13-21-8642.

[50] G. Brida, V. Caricato, M. V. Chekhova, M. Genovese, M. Gramegna, and T. Sh. Iskhakov. Testing ultrafast two-photon spectral amplitudes via optical fibres. *Optics Express*, 18: 12915, January 2010. doi: 10.1364/OE.18.012915. URL https://osapublishing.org/oe/abstract.cfm?uri=oe-18-12-12915.

[51] A. K. Gunther. Ultrafast coincidence characteristics of entangled photons towards entangled two-photon absorption. Master's thesis, University of Waterloo, 2014. URL https://uwspace.uwaterloo.ca/handle/10012/8234.

[52] Y.-H. Kim. Measurement of one-photon and two-photon wave packets in spontaneous parametric downconversion. *Journal of the Optical Society of America B*, 20(9):1959, September 2003. ISSN 0740-3224, 1520-8540. doi: 10.1364/JOSAB.20.001959. URL https://www.osapublishing.org/abstract.cfm?URI=josab-20-9-1959.

[53] P. Kok, W. J. Munro, K. Nemoto, T. C. Ralph, J. P. Dowling, and G. J. Milburn. Linear optical quantum computing with photonic qubits. *Reviews of Modern Physics*, 79(1):135–174, January 2007. doi: 10.1103/RevModPhys.79.135. URL https://link.aps.org/doi/10.1103/RevModPhys.79.135.

[54] N. Gisin and R. Thew. Quantum Communication. *Nature Photonics*, 1(3):165–171, March 2007. ISSN 1749-4893. doi: 10.1038/nphoton.2007.22. URL https://www.nature.com/articles/nphoton.2007.22.

[55] J. Huang, X. P. Xie, C. Langrock, R. V. Roussev, D. S. Hum, and M. M. Fejer. Amplitude modulation and apodization of quasi-phase-matched interactions. *Optics Letters*, 31(5): 604–606, March 2006. ISSN 1539-4794. doi: 10.1364/OL.31.000604. URL https://www.osapublishing.org/ol/abstract.cfm?uri=ol-31-5-604.

[56] A. Dosseva, Ł. Cincio, and A. M. Brańczyk. Shaping the joint spectrum of down-converted photons through optimized custom poling. *Physical Review A*, 93(1):013801, January 2016. doi: 10.1103/PhysRevA.93.013801. URL https://link.aps.org/doi/10.1103/PhysRevA.93.013801.

[57] P. G. Evans, R. S. Bennink, W. P. Grice, T. S. Humble, and J. Schaake. Bright Source of Spectrally Uncorrelated Polarization-Entangled Photons with Nearly Single-Mode Emission. *Physical Review Letters*, 105(25):253601, December 2010. doi: 10.1103/PhysRevLett.105.253601. URL https://link.aps.org/doi/10.1103/PhysRevLett.105.253601.

[58] Jian Sun. *MgO: LiNbO3 Nonlinear Wavelength Converters-From Visible to Mid-Infrared*. PhD Thesis, 2014. URL https://macsphere.mcmaster.ca/handle/11375/15414.

[59] M. Asobe, O. Tadanaga, T. Yanagawa, H. Itoh, and H. Suzuki. Reducing photorefractive effect in periodically poled ZnO- and MgO-doped LiNbO3 wavelength converters. *Applied Physics Letters*, 78(21):3163–3165, May 2001. ISSN 0003-6951, 1077-3118. doi: 10.1063/1.1374228. URL http://aip.scitation.org/doi/10.1063/1.1374228.

[60] Y. Furukawa, K. Kitamura, A. Alexandrovski, R. K. Route, M. M. Fejer, and G. Foulon. Green-induced infrared absorption in MgO doped $LiNbO_3$. *Applied Physics Letters*, 78 (14):1970–1972, April 2001. ISSN 0003-6951, 1077-3118. doi: 10.1063/1.1359137. URL http://aip.scitation.org/doi/10.1063/1.1359137.

[61] B. Chen, J. F. Campos, W. Liang, Y. Wang, and C.-Q. Xu. Wavelength and temperature dependence of photorefractive effect in quasi-phase-matched LiNbO3 waveguides. *Applied Physics Letters*, 89(4):043510, July 2006. ISSN 0003-6951, 1077-3118. doi: 10.1063/1.2240741. URL http://aip.scitation.org/doi/10.1063/1.2240741.

[62] A. Joobeur, B. E. A. Saleh, and M. C. Teich. Spatiotemporal coherence properties of entangled light beams generated by parametric down-conversion. *Physical Review A*, 50(4): 3349–3361, October 1994. ISSN 1050-2947, 1094-1622. doi: 10.1103/PhysRevA.50.3349. URL https://link.aps.org/doi/10.1103/PhysRevA.50.3349.

[63] S. P. Walborn, C. H. Monken, S. Pádua, and P. H. Souto Ribeiro. Spatial correlations in parametric down-conversion. *Physics Reports*, 495(4):87–139, October 2010. ISSN 0370-1573. doi: 10.1016/j.physrep.2010.06.003. URL http://www.sciencedirect.com/science/article/pii/S0370157310001602.

[64] O. Gayer, Z. Sacks, E. Galun, and A. Arie. Temperature and wavelength dependent refractive index equations for MgO-doped congruent and stoichiometric $LiNbO_3$. *Applied Physics B*, 91(2):343–348, May 2008. ISSN 0946-2171, 1432-0649. doi: 10.1007/s00340-008-2998-2. URL http://link.springer.com/10.1007/s00340-008-2998-2.

[65] H. B. Lin, S. H. Yu, C. X. Shi, X. J. Lv, P. Lv, Z. D. Xie, G. Zhao, and S. N. Zhu. Extended Sellmeier equation for the extraordinary refractive index of 5% MgO-doped congruent LiNbO3 at high temperature. *AIP Advances*, 7(9):095201, September 2017. ISSN 2158-3226. doi: 10.1063/1.4994104. URL http://aip.scitation.org/doi/10.1063/1.4994104.

[66] D. H. Jundt. Temperature-dependent Sellmeier equation for the index of refraction, n e, in congruent lithium niobate. *Optics Letters*, 22(20):1553–1555, 1997.

[67] O. Jedrkiewicz, A. Picozzi, M. Clerici, D. Faccio, and P. Di Trapani. Emergence of X-Shaped Spatiotemporal Coherence in Optical Waves. *Physical Review Letters*, 97(24): 243903, December 2006. doi: 10.1103/PhysRevLett.97.243903. URL https://link.aps.org/doi/10.1103/PhysRevLett.97.243903.

[68] P. Di Trapani, G. Valiulis, A. Piskarskas, O. Jedrkiewicz, J. Trull, C. Conti, and S. Trillo. Spontaneously Generated X-Shaped Light Bullets. *Physical Review Letters*, 91(9):093904, August 2003. doi: 10.1103/PhysRevLett.91.093904. URL https://link.aps.org/doi/10.1103/PhysRevLett.91.093904.

[69] A. Gatti, E. Brambilla, L. Caspani, O. Jedrkiewicz, and L. A. Lugiato. X Entanglement: The Nonfactorable Spatiotemporal Structure of Biphoton Correlation. *Physical Review Letters*, 102(22):223601, June 2009. doi: 10.1103/PhysRevLett.102.223601. URL https://link.aps.org/doi/10.1103/PhysRevLett.102.223601.

[70] E. Brambilla, O. Jedrkiewicz, L. A. Lugiato, and A. Gatti. Disclosing the spatiotemporal structure of parametric down-conversion entanglement through frequency up-conversion. *Physical Review A*, 85(6):063834, June 2012. doi: 10.1103/PhysRevA.85.063834. URL https://link.aps.org/doi/10.1103/PhysRevA.85.063834.

[71] S. Lerch, B. Bessire, C. Bernhard, T. Feurer, and A. Stefanov. Tuning curve of type-0 spontaneous parametric down-conversion. *JOSA B*, 30(4):953–958, April 2013. ISSN 1520-8540. doi: 10.1364/JOSAB.30.000953. URL https://www.osapublishing.org/abstract.cfm?uri=josab-30-4-953.

[72] K. N. Cassemiro, K Laiho, and C. Silberhorn. Accessing the purity of a single photon by the width of the HongOuMandel interference. *New Journal of Physics*, 12(11):113052, 2010. ISSN 1367-2630. doi: 10.1088/1367-2630/12/11/113052. URL http://stacks.iop.org/1367-2630/12/i=11/a=113052.

[73] T. Guerreiro, A. Martin, B. Sanguinetti, N. Bruno, H. Zbinden, and R. T. Thew. High efficiency coupling of photon pairs in practice. *Optics Express*, 21(23):27641, November 2013. ISSN 1094-4087. doi: 10.1364/OE.21.027641. URL https://www.osapublishing.org/oe/abstract.cfm?uri=oe-21-23-27641.

[74] M. Reichert, H. Defienne, and J. W. Fleischer. Optimizing the signal-to-noise ratio of biphoton distribution measurements. *arXiv:1802.00489 [physics, physics:quant-ph]*, January 2018. URL http://arxiv.org/abs/1802.00489. arXiv: 1802.00489.

[75] M. V. Fedorov. High resource of azimuthal entanglement in terms of Cartesian variables of noncollinear biphotons. *Physical Review A*, 97(1), January 2018. ISSN 2469-9926, 2469-9934. doi: 10.1103/PhysRevA.97.012319. URL https://link.aps.org/doi/10.1103/PhysRevA.97.012319.

[76] U. Glombitza and E. Brinkmeyer. Coherent frequency-domain reflectometry for characterization of single-mode integrated-optical waveguides. *Journal of Lightwave Technology*, 11(8):1377–1384, August 1993. ISSN 0733-8724. doi: 10.1109/50.254098. URL https://ieeexplore.ieee.org/document/254098/.

[77] W. Drexler, U. Morgner, R. K. Ghanta, F. X. Kartner, J. S. Schuman, and J. G. Fujimoto. Ultrahigh-resolution ophthalmic optical coherence tomography. *Nature Medicine*, 7(4):502–507, April 2001. URL https://nature.com/articles/nm0401_502.

[78] I. G. Cormack, F. Baumann, and D. T. Reid. Measurement of group velocity dispersion using white light interferometry: A teaching laboratory experiment. *American Journal of Physics*, 68(12):1146–1150, December 2000. ISSN 0002-9505, 1943-2909. doi: 10.1119/1.1286664. URL http://aapt.scitation.org/doi/10.1119/1.1286664.

[79] B. Cense, N. A. Nassif, T. C. Chen, M. C. Pierce, S.-H. Yun, B. H. Park, B. E. Bouma, G. J. Tearney, and J. F. de Boer. Ultrahigh-resolution high-speed retinal imaging using spectral-domain optical coherence tomography. *Optics Express*, 12(11):2435–2447, 2004. URL https://osapublishing.org/oe/abstract.cfm?uri=oe-12-11-2435.

[80] M. Wojtkowski, V. J. Srinivasan, T. H. Ko, J. G. Fujimoto, A. Kowalczyk, and J. S. Duker. Ultrahigh-resolution, high-speed, Fourier domain optical coherence tomography and methods for dispersion compensation. *Optics Express*, 12(11):2404–2422, 2004. URL https://osapublishing.org/oe/abstract.cfm?uri=oe-12-11-2404.

[81] W. Drexler, U. Morgner, F. X. Kärtner, C. Pitris, S. A. Boppart, X. D. Li, E. P. Ippen, and J. G. Fujimoto. In vivo ultrahigh-resolution optical coherence tomography. *Optics Letters*, 24(17):1221–1223, 1999. URL https://osapublishing.org/ol/abstract.cfm?uri=ol-24-17-1221.

[82] Y. Yasuno, Y.-J. Hong, S. Makita, M. Yamanari, M. Akiba, M. Miura, and T. Yatagai. In vivo high-contrast imaging of deep posterior eye by 1-m swept source optical coherence tomography and scattering optical coherence angiography. *Optics Express*, 15(10):6121–6139, 2007. URL https://osapublishing.org/oe/abstract.cfm?uri=oe-15-10-6121.

[83] Sebastian Marschall. *Frequency-swept Light Sources for Optical Coherence Tomography in the 1060 nm range*. PhD Thesis, Technical University of Denmark. URL http://orbit.dtu.dk/en/publications/frequencyswept-light-sources-for-optical-coherence-tomography-in-the-1060nm-range(b982134c-8835-4bff-bed2-4c066a061ec4).html.

[84] Max Chang. private communication.

[85] K. Naganuma, K. Mogi, and H. Yamada. Group-delay measurement using the Fourier transform of an interferometric cross correlation generated by white light. *Optics Letters*, 15(7):393, April 1990. doi: https://doi.org/10.1364/OL.15.000393. URL https://www.osapublishing.org/ol/abstract.cfm?uri=ol-15-7-393.

[86] G. D. Houser and E. Garmire. Balanced detection technique to measure small changes in transmission. *Applied Optics*, 33(6):1059–1062, February 1994. ISSN 2155-3165. doi: 10.1364/AO.33.001059. URL https://www.osapublishing.org/abstract.cfm?uri=ao-33-6-1059.

[87] Y. Yasuno, V. D. Madjarova, S. Makita, M. Akiba, A. Morosawa, C. Chong, T. Sakai, K.-P. Chan, M. Itoh, and T. Yatagai. Three-dimensional and high-speed swept-source optical coherence tomography for in vivo investigation of human anterior eye segments. *Optics Express*, 13(26):10652–10664, 2005. URL https://osapublishing.org/oe/abstract.cfm?uri=oe-13-26-10652.

[88] T.-J. Ahn and D. Y. Kim. Analysis of nonlinear frequency sweep in high-speed tunable laser sources using a self-homodyne measurement and Hilbert transformation. *Applied Optics*, 46(13):2395–2400, May 2007. URL https://osapublishing.org/ao/abstract.cfm?id=131884.

[89] T. Wu, Z. Ding, L. Wang, and M. Chen. Spectral phase based k-domain interpolation for uniform sampling in swept-source optical coherence tomography. *Optics Express*, 19(19):18430, 2011. doi: https://doi.org/10.1364/OE.19.018430. URL https://www.osapublishing.org/oe/abstract.cfm?uri=oe-19-19-18430.

[90] S. H. Yun, G. J. Tearney, J. F. de Boer, and B. E. Bouma. Removing the depth-degeneracy in optical frequency domain imaging with frequency shifting. *Optics Express*, 12(20):4822–4828, October 2004. ISSN 1094-4087. doi: 10.1364/OPEX.12.004822. URL https://www.osapublishing.org/abstract.cfm?uri=oe-12-20-4822.

[91] J. Benesty, J. Chen, Y. (Arden) Huang, and S. Doclo. Study of the Wiener Filter for Noise Reduction. In J. Benesty, Sh. Makino, and J. Chen, editors, *Speech Enhancement*, pages 9–41. Springer Berlin Heidelberg, Berlin, Heidelberg, 2005. ISBN 978-3-540-27489-6. URL https://doi.org/10.1007/3-540-27489-8_2. DOI: 10.1007/3-540-27489-8_2.

[92] S. C. Douglas. Introduction to adaptive filters. In *Digital signal processing handbook*, Electrical Engineering Handbook, pages 7–12. CRC Press, 2nd edition, 1999. URL https://crcpress.com/The-Digital-Signal-Processing-Handbook-Second-Edition---3-Volume-Set/Madisetti/p/book/9781420045635.

[93] A. G. Van Engen, S. A. Diddams, and T. S. Clement. Dispersion measurements of water with white-light interferometry. *Applied Optics*, 37(24):5679–5686, August 1996. URL https://osapublishing.org/ao/abstract.cfm?uri=ao-37-24-5679.

[94] Y. Arosa, E. L. Lago, L. M. Varela, and R. de la Fuente. Spectrally resolved white light interferometry to measure material dispersion over a wide spectral band in a single acquisition. *Optics Express*, 24(15):17303, July 2016. ISSN 1094-4087. doi: 10.1364/OE.24.017303. URL https://www.osapublishing.org/abstract.cfm?URI=oe-24-15-17303.

[95] A. Vallés, G. Jiménez, L. J. Salazar-Serrano, and J. P. Torres. Optical sectioning in induced coherence tomography with frequency-entangled photons. *Physical Review A*, 97(2):023824, February 2018. doi: 10.1103/PhysRevA.97.023824. URL https://link.aps.org/doi/10.1103/PhysRevA.97.023824.

[96] S. M. Lee, H. Kim, M. Cha, and H. S. Moon. Polarization-entangled photon-pair source obtained via type-ii non-collinear spdc process with ppktp crystal. *Optics Express*, 24(3): 2941, Feb 2016. ISSN 1094-4087. doi: 10.1364/oe.24.002941. URL http://dx.doi.org/10.1364/OE.24.002941.

[97] R. Shimizu and K. Edamatsu. High-flux and broadband biphoton sources with controlled frequency entanglement. *Optics Express*, 17(19):16385–16393, 2009. URL http://www.opticsexpress.org/abstract.cfm?URI=oe-17-19-16385.

[98] C. M. Natarajan, M. G. Tanner, and R. H. Hadfield. Superconducting nanowire single-photon detectors: physics and applications. *Superconductor Science and Technology*, 25 (6):063001, 2012. ISSN 0953-2048. doi: 10.1088/0953-2048/25/6/063001. URL http://stacks.iop.org/0953-2048/25/i=6/a=063001.

[99] M. Avenhaus, A. Eckstein, P. J. Mosley, and C. Silberhorn. Fiber-assisted single-photon spectrograph. *Optics Letters*, 34(18):2873–2875, 2009. URL http://ol.osa.org/abstract.cfm?URI=ol-34-18-2873.

[100] T. Lutz, P. Kolenderski, and T. Jennewein. Toward a downconversion source of positively spectrally correlated and decorrelated telecom photon pairs. *Optics Letters*, 38(5):697–699, Mar 2013. URL https://osapublishing.org/ol/abstract.cfm?uri=ol-38-5-697.

[101] T. Lutz, P. Kolenderski, and T. Jennewein. Demonstration of spectral correlation control in a source of polarization entangled photon pairs at telecom wavelength. *Optics Letters*, 39(6):

1481, September 2014. URL https://osapublishing.org/ol/abstract.cfm?uri=ol-39-6-1481.

[102] Thorlabs. Single Mode Fiber: 780 to 970 nm. URL https://www.thorlabs.com/newgrouppage9.cfm?objectgroup_id=949. Part number SM800-5.6-125.

[103] Corning. Corning® SMF-28e+® Optical Fiber. URL http://www.corning.com/media/worldwide/coc/documents/PI1463_07-14_English.pdf.

[104] J. Huang and P. Kumar. Observation of quantum frequency conversion. *Physical Review Letters*, 68(14):2153–2156, April 1992. ISSN 0031-9007. doi: 10.1103/PhysRevLett.68.2153. URL https://link.aps.org/doi/10.1103/PhysRevLett.68.2153.

[105] G.-L. Shentu, J. S. Pelc, X.-D. Wang, Q.-C. Sun, M.-Y. Zheng, M. M. Fejer, Q. Zhang, and J.-W. Pan. Ultralow noise up-conversion detector and spectrometer for the telecom band. *Optics Express*, 21(12):13986–13991, June 2013. ISSN 1094-4087. doi: 10.1364/OE.21.013986. URL https://www.osapublishing.org/oe/abstract.cfm?uri=oe-21-12-13986.

[106] B. Albrecht, P. Farrera, X. Fernandez-Gonzalvo, M. Cristiani, and H. de Riedmatten. A waveguide frequency converter connecting rubidium-based quantum memories to the telecom C-band. *Nature Communications*, 5:3376, February 2014. ISSN 2041-1723. doi: 10.1038/ncomms4376. URL https://www.nature.com/articles/ncomms4376.

[107] A. V. Paterova, H. Yang, C. An, D. A. Kalashnikov, and L. A. Krivitsky. Tunable optical coherence tomography in the infrared range using visible photons. *Quantum Science and Technology*, 3(2):025008, 2018. ISSN 2058-9565. doi: 10.1088/2058-9565/aab567. URL http://stacks.iop.org/2058-9565/3/i=2/a=025008.

[108] J. S. Pelc, L. Ma, C. R. Phillips, Q. Zhang, C. Langrock, O. Slattery, X. Tang, and M. M. Fejer. Long-wavelength-pumped upconversion single-photon detector at 1550 nm: performance and noise analysis. *Optics Express*, 19(22):21445, October 2011. ISSN 1094-4087. doi: 10.1364/OE.19.021445. URL https://www.osapublishing.org/oe/abstract.cfm?uri=oe-19-22-21445.

[109] S. Ramelow, A. Fedrizzi, A. Poppe, N. K. Langford, and A. Zeilinger. Polarization-entanglement-conserving frequency conversion of photons. *Physical Review A*, 85(1):013845, January 2012. doi: 10.1103/PhysRevA.85.013845. URL https://link.aps.org/doi/10.1103/PhysRevA.85.013845.

[110] J.-P. W. MacLean, J. M. Donohue, and K. J. Resch. Direct Characterization of Ultrafast Energy-Time Entangled Photon Pairs. *Physical Review Letters*, 120(5):053601, January 2018. doi: 10.1103/PhysRevLett.120.053601. URL https://link.aps.org/doi/10.1103/PhysRevLett.120.053601.

[111] Y. H. Lee. Alignment of an off-axis parabolic mirror with two parallel He-Ne laser beams. *Optical Engineering*, 31(11):2287, 1992. ISSN 00913286. doi: 10.1117/12.59951. URL http://opticalengineering.spiedigitallibrary.org/article.aspx?doi=10.1117/12.59951.

[112] C. Bond and C. A. Pipan. How To Align An Off-Axis Parabolic Mirror. In *Reflective Optics II*, volume 1113, pages 236–249. International Society for Optics and Photonics, October 1989. doi: 10.1117/12.955592. URL https://www.spiedigitallibrary.org/conference-proceedings-of-spie/1113/0000/How-To-Align-An-Off-Axis-Parabolic-Mirror/10.1117/12.955592.short.

[113] J. A. Murphy. Distortion of a simple Gaussian beam on reflection from off-axis ellipsoidal mirrors. *International Journal of Infrared and Millimeter Waves*, 8(9):1165–1187, September 1987. ISSN 0195-9271, 1572-9559. doi: 10.1007/BF01010819. URL https://link.springer.com/article/10.1007/BF01010819.

[114] M. A. de Araújo, R. Silva, E. de Lima, D. P. Pereira, and P. C. de Oliveira. Measurement of Gaussian laser beam radius using the knife-edge technique: improvement on data analysis. *Applied Optics*, 48(2):393, January 2009. ISSN 0003-6935, 1539-4522. doi: 10.1364/AO.48.000393. URL https://www.osapublishing.org/abstract.cfm?URI=ao-48-2-393.

[115] M. M. Fejer, G. A. Magel, Dieter H. Jundt, and Robert L. Byer. Quasi-Phase-Matched Second Harmonic Generation: Tuning and Tolerances. *IEEE Journal of Quantum Electronics*, 28(11):2631–2654, 1992. URL https://ieeexplore.ieee.org/document/161322/.

[116] G. D. Jimenez, V. G. Garces, and K. A. O'Donnell. Angular and temperature dependence of photon pair rates in spontaneous parametric down-conversion from a periodically poled crystal. *Physical Review A*, 96(2), August 2017. ISSN 2469-9926, 2469-9934. doi: 10.1103/PhysRevA.96.023828. URL https://link.aps.org/doi/10.1103/PhysRevA.96.023828.

[117] O. Jedrkiewicz, J.-L. Blanchet, A. Gatti, E. Brambilla, and P. Di Trapani. High visibility pump reconstruction via ultra broadband sum frequency mixing of intense phase-conjugated twin beams. *Optics Express*, 19(14):12903–12912, July 2011. ISSN 1094-4087. doi: 10.1364/OE.19.012903. URL https://www.osapublishing.org/oe/abstract.cfm?uri=oe-19-14-12903.

[118] Y. Shaked, S. Yefet, T. Geller, and A. Pe'er. Octave-spanning spectral phase control for single-cycle bi-photons. *New Journal of Physics*, 17(7):073024, 2015. ISSN 1367-2630. doi: 10.1088/1367-2630/17/7/073024. URL http://stacks.iop.org/1367-2630/17/i=7/a=073024.

[119] E. Cojocaru. Analytic expressions for the fourth- and the fifth-order dispersions of crossed prisms pairs. *Applied Optics*, 42(34):6910–6914, December 2003. ISSN 2155-3165. doi:

10.1364/AO.42.006910. URL https://www-osapublishing-org.proxy.lib.uwaterloo.ca/ao/abstract.cfm?uri=ao-42-34-6910.

[120] Leonard Mandel and Emil Wolf. *Optical coherence and quantum optics*. Cambridge University Press, Cambridge [England] ; New York, 1995. ISBN 0521417112. URL https://cambridge.org/core/books/optical-coherence-and-quantum-optics/F8CB94C70FA64CD3FB60890CA2048168.

[121] Mathias Johansson. The Hilbert transform. Master's thesis, Växjö University, 1999. URL http://www.fuchs-braun.com/media/d9140c7b3d5004fbffff8007fffffff0.pdf.

[122] A. V. Smith. SNLO. URL http://www.as-photonics.com/snlo.

[123] K. Shalm. SPDCalc. URL http://spdcalc.org/.

[124] *Encyclopedia of Optical Engineering*. Taylor & Francis, April 2011. ISBN 978-0-8247-0940-2 978-0-8247-0939-6. doi: 10.1081/E-EOE. URL http://www.tandfonline.com/doi/book/10.1081/E-EOE.

Appendix A

Phase Extraction

A.1 Hilbert Transform

The purpose of implementing a Hilbert transform is to create a complex analytic signal from real-valued interferometer data [80, 120] so as to extract a time-dependent phase [88].

The Hilbert function can be defined as [121]

$$H\{f(t)\} = \frac{1}{\pi} P \int_{-\infty}^{\infty} \frac{f(\tau)}{t-\tau} d\tau \tag{A.1}$$

for P being the Cauchy principal value where the integral exists.

The Hilbert transform has the following properties [88, 121]:

- $H\{f(t)\}$ of a given sinusoidal wave function $f(t)$ is the same as the original function $f(t)$, except that the phase of the waveform is shifted by $\pi/2$
- Linearity

  For a function $f(t) = c_1 f_1(t) + c_2 f_2(t)$, the Hilbert transform of $f(t)$ is $H\{f(t)\} = c_1 H\{f_1(t)\} + c_2 H\{f_2(t)\}$.
- $H^2 = -I$

  Multiple Hilbert transforms on real function give same real function with altered sign
- Hilbert transform of a derivative of a function is equal to the Hilbert transform of the function
- Orthogonality

  The real function and its Hilbert transform are orthogonal
- $\pm\pi/2$ phase shift in frequency domain, as interpreted by multiplication with imaginary value $\pm i$

A.2 Phase Extraction From Sample Wavepacket

As an example, for a linearly chirped wavepacket with a Gaussian intensity distribution, $E(t) = \exp[-2\ln 2(t/\tau_p)^2]\cos(\omega_0 t + \phi'' t^2)$, where the FWHM is $\tau_p = \frac{8\pi}{\omega_0}$, and $\phi'' = \frac{8}{\tau^2}$, the phase can be extracted by using the Hilbert transform on the list to create a strong analytic signal. Directly, the resulting phase $\phi(t) = \text{Arg}\{\frac{\text{Re}}{\text{Im}}\}$ is Fig. A.1b. Using an unwrapping function[1] searching for jumps modulo $\pi/2$, a continuous phase, Fig. A.1c can be fit to a second-order polynomial and the fitting coefficients can elucidate the chirp.

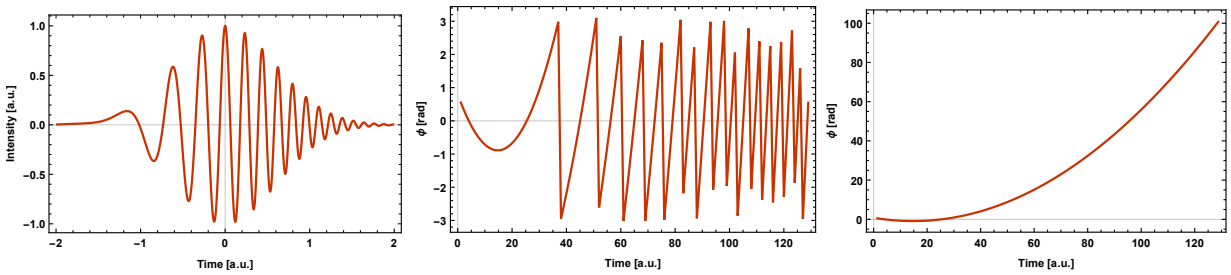

(a) Chirped wavepacket (b) Wrapped phase (c) Unwrapped phase

Figure A.1: Example wavepacket phase extraction

Fringes are modelled via the $\text{Re}\left[\exp\left[-i\left(\frac{d_{\text{air}}(\omega_l+\Omega)}{c} - \frac{d(\Omega-\omega_l)n_{\text{NBK7}}(2\pi c/(\Omega-\omega_l))}{c}\right)\right]\right]$.

A.3 Phase Extraction Dependence on Interferometer Displacements

	Position 1		Position 2		Position 4		Position 5	
	Coefficient	Std Err	Coefficient	Std Err	Coefficient	Std Err	Coefficient	Std Err
1	115	0.009	59	0.008	52	0.009	117	0.009
x	2260	0.19	1143	0.17	1048	0.21	2138	0.21
x^2	1163	6.7	1165	6.1	-1105	7.7	-1132	7.6

Table A.1: Fitting coefficients across all mirror displacements of {Air, -setup} (linearized (hilbert-extracted) phase, p.189, lin avg). Adjusted R-squared goodness of fit > 0.999

[1] *Mathematica* code modified from http://forums.wolfram.com/mathgroup/archive/1998/May/msg00107.html

	{Air,-setup}	{Air, +glass}	{Air, -glass}	{glass, +glass}	{Air, glass -glass}
Adjusted theory	-1973	990	95	525	560
Hilbert	-2289	981	179	412	753
Fringe Count	-2205	965	321	613	840

Table A.2: Extracted GDD results for all dispersion scenarios

A.4 Uncertainty in Interferometer Measurements

The uncertainty in this characterization can be attributed to multiple sources stemming from prism compressor parameters (h, q) and interferometer stability (Δlin). Assuming uncorrelated errors,

$$\Delta\text{GDD} = \sqrt{|(\delta h)(\Delta h)|^2 + |(\delta q)(\Delta q)|^2 + |\Delta\text{lin}|^2} = 146 \text{ fs}^2 \tag{A.2}$$

As was already observed, prism insertion, h, can have a large influence.

	Δh	Δq	Δlin
Error	± 1 mm	± 5 mm	4 fs^2
	δh	δq	
Uncertainty	100 fs^2/mm	-21 fs^2/mm	

Table A.3: Variable definitions from Eq. (A.2). Prism variables are derived from Section 1.4.3 and the linearization, Δlin, is from extracting variance in GDD from theoretical fringes with perfect displacement.

Between the two phase extraction methods, the Hilbert transform method has more data points to base it off of, whereas for the Fringe Counting method, it depends on the amount of zero crossings to fit a polynomial off of. In addition, for these small amounts of dispersion, the "chirp" is quite small over the spectral bandwidth range.

The calculated uncertainty of the measurements is 146.2 fs^2 from $\sqrt{|(\delta h)(\Delta h)|^2 + |(\delta q)(\Delta q)|^2 + |\Delta\text{lin}|^2}$, where

- Error: $\Delta h = \pm 1$ mm, $\Delta q = \pm 0.5$ cm, $\Delta\text{lin} = \pm 4.31$ fs^2
- insertion: $\delta h = 100$ fs^2/mm, prism-retroreflector: $\delta q = 1000$ fs^2/4.7 mm $= -213$ fs^2/cm (from plots)

The prism compressor errors are obtained from prism compressor alignment estimates and the uncertainties from Section 1.4.3.

When comparing the variances, no real difference between the methods.

Appendix B

Code

B.1 White Light Interferometry Data Analysis

Note about copy-paste to *Mathematica*: the (^) and (_) symbols don't render properly. Make sure to Find-and-Replace the (^), re-add the (_), and get rid of the ....

Phase unwrap modified from http://forums.wolfram.com/mathgroup/archive/1998/May/msg00107.html

Listing B.1: Phase unwrap

```
renormalize[args_]:=Module[{pairs, diffs, j, len=Length[args], corr=0},pairs=Partition[args,2,1];
 diffs=Map[#[[1]]-#[[2]]&,pairs];
PrependTo[diffs,0];
 diffs=2*Pi*Sign[Chop[diffs,Pi]];
Table[corr+=diffs[[j]];
corr+args[[j]],{j,1,len}]]
```

Listing B.2: Hilbert function

```
 hilbert[data_?VectorQ]:=Module[{fopts=FourierParameters->{1,-1},e,n},
e=Boole[EvenQ[n=Length[data]]];
Im[InverseFourier[Fourier[data,fopts]*
PadRight[ArrayPad[ConstantArray[2,Quotient[n,2]-e],{1,e},1],n],fopts]]]/;  And @@ Thread[Im[data]==0]
```

Zero-crossing *Mathematica* function modified from http://mathematica.stackexchange.com/questions/10640/find-zero-crossing-in-a-list

Listing B.3: Zero-crossing

```
zeroCrossings[ l_List , freq_List ] := Module[{t, u, v, pairs , startpos },
  t = {Sign[l ], Range[Length[l ]]} // Transpose;(*List of-1,0,1 only*)
  u = Select[t , First [#] != 0 &];(*Ignore zeros*)
  v = SplitBy[u, First ]; (*Group into runs of+and-values*)
  pairs = {Most[Max[#[[All, 2]]] & /@ v], Rest[Min[#[[All, 2]]] & /@ v]} // Transpose;
  startpos = First /@ pairs ;
  Table[{ freq [[ startpos [[k ]]]], k*\[Pi ]}, {k, 1, Length[startpos ]}]
  ]
```

A word of caution for the zero-crossing function: the frequency abscissa list is required for operation. Also note the code's sensitivity to list length.

B.2 Cones: Spatial/Spectral Integration Functions

For simulation SPDC there are a number of resources without needing to write your own code. Two great resources are SNLO [122] and SPDCalc [123].

Inevitably, for ease of comparison between measured SPDC properties and simulation, I simulated spatial and spectral intensities in *Mathematica*. It turns out when integrating broadband, cw-pumped SPDC over large spectral and spatial ranges, it can become quite computationally demanding. As such, I after experimenting on different integration bounds, I settled upon a method for determining the minimal integration bounds to simulate the observed SPDC properties, as dictated in Appendix B.2.2. What follows is *Mathematica* code (most recently tested in version 11.3.0.0)

B.2.1 SPDC Integration functions

For ease of use with Sellmeier equations as well as inherent units of dispersion, the following code definitions are in the units of μm/fs which additionally yields convenient constants such as the speed of light in vacuum, $c = 0.2998$ μm/fs and wavelength of interest, $\lambda_0 = 1.064$ μm.

Mathematica functions

Listing B.4: Periodically-poled lithium niobate crystal properties

```
ne=Compile[{{\[Omega],_Real},{T,_Real}},Sqrt[5.756+(2.860*10^-6)*(T-24.5)(T+570.82)+
(0.0983+(4.700*10^-8)*(T-24.5)(T+570.82))/((2\[Pi] ...
    .2998/\[Omega])^2-(.2020+(6.113*10^-8)*(T-24.5)(T+570.82))^2)+
(189.32+(1.516*10^-4)*(T-24.5)(T+570.82))/((2\[Pi] ...
    .2998/\[Omega])^2-12.52^2)-(1.32*10^-2)*(2\[Pi] .2998/\[Omega])^2]]
```

```
4
5 no=Compile[{{\[Omega]_Real},{T_Real}},Sqrt[(5.653` +7.940999999999999`*^-7 (-24.5`+T) (570.82` ...
      +T)+(89.61` -2.188`*^-6 (-24.5`+T) (570.82` ...
      +T))/(-117.7225`+3.5483217534163507`/\[Omega]^2)+(0.1185` +3.134`*^-8 (-24.5`+T) ...
      (570.82` +T))/(-(0.2091` -4.641`*^-9 (-24.5`+T) (570.82` ...
      +T))^2+3.5483217534163507`/\[Omega]^2)-0.0699019385423021`/\[Omega]^2)]];
6
7 I[L_,T_]:=L(1+1.57*10^-5(T-25)+5.3*10^-9(T-25)^2)
8 \[CapitalLambda]t[\[CapitalLambda]_,T1_]:=\[CapitalLambda](1+1.53*10^-5(T1-19)+5.3*10^-9(T1-19)^2);
```

The ordinary (no) and extraordinary (ne) indices of refraction are from [64].

Temperature-dependent poling period ([CapitalLambda]t[[CapitalLambda]_, T1_]) is rendered more beautifully when pasted in *Mathematica* appearing as Λt[Λ_, T1_]). Both this and the temperature-dependent crystal length I[L_, T_] are taken from [66].

Additional note about copy-paste to *Mathematica*: the (^), (_), ("), and (−) symbols don't render properly. Make sure to Find-and-Replace the problematic symbols; re-add the (_) in the function definition; and remove line numbers.

Listing B.5: Phasematching wavevector mismatch function

```
1 \[ CapitalDelta ]kz2[ksx_, kix_, ksy_, kiy_,\[ Omega]s_,\[Omega]0_,T_,\[CapitalLambda]_]:=Module[{c},
2 c=.2998;
3 ne[2\[Omega]0,T]Sqrt[(2\[Omega]0)^2/c^2-(ksx+kix)^2/no[2\[Omega]0,T]^2-(ksy+kiy)^2/ne[2\[Omega]0,T]^2] ...
      -ne[\[Omega]s,T]Sqrt[\[Omega]s^2/c^2-ksx^2/no[\[Omega]s,T]^2-ksy^2/ne[\[Omega]s,T]^2] ...
      -ne[2\[Omega]0-\[Omega]s,T]*Sqrt[(2\[Omega]0-\[Omega]s)^2/c^2-kix^2/no[2\[Omega]0
4 -\[Omega]s,T]^2-kiy^2/ne[2\[Omega]0-\[Omega]s,T]^2]-2\[Pi]/\[CapitalLambda]t[\[CapitalLambda],T]];
```

Full *Mathematica* implementation of Eq. (2.2). In expanded form:

$$\begin{aligned}\Delta k =& n_e(2\omega_0)\sqrt{\frac{(2\omega_0)^2}{c^2}-\frac{(k_{s,x}+k_{i,x})^2}{n_o^2(2\omega_0)}-\frac{(k_{s,y}+k_{i,y})^2}{n_e^2(2\omega_0)}}\\ &- n_e(\omega_s)\sqrt{\frac{(\omega_s)^2}{c^2}-\frac{k_{s,x}^2}{n_o^2(\omega_s)}-\frac{k_{s,y}^2}{n_e^2(\omega_s)}}\\ &- n_e(2\omega_0-\omega_s)\sqrt{\frac{(2\omega_0-\omega_s)^2}{c^2}-\frac{k_{i,x}^2}{n_o^2(2\omega_0-\omega_s)}-\frac{k_{i,y}^2}{n_e^2(2\omega_0-\omega_s)}}-\frac{2\pi}{\Lambda},\end{aligned} \tag{B.1}$$

Listing B.6: SPDC Spectral integration function

```
1 psi\[Omega]3sqrt[\[Omega]s_?NumericQ,L_,wp_,T_,\[Omega]0_,\[CapitalLambda]_,kr_]:=Module[{c},
2 c=.2998;
```

```
Chop[NIntegrate[Sqrt[\[Omega]s]L^2 Exp[-((kix+ksx)^2+(kiy+ksy)^2) ...
    wp^2]Sinc[\[CapitalDelta]kz2[ksx,kix,ksy, kiy ,\[Omega]s,\[Omega]0,T,\[CapitalLambda]] ...
    L/2]^2,{ksx,-kr,kr},{ksy,-kr,kr},{kix,-kr,kr},{kiy,-kr,kr}, ...
    Method->{"GlobalAdaptive",Method->"GaussKronrodRule","SymbolicProcessing"->0},PrecisionGoal->3]]
```

Listing B.7: SPDC Spatial integration function

```
psi\[Omega]3v2sqrt\[Omega][ksx_,ksy_,\[Omega]s_?NumericQ,L_,wp_,T_,\[Omega]0_,\[CapitalLambda]_,kr_]:=Module[{c},
c=.2998;
Chop[NIntegrate[Sqrt[\[Omega]s]L^2 Exp[-((kix+ksx)^2+(kiy+ksy)^2) ...
    wp^2]Sinc[\[CapitalDelta]kz2[ksx,kix,ksy, kiy ,\[Omega]s,\[Omega]0,T,\[CapitalLambda]] ...
    L/2]^2,{kix,-kr,kr},{kiy,-kr,kr}, ...
    Method->{"GlobalAdaptive",Method->"GaussKronrodRule","SymbolicProcessing"->0},PrecisionGoal->3]]
```

Listing B.8: FWHM bandwidth function

```
bw[\[Sigma]_]:=((2\[Pi] .2998)/(1.064-\[Sigma]/2)-(2\[Pi] .2998)/(1.064+\[Sigma]/2))/2.355
```

Listing B.9: X-blob function

```
psi\[Omega]3sqrtxmod[\[Omega]s_?NumericQ,ksx_?NumericQ,L_,wp_,T_,\[Omega]0_,\[CapitalLambda]_,kr_]:=Module[{c},
c=.2998;
Chop[NIntegrate[Sqrt[\[Omega]s]L^2 Exp[-((kix+ksx)^2+(kiy+ksy)^2) ...
    wp^2]Sinc[\[CapitalDelta]kz2[ksx,kix,ksy, kiy ,\[Omega]s,\[Omega]0,T,\[CapitalLambda]] ...
    L/2]^2,{ksy,-kr,kr},{kix,-kr,kr},{kiy,-kr,kr}, ...
    Method->{"GlobalAdaptive",Method->"GaussKronrodRule","SymbolicProcessing"->0},PrecisionGoal->3]]
```

Code in action

Computationally efficient ways of generating plotable simulation data. Works well on grid computers.

Listing B.10: SPDC spatial emission with bandpass filter

```
ParallelTable [{ksx,
   NIntegrate[(Abs[
       psi\[Omega]3v2sqrt\[Omega][ksx, 0, \[Omega]s, 5000, 38.7,
        108.6 - 1.8, 2 \[Pi] .2998/1.064, 6.76775, .866]]*
      Exp[-((\[Omega]s - 2 \[Pi] .2998/1.064)^2/
        bw[.010/(2 Sqrt[Log[2]])]^2)]), {\[Omega]s,
     2 \[Pi] .2998/1.3, 2 \[Pi] .2998/0.90},
    Method -> {Automatic, "SymbolicProcessing" -> 0},
```

```
9       PrecisionGoal -> 3]}, {ksx, 0, .41, 0.0067},
10    Method -> "FinestGrained"]; // AbsoluteTiming
```

Listing B.11: SPDC spectral emission

```
1  ParallelTable [{2\[Pi] .2998/\[Omega]s,(Abs[psi\[Omega]3sqrt[\[Omega]s,5000,66.3,140.9+0,2\[Pi] ...
       .2998/(1.064) ,6.760,0.1333]]) },{\[Omega]s,2\[Pi] .2998/1.16,2\[Pi] ...
       .2998/.97,0.012}, Method->"FinestGrained"];
```

B.2.2 A method for choosing parameters for simulating SPDC

Λ	poling period
$\mathbf{q}_{\text{lens}}$	Wavevector from NA of coupling lens (or most limiting aperture)
$\mathbf{q}_{\text{w}}$	Wavevector from pump waist divergence angle

Table B.1: Parameters needed for SPDC simulation.

Procedure

1. Measure spectral tuning curves via spectrometer. Pick out experimentally what the degenerate temperature is
2. Calculate $\mathbf{q}_{\text{w}}$ from the divergence angle of the beam waist
3. Solve (NSolve or FindRoot) $\Delta k = 0$ of Listing B.5 with $\mathbf{q}_{\text{w}}$ included as the perpendicular wavevector components
4. Simulate SPDC spectrum (Listing B.11) for a few measured temperatures, compare with measured spectrum
5. Tune Λ a few nanometers as needed to overlap

B.2.3 Spatial donut Gaussian model

The bandpass filtered down-conversion imaged on the CCD camera was fit using NonlinearModelFit in *Mathematica* to a "donut" Gaussian of radius r_0 and with variances σ_x and σ_y in units of pixels, as seen in Eq. (B.2).

$$F_{\text{donut}}(r) = \text{bkg} + \mathcal{N} \exp\left[-\left(\sqrt{\frac{1}{2(1-\rho^2)}\left(\frac{(x-x_0)^2}{2\sigma_x} + \frac{(y-y_0)^2}{2\sigma_y} - \frac{2\rho(x-x_0)(y-y_0)}{2\sigma_x\sigma_y} \right)} - \frac{r_0}{\sqrt{\sigma_x\sigma_y}} \right)^2 \right] \tag{B.2}$$

Rotation rotation of the donut was controlled by ρ, though values were typically near zero. The donut was centered on the beam profiler at pixel numbers (x_0, y_0). Since these beam profiler measurements were taken near the limit of this camera's sensitivity, the noise floor, bkg and peak height $\mathcal{N}$ to accurately fit this noisy, realistic data.

The X-blob representations of Section 2.3.1 required the parameters r_0 and σ_x/σ_y. Due to the square root, the true variances at FWHM, in units of micrometers, is $\sigma_{x,\text{true}} = C_{x\to\mu m} \times \sqrt{2\sqrt{2\ln 2}\sigma_x}$ for this beam profiler camera's pixel conversion $C_{x\to\mu m} = 4.65$ μm/px.

B.2.4 Gaussian beam propagation

In order to compare the experimental measurements to the spatial integrations and vice versa, an accurate conversion between Cartesian space and momentum space was needed. It was found that refraction at the interface between PPLN and air resulted in a constant, noticeable radial offset thus beam propagation through the ABCD matrix method was employed.

Gaussian ABCD matrix definitions

The ABCD matrix method allows an optical beam, represented as an initial height, x_1, and slope (angle), x_1', with respect to the optical axis, to be transformed by matrices making up an optical system into an output vector. This formalism holds for paraxial beams.

$$\begin{pmatrix} x_2 \\ x_2' \end{pmatrix} = \begin{pmatrix} A & B \\ C & D \end{pmatrix} \begin{pmatrix} x_1 \\ x_1' \end{pmatrix} \tag{B.3}$$

For Gaussian beams propagating along the z-axis, properties of the radius of curvature, $R(z)$ of the wavefront can be described by the complex q-parameter [19, 124]

$$\frac{1}{q(z)} = \frac{1}{R(z)} - i\frac{\lambda}{\pi w(z)^2} \tag{B.4}$$

where the q-parameter can additionally be related by

$$q(z) = z + iz_R \tag{B.5}$$

for z_R being the Rayleigh range. Using the optical system results of the ABCD law, the output q-parameter (labelled q_2) can be related to the matrix elements of Eq. (B.3) by

$$q_2 = \frac{Aq_1 + B}{Cq_1 + D}. \tag{B.6}$$

Propagation (distance d)	Lens (focal length f)	Refraction (refractive index $n_1 \to n_2$)
$M_{\text{free}}(d) = \begin{pmatrix} 1 & d \\ 0 & 1 \end{pmatrix}$	$M_{\text{lens}}(f) = \begin{pmatrix} 1 & 0 \\ -\frac{1}{f} & 1 \end{pmatrix}$	$M_{\text{refrac}} = \begin{pmatrix} 1 & 0 \\ 0 & \frac{n_1}{n_2} \end{pmatrix}$

Table B.2: ABCD law matrices for modelling optical systems

Propagation through PPLN

Of interest for modelling PPLN is the propagation from lens to beam waist in PPLN or vice versa.

To determine the waist size within PPLN for a given lens focal length, the q-parameter (Eq. B.6) of the optical system needs to be calculated. For a $f = 175$ mm lens with a waist at the center of a 5 mm PPLN crystal of length L, the matrix representing the optical system is

$$\mathbf{M} = M_{\text{free}}(L/2)M_{\text{refrac}}(n_{\text{air}}, n_{\text{PPLN}})M_{\text{free}}(f - L/2)M_{\text{lens}}(f) \tag{B.7}$$

results in a q-parameter of $q_2 = -2698 + 8854i$, in units of micrometers. Relating the imaginary portion to the Rayleigh range of Eq. (B.5) and solving for the desired beam waist $w_{\text{PPLN}} = 38.7$ μm. This is larger, due to refraction as compared to the refraction-free result of $w_{\text{air}} = 26.3$ μm, as generated from optical system $\mathbf{M} = M_{\text{free}}(f)M_{\text{lens}}(f)$ and by conventional Gaussian optical means [19].

Position to wavevector conversion

Building on the previous beam propagation matrix formalism, a function for conversion between position and perpendicular wavevector, q (not to be confused with the q-parameter of the previous section) can be made from extraction of the half-angle, x_2', from the output vector.

Let the optical system – spanning the beam waist in PPLN to the collimating lens in air – for propagation in the z-direction, be defined as:

$$\mathbf{M}_q(z) = M_{\text{free}}(f|_\lambda - z)M_{\text{refrac}}(n_o, n_{\text{air}})M_{\text{free}}(z) \tag{B.8}$$

where it is worth while to obtain the actual focal length of the lens for the wavelength of interest via Zemax OpticStudio or the like rather than relying on the design wavelength.

The initial vector for the down-conversion cone is defined as

$$\begin{pmatrix} x_1 \\ x_1' \end{pmatrix} = \begin{pmatrix} 0 \\ \arctan\left[\frac{1}{2}\frac{y}{f}\right] \end{pmatrix} \tag{B.9}$$

for the beam profiler position y. The factor of $\frac{1}{2}$ is necessary from the definition of Eq. (B.2).

The beam profiler positions can be converted to wavevector via

$$F_q(y) = \frac{2\pi}{\lambda}\sin(x_2'). \tag{B.10}$$

Similarly, wavevector to position transformation is obtained from calculating the component x_2 from the output vector $\begin{pmatrix} x_2 \\ x_2' \end{pmatrix}$ is calculated from

$$\mathcal{M}_y(q) = M_{\text{free}}(f|_\lambda - L/2)M_{\text{refrac}}(n_o, n_{\text{air}})M_{\text{free}}(L/2) \tag{B.11}$$

with initial vector

$$\begin{pmatrix} x_1 \\ x_1' \end{pmatrix} = \begin{pmatrix} 0 \\ \arcsin\left[\frac{q}{\frac{2\pi n_o}{\lambda}}\right] \end{pmatrix}. \tag{B.12}$$